Charge ordering phenomena and superconductivity in underdoped cuprates

L. Tassini

Lehrstuhl E23 für Technische Physik

Walther-Meissner-Institut für Tieftemperaturforschung
der Bayerischen Akademie der Wissenschaften

Charge ordering phenomena and superconductivity in underdoped cuprates

Leonardo Tassini

Vollständiger Abdruck der von der Fakultät für Physik der Technischen Universität München zur Erlangung des akademischen Grades eines

Doktors der Naturwissenschaften

genehmigten Dissertation.

Vorsitzender:		Univ.-Prof. Dr. M. Ratz
Prüfer der Dissertation:	1.	Univ.-Prof. Dr. R. Gross
	2.	Univ.-Prof. Chr. Pfleiderer, PhD.

Die Dissertation wurde am 30.10.2007 bei der Technischen Universität München eingereicht und durch die Fakultät für Physik am 16.01.2008 angenommen.

Contents

Chapter 1

Introduction

In 1986 Bednorz and Müller discovered superconductivity at approximately 30 K in $Ba_xLa_{5-x}Cu_5O_{5(3-y)}$ [1], starting the era of high temperature superconductivity. This result triggered an intense scientific activity in the field of the oxide-superconductors (commonly referred to as cuprates), and new compounds were synthesized with increasingly higher transition temperature, up to the actual highest superconducting transition temperature of approximately 133.5 K in $HgBa_2Ca_2Cu_3O_{8+x}$ [2].

Oxide superconductors belong to the material class of strongly correlated electron system. Without electronic correlations, for an undoped cuprate such as La_2CuO_4 with the Cu^{2+} ion in a $3d^9$ configuration one would expect a half-filled band and therefore metallic behaviour. However, due to strong electronic correlations oxide superconductors at half filling are Mott-Hubbard insulators, where a large on-site electron-electron repulsion U suppresses charge fluctuations and electrical transport [3, 4, 5, 6, 7, 8, 9]. For this reason they are usually referred to as undoped with the doping level p set at 0. On moving away from half-filling by doping with electron or holes the cuprates are showing a rich variety of physical phenomena including high temperature superconductivity. In this thesis only hole doped materials will be discussed. At high doping levels $p \gtrsim 0.27$ the physics of cuprates is well described by the Fermi liquid picture, and the oxide superconductors behave

approximately like conventional metals [10]. At intermediate doping levels, $0.05 \leq p \leq 0.27$, superconductivity emerges, and above the transition temperature T_c an unconventional normal state is found. At optimal doping, defined as the doping level where T_c is maximal ($p \approx 0.16$ for all cuprate families), the normal state resistivity shows linear temperature dependence down to very low temperature [11, 12] in contrast to the resistivity of conventional metals. Below optimal doping, between T_c and a temperature usually labeled T^* in the literature a so called pseudgap regime is observed, which is characterized by a **k**-dependent depletion of the density of states [13, 14, 15, 16]. Approximately in the same doping range, a static inhomogeneous spin and charge ordering (spin density waves and charge density waves), usually referred to as stripes has been found in specific compounds [17, 18, 19, 20, 21]. Furthermore, in $La_{2-x}Sr_xCuO_4$ non-static spin density waves have been found in a large doping range, resembling very much a dynamical version of the static stripe ordering [22, 23, 24, 25, 26]. All these phenomena make the applicability of the Fermi-liquid theory in the intermediate doping regime questionable [27].

In addition to all the exotic normal-state properties, superconductivity itself in the cuprates remains a puzzle. Various scenarios have been proposed such as (i) interactions of the electronic spin with the surrounding spins leading to pairing, (ii) interaction with charge fluctuations, or (iii) the splitting of the electrons into constituents that behave like free particles carrying only spin or only charge, where to make the transition into the superconductive phase pairing is not necessary. Finally, since it was found that also phonons and Coulomb interaction strongly renormalize the electron properties [28, 29, 30] they could play a role in high temperature superconductivity.

At present, a key question is the role of stripes with respect to superconductivity. Stripes may be at the heart of high temperature superconductivity, may be irrelevant, or may even compete with superconductivity. In this context, a distinction between static and fluctuating stripes has to be done. It is now clear that static stripes compete with superconductivity. This is sup-

ported by the reduction of T_c of $La_{1.6-x}Nd_{0.4}Sr_xCuO_4$ [17, 31], as well as by the complete suppression of superconductivity up to approximately $p = 0.20$ in $La_{1.8-x}Eu_{0.2}Sr_xCuO_4$ [20]. However, it has been shown theoretically that fluctuating stripes could promote superconductivity [32, 33]. Another important question is whether stripes are a general feature common to all oxide superconductors or whether they are a peculiarity of only some specific compounds. Finally, since stripes and the pseudogap phenomena appear approximately in the same doping range the question arises about a possible relationship between the two phenomena.

Electronic Raman scattering is a powerful tool for investigating charge ordering phenomena. The photons couple directly to the charge, and with inelastic (Raman) light scattering the response of charge fluctuation is measured. Therefore, it is particularly useful to detect the response of dynamical ordering phenomena of conduction electrons [34], which are hard to pin down. Due to the selection rules even local deviations from the overall symmetry can be detected. The latter is particularly useful to study the symmetry of the charge ordering. The effect of dynamical charge ordering has been observed with Raman scattering via an additional low-energy peak in $La_{1.90}Sr_{0.10}CuO_4$ [35]. In addition to the capability of detecting dynamical charge order also superconductivity can be studied in detail with Raman scattering. Therefore, it is the appropriate technique to study the interrelation of charge order and superconductivity.

In this work the underdoped regime of two different families of cuprates, $La_{2-x}Sr_xCuO_4$ and $(Y_{1-y}Ca_y)Ba_2Cu_3O_{6+x}$, characterized by very different T_c^{MAX}, was investigated. Evidence of universal dynamical charge order (stripes) with a preferential direction along the diagonal of the CuO_2 planes was found below the onset point of superconductivity p_{sc1}. A qualitative relationship between charge ordering phenomena and superconductivity was found.

Charge and spin ordering sensitively respond to applied pressure. This has been shown by measurements on $La_{1.8-x}Eu_{0.2}Sr_xCuO_4$, where the static or-

dering is destroyed upon applying pressure, and superconductivity is restored [36]. Therefore, in order to study ordering phenomena it is particularly useful to measure the Raman response as function of pressure. In addition, the pressure dependence of the Raman response will provide information on the electron-phonon coupling helping to clarify the role of phonons in the context of high temperature superconductivity. In this thesis a completely new setup for Raman measurements at high pressure was designed and built up. Test measurements with the high pressure setup were successfully performed.

The thesis is organized as follows: a brief introduction to the most important properties of cuprates is presented in chapter 2. The theoretical background of the Raman effect is introduced in chapter 3, and the details of the samples, their characterization, and the experimental setup are described in chapter 4. In chapter 5 the experimental results are presented, followed by an interpretation and discussion in chapter 6. In appendix A the high pressure setup is described in detail, and the results of the test measurements are shown.

Chapter 2

High Temperature Superconductors

2.1 Introduction

Copper oxygen compounds with high superconducting transition temperature have various crystal structures and chemical compositions. The essential structural unit common to all cuprate families are the CuO_2 planes (Fig. 2.1). Since everything else changes from one compound to another, the characteristic physics of cuprates is believed to occur in the CuO_2 planes. Different cuprate families show a number of common physical properties. The most relevant can be summarized as follows:

- Cuprates are quasi two-dimensional doped Mott-Hubbard insulators. The parent compounds are antiferromagnetic insulators that can be driven in a metallic or superconducting phase by adding charge carriers.
- Cuprates show critical temperatures in the range up to 160 K typically one order of magnitude higher than the critical temperatures of conventional superconductors.
- The superconducting coherence length ξ is strongly anisotropic with the in-plane value close to 10 Å. The out-of-plane value of only about 1 Å is

much smaller than the lattice constant.

- The magnetic penetration depth λ is of the order of 1000 Å or higher. Due to the large ratio $\kappa = \lambda/\xi > 100$, cuprates are extreme as type II superconductors.

The conducting CuO_2 planes are parallel to the a and b crystallographic axes. The CuO_2 plane has copper atoms sitting at the corner of a square with oxygen atoms placed between the copper atoms, as shown in Fig. 2.1. The non-conducting layers between the CuO_2 planes act as charge reservoirs. The carrier concentration in the CuO_2 planes can be varied by changing the chemical composition of the non-conducting layers.

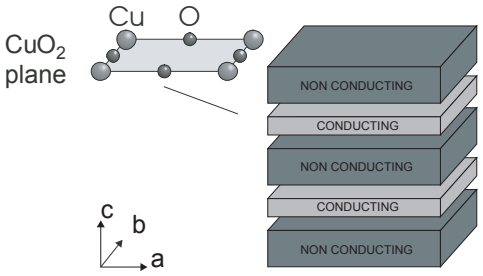

Figure 2.1: *Sketch of the layer structure (of the unit cell) of high temperature superconductors.*

According to local density approximation (LDA) calculations the $3d_{x^2-y^2}$ copper orbitals, strongly hybridized with the oxygen $2p_x$ and $2p_y$ orbitals are the highest occupied states, and therefore determine the low-energy electronic properties. The CuO_2 plaquette and the relevant orbitals are represented in Fig. 2.2. LDA for a square lattice shows three bands (see Fig. 2.3). In absence of electronic correlations at half filling (i.e., one electron per Cu $3d_{x^2-y^2}$ orbital, corresponding to zero doping) the Fermi level would be in the anti-bonding band leading to a metallic state [37]. However, experiments show that at half filling cuprates are antiferromagnetic insulators. The reason is that the LDA picture is oversimplified and does not include correlation effects. In the high temperature superconductors the on-site electron-electron repulsion U for the Cu $3d$ electrons is comparable to the band width and the antibonding band splits into two bands called

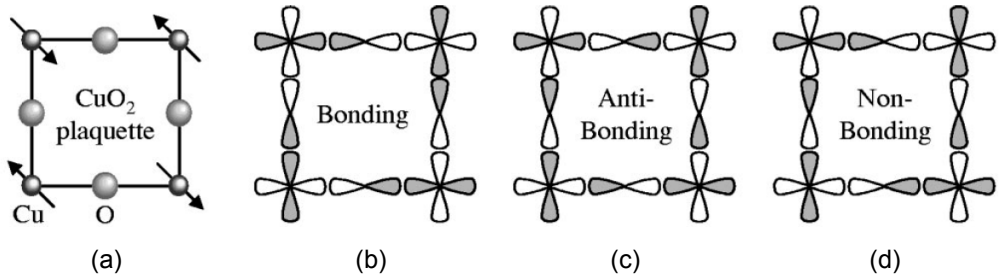

Figure 2.2: *CuO_2 plaquette (a), and Cu $d_{x^2-y^2}$ and O 2p orbitals for bonding, antibonding, and non bonding hybridized wave functions. The figure is taken from Ref. [38]*

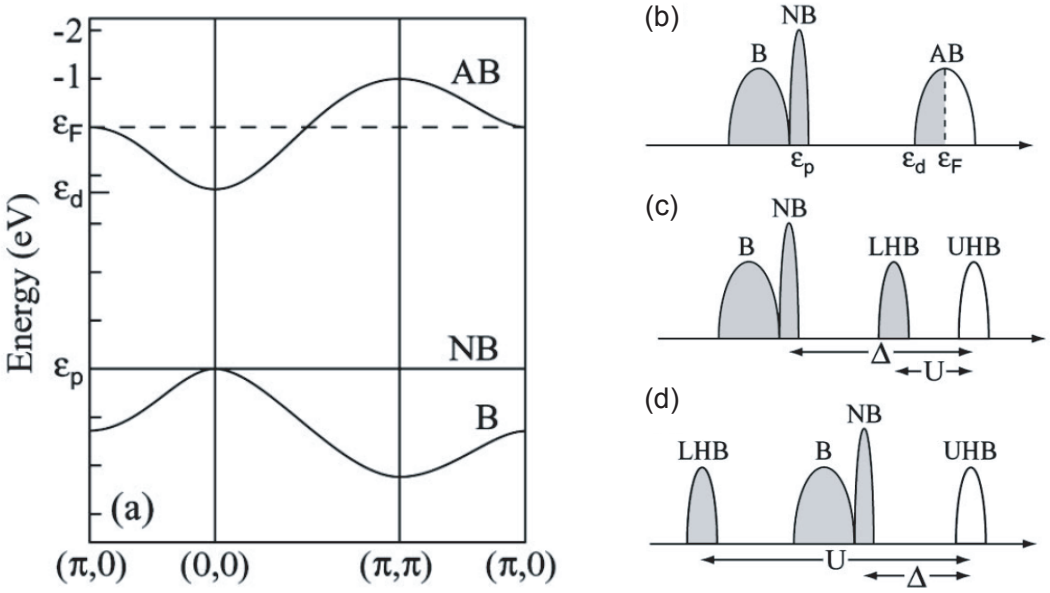

Figure 2.3: *(a) Results of local density approximation (LDA) calculations for the square lattice [37]. (b) In the absence of correlations the system is metallic with the Fermi level in the half filled anti-bonding band. (c, d) Including correlations the system becomes a Mott insulator or a charge-transfer insulator, respectively, for $\Delta > U > W$ and $\Delta < U < W$. U indicates the electron-electron repulsion energy, W the bandwidth, and Δ the charge-transfer energy. The figure is taken from Ref. [38]*

lower (filled) and upper (empty) Hubbard bands (see Fig. 2.3). Since the lower Hubbard band is completely filled the conductivity vanishes.

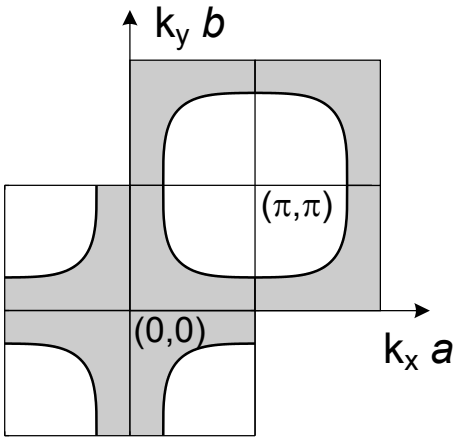

Figure 2.4: *Schematic representation of the typical nearly 2D Fermi surface in cuprates. White and shaded areas denote unoccupied and occupied states, respectively.*

The coupling perpendicular to the CuO_2 planes is very small, and the carriers move practically only in the two-dimensional conducting planes. The Fermi surface is nearly cylindrical as plotted in Fig. 2.4. Fermi surfaces in various cuprates have been measured with angle resolved photoemission spectroscopy (ARPES), and a barrel-like Fermi surface centred at the (π, π) point of the Brillouin zone has been found [38, 39]. A sketch of the Fermi surface in the Brillouin zone is plotted in Fig. 2.4.

2.2 Phase diagram

Independent of the family all cuprates show practically the same temperature-doping phase diagram sketched in Fig. 2.5. The doping can be achieved with donors or acceptors, and the material is denoted as electron-doped or hole-doped, respectively. In this thesis only hole-doped samples have been studied. Hence the discussion here is limited to the hole doped side of the phase diagram. The parent compound at zero doping is an antiferromagnetic insulator with a Néel temperature T_N of the order of room temperature. With increasing carrier concentration the Néel temperature decreases and long-

range antiferromagnetism (AF) vanishes rapidly disappearing approximately at a doping level p of 0.02 holes per CuO_2 formula unit. At higher doping superconductivity evolves. The superconductive phase is terminated by a parabola described by the empirical relation [40]

$$T(p) = T_c^{\mathrm{MAX}} \left[1 - 82.6(0.16 - p)^2\right], \tag{2.1}$$

starting at $p \approx 0.05$ and ending at $p \approx 0.27$. The maximum critical temperature T_c^{MAX} is found at $p \approx 0.16$, referred to as the optimum doping level (OPT). Regions at lower and higher doping are referred to as underdoped (UD) and overdoped (OD), respectively. In the overdoped region the con-

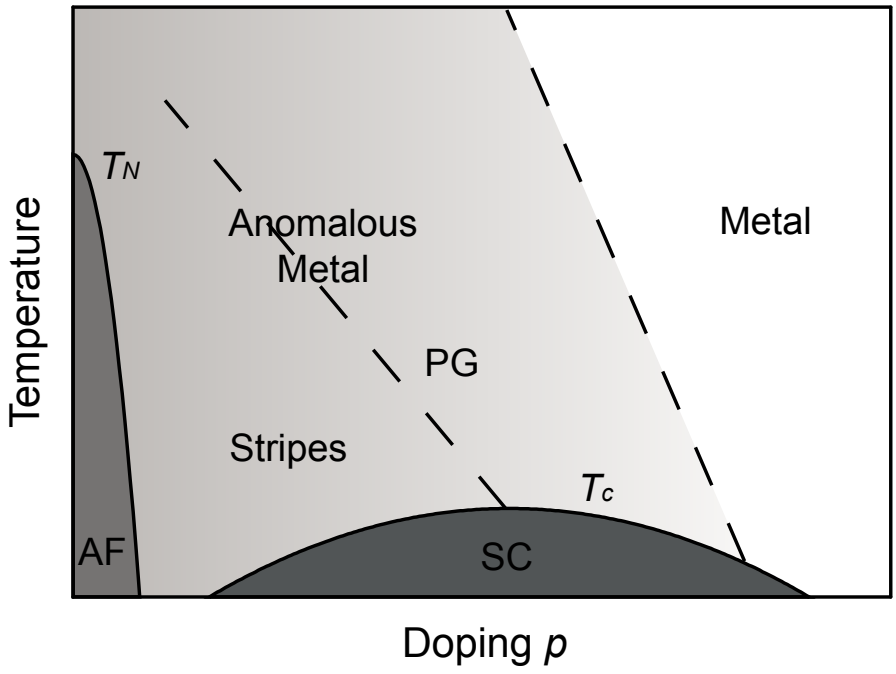

Figure 2.5: *Phase diagram of hole-doped high-temperature superconductors. Solid lines mark phase transitions, and dashed lines indicate crossovers. AF and SC are the antiferromagnetic and superconducting phases, respectively, with related transition temperatures T_N and T_c. PG indicates the region where the pseudogap is believed to open, and stripes indicates the region where superstructures have been been found in some compounds.*

cept of Landau quasiparticles (QP) seems to be a reasonable approximation [10, 41, 42, 43]. In this regime cuprates behave as conventional metals.

The normal state at lower carrier concentration exhibits unusual properties which are poorly understood at present. In this region below optimum doping the opening of a momentum dependent gap, usually referred to as pseudogap (PG) is observed [13]. Approximately in the same doping range, where the pseudogap is observed, charge and spin modulation often referred to as charge and spin stripes, has been detected in La-based compounds (see Ref. [17] and Sect. 2.5).

Crossovers in the electronic properties, indicated by the dashed lines in Fig. 2.5, have been found and suggest the presence of a quantum critical point (QCP) near the optimal doping level [44, 45].

2.3 Superconducting gap

In the weak coupling limit superconductivity is described by the Bardeen-Cooper-Schriffer (BCS) theory [46]. In BCS theory the electron-phonon interaction leads to an effective attractive electron-electron interaction, and the formation of Cooper pairs where the electrons have momenta **k** and -**k** and the pair has no internal angular momentum (s-wave pairing).

BCS theory shows that the superconducting ground state is separated by an energy gap Δ from the excited states. The gap of conventional superconductors has the following characteristics:

- It is constant in **k**-space
- At $T = 0$, the ratio of the gap and the transition temperature T_c is universal,
$$\frac{\Delta(0)}{k_B T_c} = 1.76 \tag{2.2}$$
- Close to T_c, the gap vanishes as
$$\frac{\Delta(T)}{\Delta(0)} = 1.74(1 - \frac{T}{T_c})^{1/2} \tag{2.3}$$

While it is clear that the electrons form singlet pairs also in the cuprates [47], substantial differences with respect to conventional superconductors have been observed. Several techniques provide evidence for an anisotropic superconducting gap with nodes along the diagonals of the Brillouin zone as sketched in Fig 2.6 (b and c) [48, 49, 50]. Many types of experimental techniques such as angle-resolved photoemission spectroscopy (ARPES), infrared, Raman, tunnelling, and NMR spectroscopy, etc., measure only the modulus of the order parameter and therefore cannot discriminate between a $d_{x^2-y^2}$ and $|d_{x^2-y^2}|$. However, the phase sensitive probes such as flux quantization measurements have shown that $\Delta(\phi)$ (with ϕ the azimuthal angle on the Fermi surface) changes sign at the nodes (see [51] for a review on experimental results on $\Delta(\phi)$), and that a gap with $d_{x^2-y^2}$ symmetry, sketched in Fig 2.6 (c), is most compatible with the results in cuprates.

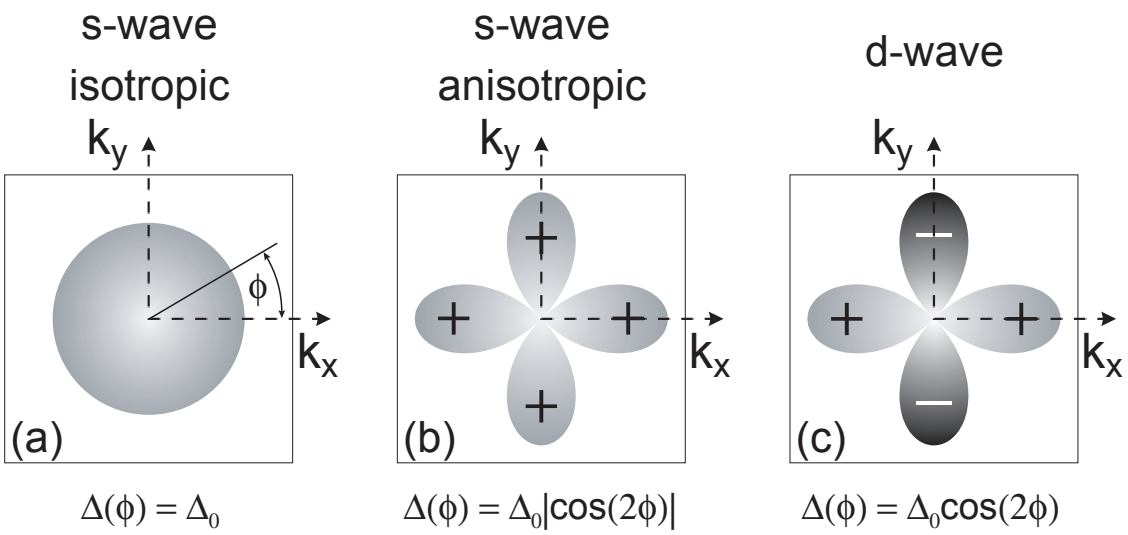

Figure 2.6: *(a) Variation of the gap function in* **k***-space for the isotropic s-wave symmetry. (b) and (c) show anisotropic s-wave and d-wave gaps, respectively.* ϕ *indicates the azimuthal angle on the Fermi surface.*

The superconducting gap can be studied also with Raman scattering (see Chap. 3 for details). Going from the normal into the superconducting state there is a redistribution of spectral weight, where the broad continuum scat-

tering is depressed at low frequencies and spectral weight is transferred to higher frequencies, forming a broad peak. The peak is often referred to as the pair breaking peak. The position of the peak depends on the symmetry.

At optimal doping ($p \approx 0.16$) the pairbreaking peaks are in the proper relative position expected for d-wave pairing, and $2\Delta_{\mathrm{MAX}}/k_B T_c$ is approximately 8 [34, 52, 53, 54]. In the overdoped regime the B_{1g} peak obeys the relation $\Omega_{\mathrm{peak}}^{B_{1g}}/T_c^{\mathrm{MAX}} = 46(0.28-p)$ [34, 55, 56, 57, 58]. The B_{1g} peak vanishes slightly below optimal doping [34], approximately where the loss of coherence is observed with ARPES [59].

At present the origin of the B_{1g} peak in the superconducting state is still controversial. Recently, origins alternative to pair breaking were proposed, such as a collective mode appearing below T_c from either spin-coupling or charge-density-waves [60, 61, 62].

In B_{2g} symmetry the peak position in the superconducting phase tracks T_c [34]. However, there are no results at very low doping levels close to the antiferromagnetic (AF) to superconducting (SC) transition.

2.4 Pseudogap

The pseudogap phenomenon is a **k**-dependent reduction of the density of states [63, 13, 15, 64] that is visible at low temperature in underdoped and optimally doped samples, and vanishes in the overdoped regime. Its momentum dependence closely resembles that of the $d_{x^2-y^2}$ superconducting gap of cuprates [15, 64].

Anomalies in the normal state properties, attributed to the pseudogap, were detected with several different experimental techniques. In tunnelling spectroscopy a gap-like feature close to zero bias is seen to persist in the normal state clearly indicating a gap in the tunnelling conductance [63, 13]. In angle-resolved photoemission spectroscopy a gap-like feature around the anti-nodal regions ($(\pi/2, \pi/2)$, see Fig. 2.4) and vanishing in the nodal regions ($(0, \pi)$ and $(\pi, 0)$, see Fig. 2.4) was observed [14, 15, 38, 64]. With

infrared spectroscopy a gap-like depression in the scattering rate was seen below 750 cm^{-1} in the normal state of $YBa_2Cu_4O_8$, and the gap-like feature becomes more pronounced in the superconducting phase [65]. Similar suppressions of the scattering rates were observed in $Bi_2Sr_2CaCu_2O_{8+\delta}$ [66] and $La_{2-x}Sr_xCuO_4$ [67].

One of the peculiarities of cuprates is the linear temperature dependence of the resistivity around optimal doping down to very low temperatures [11, 12]. Strong deviations from the linear resistivity were observed in underdoped samples, as shown in Fig. 2.7 from Ref. [68], and the non linear behaviour was attributed to pseudogap effects [68, 69, 70].

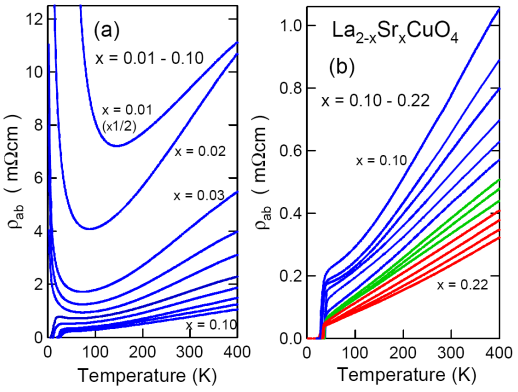

Figure 2.7: *$\rho_{ab}(T)$ data of $La_{2-x}Sr_xCuO_4$ for $x = 0.01 - 0.22$ at 0.01 intervals, from Ref. [68].*

In Raman scattering the pseudogap manifests itself as a depletion of spectral weight. Loss of spectral weight was observed below approximately 800 cm^{-1} in the B_{2g} spectra of underdoped $YBa_2Cu_3O_{6+x}$ [71]. Here spectral weight depression was not measured in B_{1g} symmetry. However, evidence of a pseudogap in B_{1g} symmetry was found in in underdoped $La_{2-x}Sr_xCuO_4$ [72].

In Sect. 5.1.1, 5.1.2, and 5.2 the pseudogap has been investigated in detail as a function of temperature, symmetry, and doping in the range $0 \leq p \leq 0.12$, and the results are discussed in Sect. 6.5.

2.5 Charge and spin order in cuprates

Neutron scattering experiments on $La_{1.48}Nd_{0.4}Sr_{0.12}CuO_4$ show evidence of static charge and spin modulations [17]. This charge and spin modulation, usually called stripes, consists of antiferromagneti-

cally ordered domains periodically separated by charged regions where the holes reside, as sketched in Fig. 2.8. The charge stripes provide an antiphase boundary for the magnetic order. An analogous type of charge and spin order was detected also in other La-based cuprates, specifically in $La_{1.875}Ba_{0.125}CuO_4$ [19], $La_{1.8-x}Eu_{0.2}Sr_xCuO_4$ [20], and $La_{1.875}Ba_{0.125-x}Sr_xCuO_4$ at $x = 0.05$, 0.06 and 0.075 [73]. In $La_{2-x}Sr_xCuO_4$ at $x \lesssim 0.05$ a static spin modulation analogous to the spin order mentioned above was found [22, 24], and at $x \gtrsim 0.05$ magnetic excitations indicating a dynamical version of the spin correlations at lower doping levels was observed [74, 75]. At present it is an open issue whether stripes are confined only to a few compounds or whether stripes, eventually dynamic, are a general feature of oxide-superconductors and provide a good descripton of underdoped cuprates.

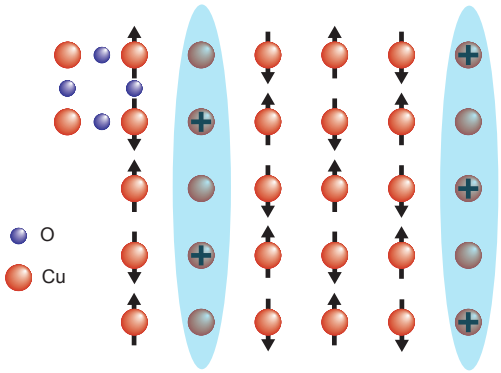

Figure 2.8: *Schematic representation of the charge and spin stripes.*

Another important open question is the relationship between stripes and superconductivity. While it is now established that static order competes with superconductivity, as shown by the depression of the superconducting transition temperature T_c at 1/8 filling in $La_{1.48}Nd_{0.4}Sr_{0.12}CuO_4$ and $La_{1.875}Ba_{0.125}CuO_4$, or by the complete suppression of superconductivity in $La_{1.8-x}Eu_{0.2}Sr_xCuO_4$ up to $p \approx 0.20$, the role of "melted" stripes is less clear and whether or not they could provide a mechanism for high-temperature superconductivity is one of the main topics of current research [76, 77, 78].

In this thesis charge and spin ordering was investigated in detail in underdoped $La_{2-x}Sr_xCuO_4$ and $(Y_{1-y}Ca_y)Ba_2Cu_3O_{6+x}$. The results of the measurements are discussed in Chap. 6.

2.6 Quantum critical points

The normal state of cuprates around optimal doping shows very peculiar properties, such as the linear temperature dependence of the resistivity down to very low temperatures at optimal doping [11, 12]. Here, the Landau Fermi-liquid theory and associated quasiparticle concepts do not seem to be applicable. One possible explanation of the non Fermi liquid character of the normal phase is the low dimensionality of such highly anisotropic systems and their correlated nature. For instance the Fermi liquid theory breaks down in quasi-one dimensional conductors, and the one dimensional metallic phase is described by the Luttinger liquid theory [79, 80]. However, it has been shown that the Fermi liquid picture is preserved for dimension higher than 1 for any Hamiltonian with nonsingular low-energy interactions, and in this hypothesis the Luttinger behaviour is strictly confined to one-dimensional metals [81, 82, 83, 84]. Only sufficiently singular long-range forces lead to non Fermi liquid behaviour at low energy above one dimension [85, 86] and the anomalous properties would then arise as a consequence of singular scattering processes at low energy.

Singular scattering can be related to the existence of a quantum critical point (QCP), where critical fluctuations can mediate singular interactions between the quasiparticles, providing at the same time a strong pairing mechanism. Several experimental results suggest the presence of a QCP around optimal doping, such as transport measurements in $La_{2-x}Sr_xCuO_4$, where evidence of a metal-insulator transition ending at optimal doping at $T = 0$ have been found after the suppression of superconductivity with high magnetic fields [87]. Similar indications come from the low energy excitations distinct from the usual single-particle excitations, observed by infrared spectroscopy and showing evidence of scaling properties [45, 88]. Moreover, qualitative changes of behaviour at optimal doping have been observed in nuclear magnetic resonance [89], susceptibility [90], neutron scattering [91], photoemission [14, 64, 92], specific heat [93], thermoelectric power [94], Hall coefficient [95], and resistivity measurements [87, 90, 96].

Several authors proposed that the properties both in the normal and in the superconducting state are controlled by a QCP [78, 97, 98, 99, 100, 101, 102]. In this context the debate focuses on the nature of the quantum criticality. Antiferromagnetic fluctuations [103, 104], excitonic states [98], or incommensurate charge density waves [78] have been proposed.

In Sect. 6.3 the implications arising from a QCP in the oxide-superconductors are discussed and compared to the data measured in this thesis.

Chapter 3

Raman scattering

In this chapter essentials of electronic Raman scattering are summarized. In particular selection rules of the Raman response will be discussed as well as a connection between the Raman response and other transport properties. A general treatment of electronic Raman scattering can be found for instance in Ref. [34] and references therein.

Electronic Raman scattering is among the few two-particle probes capable of selecting different regions in **k**-space. Due to this peculiarity Raman scattering has successfully been applied to study anisotropies of electron dynamic in the cuprates, to analyze the scattering rate of electrons in certain regions of the Brillouin zone above T_c, and to study the symmetry and the magnitude of the superconducting gap.

3.1 The Raman effect

Raman scattering describes inelastic scattering of light, in which a photon with frequency ω_i and momentum $\mathbf{k}_i$ is absorbed and a photon with frequency ω_s and momentum $\mathbf{k}_s$ is emitted, while the system makes a transition from an initial state $|I\rangle$ to a final state $|F\rangle$. In Fig. 3.1 a sketch of the Raman scattering process is shown. The incident photon drives the system to a high-energy (virtual) level $|\nu\rangle$ that decays into a real level of the system $|F\rangle$ with

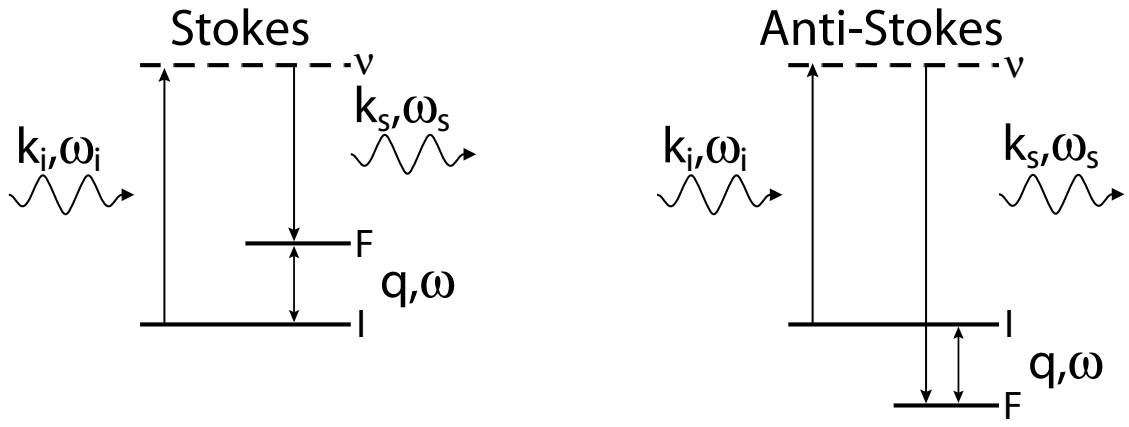

Figure 3.1: *Schematic representation of the Raman effect. The process is called Stokes and anti-Stokes for $\omega_s < \omega_i$ and $\omega_s > \omega_i$, respectively.*

the emission of a scattered photon. If the intermediate state decays into a level with an energy higher than that of the initial state, the energy of the scattered photon is smaller than the energy of the incoming one. This process is called Stokes, vice versa it is called anti-Stokes. The conservation of energy and momentum in the process is expressed by the equations

$$\begin{aligned} \hbar\Omega &= \hbar\omega_i - \hbar\omega_s; \\ \mathbf{q} &= \mathbf{k}_i - \mathbf{k}_s. \end{aligned} \tag{3.1}$$

3.2 Electronic Raman scattering

A system of N electrons in an electromagnetic field is described by the Hamiltonian

$$H = \sum_i^N \frac{[\hat{\mathbf{p}}_i + (e/c)\hat{\mathbf{A}}(\mathbf{r}_i)]^2}{2m} + H_{\text{Coulomb}} + H_{\text{fields}}, \tag{3.2}$$

where $\hat{\mathbf{p}} = -i\hbar\nabla$ is the momentum operator, e is the (positive) elementary charge, H_{Coulomb} is the Coulomb interaction, H_{fields} is the free electromagnetic part (e.g. the external applied field), and $\hat{\mathbf{A}}$ is the vector potential of the field at $\mathbf{r_i}$. It is possible to expand the kinetic energy and rewrite the Hamiltonian

in the form

$$H = H' + \frac{e}{2mc}\sum_i \left[\hat{\mathbf{p}}_i \cdot \hat{\mathbf{A}}(\mathbf{r}_i) + \hat{\mathbf{A}}(\mathbf{r}_i) \cdot \hat{\mathbf{p}}_i\right] + \frac{e^2}{2mc^2}\sum_i \hat{\mathbf{A}}(\mathbf{r}_i) \cdot \hat{\mathbf{A}}(\mathbf{r}_i), \quad (3.3)$$

with $H' = H_0 + H_{\text{field}}$ and H_{Coulomb} included in H_0. The second and third terms of Eq. (3.3) represent the interaction Hamiltonian. The electromagnetic vector potential can be expanded into Fourier modes $\hat{\mathbf{A}}(\mathbf{r}_i) = \sum_{\mathbf{q}} e^{i\mathbf{q}\cdot\mathbf{r}_i}\hat{\mathbf{A}}_{\mathbf{q}}$. In second quantized notation, the electromagnetic field operator takes the form [105]

$$\hat{\mathbf{A}}_{\mathbf{q}} = \sqrt{\frac{hc^2}{\omega_{\mathbf{q}} V}}[\mathbf{e}_{\mathbf{q}} a_{-\mathbf{q}} + \mathbf{e}^*_{\mathbf{q}} a^\dagger_{\mathbf{q}}], \quad (3.4)$$

with V the volume and $a^\dagger_{\mathbf{q}}, a_{\mathbf{q}}$ the creation, annihilation operators of photons with energy $\hbar\omega_{\mathbf{q}} = \hbar c|\mathbf{q}|$ having a polarization denoted by the complex unit vector $\mathbf{e}_{\mathbf{q}}$.

An important quantity connecting light-scattering experiments and theory is the differential cross section defined as the rate of photons scattered from the incident beam into a solid-angle $d\Omega$ with a scattered frequency between ω_s and $\omega_s + d\omega_s$ divided by the flux of incident photons. It is possible to express the differential cross section via the transition rate R of scattering an incident $(\mathbf{q}_i, \omega_i, \mathbf{e}^{(i)}_{\mathbf{q}})$ photon into an outgoing state $(\mathbf{q}_s, \omega_s, \mathbf{e}^{(s)}_{\mathbf{q}})$,

$$\frac{\partial^2\sigma}{\partial\Omega\partial\omega_s} = \hbar r_0^2 \frac{\omega_s}{\omega_i} R, \quad (3.5)$$

where $r_0 = e^2/mc^2$ is the Thompson radius. The transition rate R is determined via Fermi's Golden Rule.

$$R = \frac{1}{\mathcal{Z}}\sum_{I,F} e^{-\beta E_I} \mid \langle F|M|I\rangle \mid^2 \delta(E_F - E_I - \hbar\Omega), \quad (3.6)$$

where $\mathcal{Z}$ is the partition function, $\beta = 1/k_B T$, M is the effective light-scattering operator, and $|I\rangle$ and $|F\rangle$ are the initial and final states of the system, respectively. The sum represents a thermodynamic average over pos-

sible initial and final states with **k**-vectors in the solid angle element $d\Omega$ of the many-electron system having energies E_I, E_F, respectively. All light-scattering processes fall into the category of second-order radiative transitions, in contrast to the rate of the first-order processes, represented by the absorption or emission of one photon. The transition rate has contributions from either the middle or the third terms in Eq. (3.3): the middle terms couples the electron's current to a single photon and the third term couples the electron's charge to two photons. For inelastic light scattering it is necessary to consider terms containing two vector potential operators in the effective light-scattering operator and the terms containing more than two vector potential operators will be neglected.

In the weak correlation limit, the Raman cross section can be expressed in terms of a correlation function $\tilde{S}$ of an effective charge density $\tilde{\rho}$ [34]

$$\frac{\partial^2\sigma}{\partial\Omega\partial\omega_{\rm s}} = \hbar r_0^2 \frac{\omega_s}{\omega_i}\tilde{S}(\mathbf{q}, i\Omega \to \Omega + i0). \tag{3.7}$$

The Raman effective density-density correlation function [34] reads

$$\tilde{S}(\mathbf{q}, i\Omega) = \sum_I \frac{e^{-\beta E_{\rm I}}}{\mathcal{Z}} \int d\tau e^{i\Omega\tau} \langle I \mid T_\tau \tilde{\rho}(\mathbf{q}, \tau)\tilde{\rho}(-\mathbf{q}, 0) \mid I\rangle, \tag{3.8}$$

where T_τ is the complex time τ ordering operator, and the effective charge density is definied by the expression

$$\tilde{\rho}(\mathbf{q}) = \sum_{\mathbf{k},\sigma} \gamma(\mathbf{k}, \mathbf{q}) c^\dagger_{\mathbf{k}+\mathbf{q},\sigma} c_{\mathbf{k},\sigma}. \tag{3.9}$$

Here σ is the spin index, $c^\dagger_{\mathbf{k},\sigma}$ and $c_{\mathbf{k},\sigma}$ are creation and annihilation operators of an electron with momentum **k** and spin σ, respectively, and $\gamma(\mathbf{k}, \mathbf{q})$ is the **k**-dependent Raman vertex. Via the fluctuation-dissipation theorem $\tilde{S}(\mathbf{q})$ can be written in terms of a dynamical effective density susceptibility $\tilde{\chi}$,

$$\tilde{S}(\mathbf{q}, \Omega) = -\frac{1}{\pi}\{1 + n(\Omega, T)\}\tilde{\chi}''(\mathbf{q}, \Omega), \tag{3.10}$$

with $n(\Omega, T)$ the Bose-Einstein distribution and

$$\tilde{\chi}(\mathbf{q}, \Omega) = \langle [\tilde{\rho}(\mathbf{q}), \tilde{\rho}(-\mathbf{q})] \rangle_{\Omega}. \tag{3.11}$$

The Raman vertex has the form [106, 34]

$$\gamma(\mathbf{k}, \mathbf{q}) = \sum_{a,b} \gamma_{a,b}(\mathbf{k}, \mathbf{q}) e_i^a e_s^b, \tag{3.12}$$

with

$$\begin{aligned} \gamma_{a,b}(\mathbf{k}, \mathbf{q}) = \delta_{a,b} \quad &+ \quad \frac{1}{m} \sum_{\mathbf{k}_\nu} \Bigg[\frac{\langle \mathbf{k}+\mathbf{q} \mid p_s^b \mid \mathbf{k}_\nu \rangle \langle \mathbf{k}_\nu \mid p_i^a \mid \mathbf{k} \rangle}{E_{\mathbf{k}} - E_{\mathbf{k}_\nu} + \hbar\omega_i} \\ &+ \quad \frac{\langle \mathbf{k}+\mathbf{q} \mid p_i^a \mid \mathbf{k}_\nu \rangle \langle \mathbf{k}_\nu \mid p_s^b \mid \mathbf{k} \rangle}{E_{\mathbf{k}+\mathbf{q}} - E_{\mathbf{k}_\nu} - \hbar\omega_{\mathrm{s}}} \Bigg], \end{aligned} \tag{3.13}$$

where $e_{i,s}^a$, $e_{i,s}^b$ are the components of the polarization vectors of the incident and scattered light with $a, b = x, y, z$, and $p_{i,s}^a = p^a e^{\pm i \mathbf{q}_{i,s} \cdot \mathbf{r}}$. $|\mathbf{k}+\mathbf{q}\rangle$, $|\mathbf{k}\rangle$, and $|\mathbf{k}_\nu\rangle$ are the final, initial, and intermediate states, respectively, and $E_{\mathbf{k}+\mathbf{q}}$, $E_{\mathbf{k}}$, $E_{\mathbf{k}_\nu}$ are the energies of the final, initial, and intermediate states, respectively. The Raman vertex γ has a weak dependence on $\mathbf{q}$ for $|\mathbf{q}| \ll k_F$. The sum over intermediate states of Eq. (3.13) includes contributions from the states created in the conduction band as well as from states separated from the conduction band. The matrix elements including an intermediate state in the conduction band are proportional to the momentum transferred by the photon, which in the limit q $\ll k_f$ are smaller by a factor of $(v_F/c)^2$ (v_F is the Fermi velocity and c is the velocity of light) than the other terms and can be neglected [107]. Assuming $\omega_{i,s} << | E_{\mathbf{k}_\nu} - E_{\mathbf{k}} |$ for the remaining terms in the sum over $\mathbf{k}_\nu$, $\gamma_{\alpha,\beta}$ assume the form of the mass tensor in the effective mass approximation [34],

$$\gamma_{\alpha,\beta}(\mathbf{k}, |\mathbf{q}| \to 0) = \frac{1}{\hbar^2} \frac{\partial^2 E_{\mathbf{k}}}{\partial k_\alpha k_\beta}. \tag{3.14}$$

3.3 Raman response function

In terms of Green's functions Eq. (3.11) can be expressed in lowest order approximation [34], as

$$\chi_{\gamma\gamma}(\mathbf{q}, i\Omega) = -\frac{2}{V\beta}\sum_{i\omega}\sum_{\mathbf{k}}\gamma_{\mathbf{k}}G(\mathbf{k}, i\omega)\gamma_{\mathbf{k}}G(\mathbf{k}-\mathbf{q}, i\omega - i\Omega), \tag{3.15}$$

where $\gamma_{\mathbf{k}}$ represents the $\mathbf{k}$-dependent Raman vertex and the convention $\hbar = 1$ and $k_B = 1$ is used. $G(\mathbf{k}, i\omega)$ is the fermionic propagator, $\beta = 1/T$, and $i\omega$ are fermionic Matsubara frequencies.

In the presence of interactions the bare propagator is replaced by the renormalized Green's function expressed via the Dyson equation [105]

$$G(\mathbf{k}, i\omega)^{-1} = G^{(0)}(\mathbf{k}, i\omega)^{-1} - \Sigma(\mathbf{k}, i\omega), \tag{3.16}$$

represented in Fig. 3.2 where $G^{(0)}$ is the bare propagator and $\Sigma = \Sigma'(\mathbf{k}, \omega) + i\Sigma''(\mathbf{k}, \omega)$ is the self energy. The imaginary part of the self energy Σ'' has the

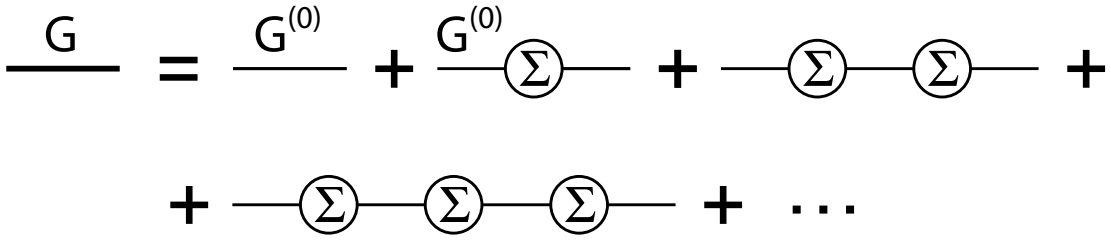

Figure 3.2: *Schematic representation of the Dyson equation. The thick line on the left hand side represents the renormalized propagator while the thin lines on the right hand side indicate the bare propagators, and the bubbles represent the self energy.*

effect of introducing a finite lifetime to the quasiparticles while the real part Σ' represents an energy shift of the excitation [105].

In the presence of interactions and correlations Eq. (3.15) is not normally sufficient, and vertex corrections may become essential. The general expression for the two-particle correlation function describing the nonresonant Ra-

man response of a correlated system reads

$$\chi_{\gamma,\gamma}(\mathbf{q}=0,i\Omega) = -\frac{2}{V\beta}\sum_{i\omega}\sum_{\mathbf{k}}\gamma(\mathbf{k})G(\mathbf{k},i\omega)G(\mathbf{k},i\omega+i\Omega)\Gamma(\mathbf{k};i\omega;i\Omega). \tag{3.17}$$

In the ladder approximation the renormalized Raman vertex is given by the Bethe-Salpeter equation:

$$\Gamma(\mathbf{k};i\omega;i\Omega) = \gamma(\mathbf{k})+\frac{1}{V\beta}\sum_{i\omega'}\sum_{\mathbf{k}'}V(\mathbf{k}-\mathbf{k}',i\omega-i\omega')G(\mathbf{k}',i\omega')G(\mathbf{k}',i\omega'+i\Omega)\Gamma(\mathbf{k}';i\omega';i\Omega), \tag{3.18}$$

where $V(\mathbf{k}-\mathbf{k}',i\omega-i\omega')$ is the generalized electron-electron interaction.

The general expression of the Raman response has to be written in the gauge-invariant form, in which the particle number has to be conserved and charge density fluctuations are screened. The total Raman susceptibility (usually called screened Raman response) assumes the form [108]

$$\chi = \chi_{\gamma\gamma} - \frac{\chi_{\gamma 1}\chi_{1\gamma}}{\chi_{11}} + \frac{\chi_{\gamma 1}\chi_{1\gamma}}{\chi_{11}^2}\chi_{\mathrm{SC}} \tag{3.19}$$

where $\chi_{\mathrm{SC}} = \chi_{11}(1-v_q\chi_{11})^{-1}$ and v_q is the bare Coulomb interaction. The subscript γ denotes the effective Raman density while 1 denotes the pure charge density, obtained when γ is replaced by 1.

3.4 Symmetry properties of the Raman response

The Raman vertex depends on the energies of the incoming and outgoing photons (ω_i,ω_s), on momentum, and on polarization. With a given selection of the polarization states of the incoming and outgoing photons, different components (symmetries) of the Raman vertex can be selected (Eqs. (3.12), (3.13), (3.14)). Different components of the Raman vertex have different $\mathbf{k}$-dependences and act as weighting factors in $\mathbf{k}$-space.

In general, the polarization dependence of the Raman scattering rate

can be classified using group theoretical arguments. The symmetries of the charge-density fluctuations are determined by the light polarizations and the scattering geometry. The Raman vertex can be decomposed into basis functions Φ_μ of the irreducible point group of the crystal [109, 110, 111]

$$\gamma_{\mathbf{k}} = \sum_{\mu} \gamma_\mu \Phi_\mu(\mathbf{k}) \tag{3.20}$$

labeled μ. The various basis functions weight out different regions of $\mathbf{k}$-space. Which set of elements contribute to the sum in (3.20) is determined by the polarizations of the incident and scattered light. For the cuprates the tetragonal D_{4h} group is relevant and the decomposition can be written as

$$\begin{aligned}
\gamma(\mathbf{k}) &= \frac{1}{2} O_{A_{1g}^{(1)}} (e_i^x e_s^x + e_i^y e_s^y) \\
&+ \frac{1}{2} O_{A_{1g}^{(2)}} (e_i^z e_s^z) \\
&+ \frac{1}{2} O_{B_{1g}} (e_i^x e_s^x - e_i^y e_s^y) \\
&+ \frac{1}{2} O_{B_{2g}} (e_i^x e_s^y + e_i^y e_s^x) \\
&+ \frac{1}{2} O_{A_{2g}} (e_i^x e_s^y - e_i^y e_s^x) \\
&+ \frac{1}{2} O_{E_g^{(1)}} (e_i^x e_s^z + e_i^z e_s^x) \\
&+ \frac{1}{2} O_{E_g^{(2)}} (e_i^y e_s^z + e_i^z e_s^y),
\end{aligned} \tag{3.21}$$

with O_μ the corresponding projected operators and $e_{i,s}^a$ $(a = x, y, z)$ the light polarizations.

The momentum dependence of the basis functions relevant for the data measured in this thesis are shown in Fig. 3.3. The dashed white lines indicate the points where the amplitude of the bases functions vanishes. The B_{1g} spectra probes light scattering events along the principal axes, B_{2g} probes the diagonals while A_{1g} is a weighted average over the entire Brillouin zone.

The relation between polarizations and symmetries is shown in Fig. 3.4 where x and y indicate polarizations parallel to the copper-oxygen bonds of

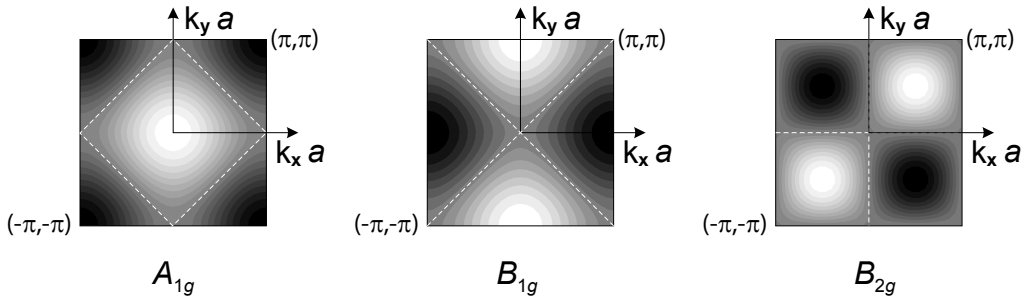

Figure 3.3: *Momentum dependences of the lowest order basis functions into which the Raman vertex is expanded. White and black indicate the maximum positive and negative values, respectively.*

the CuO_2 planes, and x' and y' along the diagonals of the planes. With polarizations in the ab plane single symmetries cannot be accessed individually, and in general a linear combination of two components is measured. In order to extract single components a set of different polarization configurations has to be measured, and a subtraction procedure is required. In Table 3.1 the common experimentally used polarization geometries and the **k**-dependences of the related basis functions $\Phi_\mu(\mathbf{k})$ are shown.

3.5 Collective modes

In Sect. 3.2 and 3.3 Raman scattering from essentially non-interacting conducting electrons was described. However, there are other sources for Raman scattering and the signal can come for example from interactions with collective modes. In superconductors there are several examples of collective excitations, such as the plasma mode (visible also in normal metals), or the excitation arising from the residual interaction between two electrons of a broken Cooper pair, leading to bound states below the pair breaking threshold [110].

Whenever correlation effects come into play competing ground states are quite common, and it is not confined to cuprates only. In the spin- and charge-density-wave superconductors for instance, density wave formation can

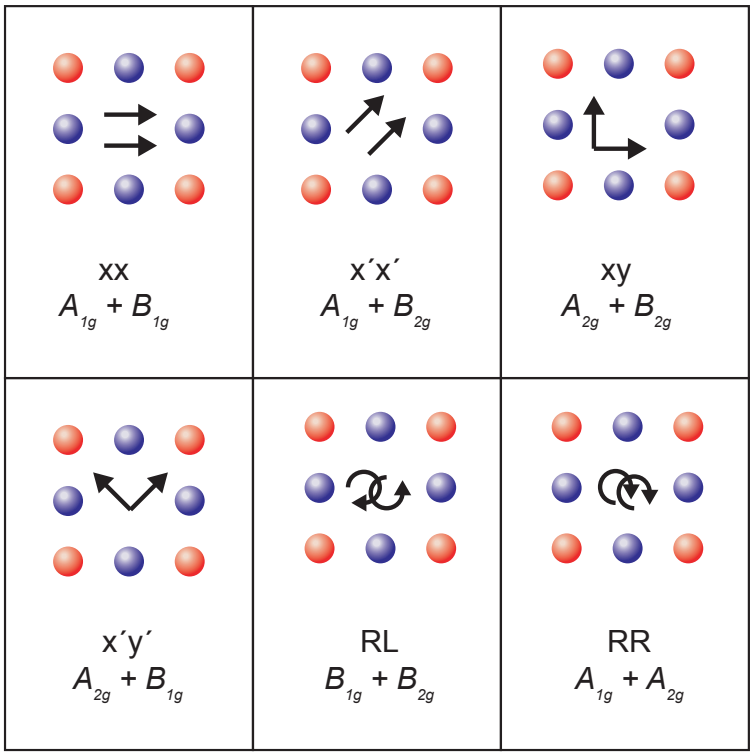

Figure 3.4: *Connection between the symmetries of the Raman vertex* $\gamma(\mathbf{k})$ *and the polarizations of the incoming and outgoing photons in the ab plane for* D_{4h}. *x, y and* x', y' *indicate linearly polarized light along the* $Cu-O$ *bond direction and along the diagonal of the* CuO_2 *planes, respectively; L and R indicate left and right circularly polarized light, respectively.*

lead to a partial suppression of superconductivity. Then, additional modes appear as a result of the competition between the charge-density-wave and superconductivity. Gap modes below 2Δ have been obtained considering the coupling between charge-density and superconducting gap amplitudes [112, 113, 114].

If long-range order is suppressed by thermal or quantum fluctuations, charge-density-wave instability need not necessarily compete with supercn-ductivity but rather can provide an effective coupling mechanism, and col-lective modes can appear as fluctuation-induced modes. Raman scattering from these modes is usually determined from Aslamazov-Larkin fluctuation diagrams [115, 116]. A possible Raman active excitation can be due to the

Geometry	$\hat{e}_i$	$\hat{e}_s$	γ	Basis Functions $\Phi_\mu(\mathbf{k})$
xx, yy	$\hat{x}, \hat{y}$	$\hat{x}, \hat{y}$	$\gamma_{A_{1g}} + \gamma_{B_{1g}}$	$\frac{1}{2}[\cos(k_x a) + \cos(k_y a)] \pm$ $\frac{1}{2}[\cos(k_x a) - \cos(k_y a)]$
$x'x'$	$\frac{1}{\sqrt{2}}(\hat{x} + \hat{y})$	$\frac{1}{\sqrt{2}}(\hat{x} + \hat{y})$	$\gamma_{A_{1g}} + \gamma_{B_{2g}}$	$\frac{1}{2}[\cos(k_x a) + \cos(k_y a)] +$ $\sin(k_x a)\sin(k_y a)$
$x'y'$	$\frac{1}{\sqrt{2}}(\hat{x} + \hat{y})$	$\frac{1}{\sqrt{2}}(\hat{x} - \hat{y})$	$\gamma_{B_{1g}} + \gamma_{A_{2g}}$	$\frac{1}{2}[\cos(k_x a) - \cos(k_y a)][1 +$ $\sin(k_x a)\sin(k_y a)]$
xy	$\hat{x}$	$\hat{y}$	$\gamma_{B_{2g}} + \gamma_{A_{2g}}$	$\sin(k_x a)\sin(k_y a) \times$ $\{1 + \frac{1}{2}[\cos(k_x a) - \cos(k_y a)]\}$
LR	$\frac{1}{\sqrt{2}}(\hat{x} + i\hat{y})$	$\frac{1}{\sqrt{2}}(\hat{x} + i\hat{y})$	$\gamma_{B_{1g}} + \gamma_{B_{2g}}$	$\frac{1}{2}[\cos(k_x a) + \cos(k_y a)] +$ $\sin(k_x a)\sin(k_y a)$
LL	$\frac{1}{\sqrt{2}}(\hat{x} + i\hat{y})$	$\frac{1}{\sqrt{2}}(\hat{x} - i\hat{y})$	$\gamma_{A_{1g}} + \gamma_{A_{2g}}$	$\frac{1}{2}\{\cos(k_x a) + \cos(k_y a) +$ $[\cos(k_x a) - \cos(k_y a)] \times$ $\sin(k_x a)\sin(k_y a)\}$
xz	$\hat{x}$	$\hat{z}$	$\gamma_{E_{1g}}$	$\sin(k_x a)\sin(k_z c)$
yz	$\hat{y}$	$\hat{z}$ $\gamma_{E_{1g}}$	$\sin(k_y a)\sin(k_z c)$	
zz	$\hat{z}$	$\hat{z}$	$\gamma_{A_{1g}^{(2)}}$	$\cos(k_z c)$

Table 3.1: *Components of the transition rate R for various polarization configurations along with the symmetry projections for the D_{4h} point group. x, y and x', y' indicate linearly polarized light along the $Cu-O$ bonds and along the diagonal of the CuO_2 planes, respectively, and L and R indicate left and right circularly polarized light, respectively.*

exchange of two fluctuation modes at wave vectors $\mathbf{Q}_c$ and - $\mathbf{Q}_c$, resulting in a mode at an energy of twice the mass of the fluctuation propagator. Raman scattering allows the selection of different symmetries and with a proper selection of the polarizations different fluctuation modes corresponding to different ordering wave vectors can be selected. The Raman response of spin and charge fluctuations in the normal state of cuprates have been investigated in Ref. [117] and [116], respectively.

In chapter 6 Raman spectra measured in this thesis are compared with Raman response calculated for charge fluctuations.

3.6 Relation between electronic Raman scattering and other transport probes

In this section the relationship between Raman scattering and other transport techniques, such as optical conductivity and conventional resistivity are discussed.

In the normal state the bare propagator is $G^{(0)}(\mathbf{k}, i\omega)^{-1} = i\omega - \xi_{\mathbf{k}}$ and the renormalized one by applying the Dyson equation 3.16 reads

$$G(\mathbf{k}, i\omega) = \frac{1}{i\omega - \xi_{\mathbf{k}} - \sum(\mathbf{k}, i\omega)}, \tag{3.22}$$

where $\xi_{\mathbf{k}} = \epsilon_{\mathbf{k}} - \mu$ is the band dispersion and μ the chemical potential.

In order to analytically evaluate Eq. (3.15) it is convenient to introduce the spectral representation for the Green's function $G(\mathbf{k}, i\omega)$ [105]

$$G(\mathbf{k}, i\omega) = -\int_{-\infty}^{\infty} \frac{dy}{\pi} \frac{G''(\mathbf{k}, y)}{i\omega - y} \tag{3.23}$$

where $G''(\mathbf{k}, i\omega)$ is the imaginary part of the electronic propagator $G(\mathbf{k}, y) = G'(\mathbf{k}, y) + iG''(\mathbf{k}, y)$.

In the weak correlation limit the Raman response is given by Eq. (3.15). After performing the sum over the fermionic Matsubara frequencies $i\omega$ [105], analytic continuation $i\omega \to \omega + i0^+$, and taking the limit $|\mathbf{q}| = 0$, the Raman response reads

$$\chi''_{\gamma\gamma}(\Omega) = \frac{2}{V} \sum_{\mathbf{k}} \gamma_{\mathbf{k}}^2 \int_{-\infty}^{\infty} \frac{d\omega}{\pi} G''(\mathbf{k}, \omega) G''(\mathbf{k}, \omega + \Omega)[f(\omega) - f(\omega + \Omega)], \tag{3.24}$$

where $f(\omega)$ is the Fermi-Dirac distribution.

Eq. (3.24) is the generalized Kubo susceptibility written for the Raman process. In the general case the generalized Kubo susceptibility reads

$$\chi''_{ab}(\Omega) = \frac{2}{V} \sum_{\mathbf{k}} a_{\mathbf{k}} b_{\mathbf{k}} \int_{-\infty}^{\infty} \frac{d\omega}{\pi} G''(\mathbf{k}, \omega) G''(\mathbf{k}, \omega + \Omega)[f(\omega) - f(\omega + \Omega)]. \tag{3.25}$$

Eq. (3.25) is a two-particle correlation function describing transport properties. Here $a_{\mathbf{k}}$, $b_{\mathbf{k}}$ are the bare vertices representing for instance quasiparticle charge ($a_{\mathbf{k}} = 1$), current ($a_{\mathbf{k}} = v_{\mathbf{k}}$), Raman scattering ($a_{\mathbf{k}} = \gamma_{\mathbf{k}}$), etc. Differences from various response functions arise from the different vertices. The conductivity response is obtained by selecting the current vertices in Eq. (3.25) and the absorptive part of the conductivity can be expressed via the response function with the general expression

$$\sigma'(\Omega) = \frac{\chi''_{jj}(\Omega)}{\Omega}. \tag{3.26}$$

If the conductivity response is replaced by the Raman response in Eq. (3.26) the equivalence relation is not satisfied due to the differences between the Raman and conductivity response functions. However, since the vertices do not depend strongly on temperature, the conductivity multiplied by the frequency and the Raman response should show the same qualitative temperature dependence, and the comparison of the evolution with temperature of these two quantities is justified, if correlations do not play an important role. Moreover, it has been explicitly shown that under certain restrictions the imaginary part of the Raman response and the real part of the conductivity multiplied by the frequency are proportional [118]

$$\Omega\sigma'(\Omega) \propto \chi''_{\gamma\gamma}(\Omega), \tag{3.27}$$

providing an explicit justification for the comparison of these two quantities.

In the static limit $\Omega \to 0$ an explicit expression for an effective scattering rate can be derived. The Green's function in Eq. (3.24) can be written as

$$\begin{aligned} G(\mathbf{k},\omega,T) &= \frac{1}{\omega - \xi_{\mathbf{k}} - \omega\frac{\partial\sum'}{\partial\omega}(0,T) - i\sum''(\mathbf{k},\omega,T)} + G_{\mathrm{INC}} \\ &= \frac{1}{1 - \frac{\partial\sum'}{\partial\omega}(\mathbf{k},0,T)}\frac{1}{\omega - \overline{\xi}_{\mathbf{k}} - i\overline{\sum}''(\mathbf{k},\omega,T)} + G_{\mathrm{INC}} \\ &= \frac{Z(\mathbf{k},\omega,T)}{\omega - \overline{\xi}_{\mathbf{k}} - i\overline{\sum}''(\mathbf{k},\omega,T)} + G_{\mathrm{INC}}, \end{aligned} \tag{3.28}$$

where $Z(\mathbf{k},\omega,T) = (1-\partial\Sigma'(\mathbf{k},\omega,T)/\partial\omega)^{-1}$ is the quasiparticle residue, $\overline{\xi}_{\mathbf{k}} = \xi_{\mathbf{k}}/\left(1-\frac{\partial\sum'}{\partial\omega}(\mathbf{k},0,T)\right)$ and $\overline{\sum}''(\mathbf{k},\omega,T) = \sum''(\mathbf{k},\omega,T)/\left(1-\frac{\partial\sum'}{\partial\omega}(\mathbf{k},0,T)\right)$ are the renormalized energy band dispersion and renormalized imaginary part of the self energy, respectively, and G_{INC} contains the contribution to higher orders in the Taylor expansion of the self energy. In the limit $\Omega \to 0$ the Raman response [119, 34] reads

$$\chi''_{\mu}(\Omega\to 0) = \Omega N_F \left\langle \gamma^2_{\mu}(\mathbf{k}) \int \frac{d\xi \left(-\frac{\partial f^0}{\partial\xi}\right) Z^2(\mathbf{k},\xi,T)}{2\Sigma''(\mathbf{k},\xi,T)} \right\rangle, \tag{3.29}$$

where N_F is the density of electronic levels at the Fermi Energy, f^0 is the equilibrium Fermi distribution function, and $\langle\cdots\rangle$ denotes an average over the Fermi surface. The imaginary part of the self energy Σ'' determines the lifetime of quasiparticle placed into the state $\mathbf{k}$ via the relation $\hbar/2\Sigma''(\mathbf{k},\omega,T) = \tau_{\mathbf{k}}(\omega,T)$. The inverse of the initial slope of the Raman response function provides an effective scattering rate of the quasiparticles

$$\left(\frac{\partial\chi''_{\mu}(\Omega)}{\partial\Omega}\right)^{-1}_{\Omega=0} \propto \Gamma^{\mu}_0(T). \tag{3.30}$$

From the effective scattering rate a quantity that can be best thought of as Raman resistivity can be extracted. It is important to mention that Raman resistivity and conventional resistivity are different and their comparison needs some care. Again differences arise from the different vertices, and a complete quantitative agreement cannot be expected. However, as long as correlation effects are not strong the comparison of the temperature dependence of the Raman and conventional resistivity is in general justified.

The comparison of the Raman and conventional resistivity will be shown and discussed in chapter 5 and 6.

3.7 Memory-function approach

The electron dynamics can be analyzed with a method which was originally introduced for the current-current correlation function [120], applied subsequently to the analysis of infrared data [121], and recently developed for the Raman response [122]. This method consists in writing the Raman response in terms of a (Raman) memory function

$$M_R(z) = \frac{z\chi(z)}{1-\chi(z)}. \tag{3.31}$$

Though the Raman memory function is different from the conductivity memory function its analytic properties are the same. $M_R(z)$ is holomorphic for all non real z and obeys the symmetry relations $M_R^*(z) = M_R(z^*)$ and $M_R(z) = -M_R(-z)$. Consequently, $M_R(z)$ can be represented by a spectral integral

$$M_R(z) = \frac{1}{\pi}\int_\infty^\infty d\xi \frac{M_R''(\xi)}{\xi - z}, \tag{3.32}$$

where $M_R''(\omega)$ is the analytical continuation of $M_R(z)$ to the real axis,

$$M_R(\Omega \pm i0) = M_R'(\Omega) \pm iM_R''(\Omega). \tag{3.33}$$

Solving Eq. (3.31) for χ one obtains the representation of the susceptibility in terms of the memory function M. After performing the continuation to the real axis the susceptibility in terms of the memory function reads

$$\chi(\Omega) = \frac{M_R(\Omega)}{\Omega + M_R(\Omega)}. \tag{3.34}$$

With

$$M_R(\Omega) = \Omega\lambda(\Omega) + i\Gamma(\Omega), \tag{3.35}$$

the imaginary part of the Raman response function reads

$$\chi''(\Omega) = \frac{\Omega\Gamma(\Omega)}{\Omega^2(1+\lambda(\Omega))^2 + \Gamma^2(\Omega)}. \tag{3.36}$$

In the hypothesis of a self energy independent of **k** the imaginary part of the Raman response function assumes the same structure of Eq. (3.36) with $\Gamma(\Omega)$ replaced by $\sum''(\Omega)$ and λ replaced by $-\partial \sum' / \partial \Omega$. Therefore $\Gamma(\Omega)$ corresponds to a dynamical relaxation rate of the carriers and $1 + \lambda(\Omega) = m^*/m$ to the mass-enhancement factor.

In order to extract $\Gamma(\Omega)$ and $1 + \lambda(\Omega)$ from the imaginary part of the Raman response it is convenient to define the function

$$I(\Omega) = \chi''(\Omega)/\Omega. \tag{3.37}$$

The expressions for $\Gamma(\Omega)$ and $1 + \lambda(\Omega)$ read

$$\begin{aligned} \Gamma(\Omega) &= R\frac{I(\Omega)}{I^2(\Omega) + \Omega^2 K^2(\Omega)} \\ 1 + \lambda(\Omega) &= R\frac{K(\Omega)}{I^2(\Omega) + \Omega^2 K^2(\Omega)}. \end{aligned} \tag{3.38}$$

The function $\Omega K(\Omega)$ is the Kramers-Krönig (KK) transform of $I(\Omega)$,

$$K(\Omega) = -\frac{2}{\pi}\mathcal{P}\int_0^\infty \frac{I(\xi)}{\xi^2 - \Omega^2} d\xi, \tag{3.39}$$

where $\mathcal{P}$ indicates the principal value of the integral. The normalizing factor R is fixed by a sum rule

$$R = \frac{2}{\pi}\int_0^\infty I(\Omega) d\Omega. \tag{3.40}$$

The Raman relaxation rates obtained in this work are extracted from the data following this approach. The static rates which will be compared to the resistivity (chapter 6) are obtained by extrapolating the dynamic results to $\Omega = 0$. For the conversion of the resistivity into relaxation rates a Drude model is used,

$$\frac{1}{\tau} = \epsilon_0 \omega_{\mathrm{pl}}^2 \rho, \tag{3.41}$$

where ϵ_0 is the permittivity of free space, ω_{pl} the plasma frequency, and ρ the

resistivity. Expressing the Raman rates in cm^{-1}, $\hbar\omega_{\mathrm{pl}}$ in eV and ρ in $\mu\Omega$cm the conversion relation reads

$$\Gamma = \frac{\hbar}{\tau} = 1.08(\hbar\omega_{\mathrm{pl}})^2\rho. \tag{3.42}$$

Chapter 4

Experimental details

In this chapter the samples studied and the experimental techniques used will be described. In addition, details on the doping and the annealing conditions as well as the data treatment will be explained.

4.1 Samples

In order to distinguish between features intrinsic of all cuprates and features related to a specific material class a comparison of different compounds is necessary. In this work two different cuprates families have been selected: $La_{2-x}Sr_xCuO_4$ and $(Y_{1-y}Ca_y)Ba_2Cu_3O_{6+x}$ (Y-123). $La_{2-x}Sr_xCuO_4$ is chosen for the availability of single crystals at very low doping levels and in order to compare the Raman data with measurements performed with other experimental techniques. $(Y_{1-y}Ca_y)Ba_2Cu_3O_{6+x}$ is selected for its superior crystal quality and for the possibility to dope via the substitution of Y by Ca. Ca allows one to finely change the doping in a reliable fashion without introducing strong charge trapping defects [123].

4.1.1 $La_{2-x}Sr_xCuO_4$

$La_{2-x}Sr_xCuO_4$ belongs to the class of monolayer materials with only one CuO_2 plane per unit cell. At sufficiently high temperature it is characterized by the

body-centred tetragonal structure shown in Fig. 4.1. In the centre of the unit cell there is an octahedron formed by O atoms surrounding a Cu atom. LaSrO planes form the charge reservoir between the conducting planes. Each Cu atom in the CuO_2 planes has an O atom above and below in c-direction called apical O. The stronger bonds are those in the planes, since the Cu-O distance in the c-direction ($\approx$ 2.4 Å) is larger than that in the planes ($\approx$ 1.9 Å).

Lowering the temperature the material undergoes a structural phase transition where the tetragonal structure transforms to one with orthorhombic symmetry, because of the staggered tilt of the CuO_6 octahedra [124]. In the antiferromagnetic insulator La_2CuO_4 the transition temperature is approximately 520 K which is suppressed by about 20 K per percent Sr concentration [124].

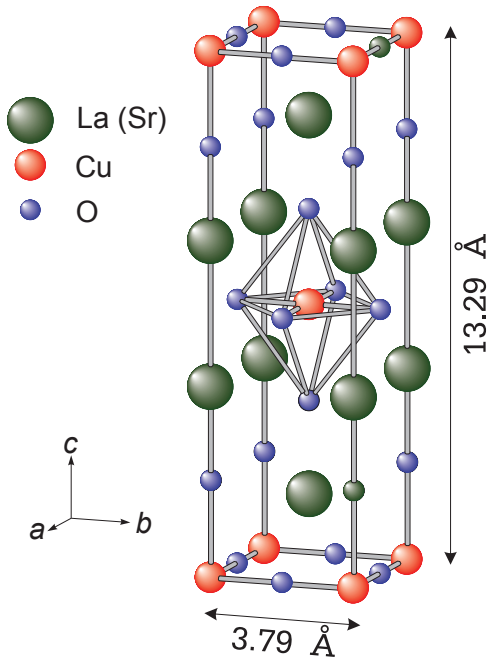

Figure 4.1: *Crystal structure of* $La_{2-x}Sr_xCuO_4$.

The oxidation state in the crystal is La^{3+}, O^{2-}, and in order to conserve the charge neutrality Cu is in the $3d^9$, i.e. 2+ state with a net spin of 1/2. To dope the material, La^{3+} is substituted by Sr^{2+} which results in removing electrons from the CuO_2 planes. The doping level p corresponds to the Sr concentration ($p = x$). For Sr concentrations between $x \approx 0.05$ and $x \approx 0.27$ the material is superconducting [125], and the maximum transition temperature is $T_c \approx 40$ K at $x \approx 0.16$.

La can also be partially replace by Ba. Ba is also 2+ and has the same effect as Sr. $La_{1.875}Ba_{0.125}CuO_4$ and $La_{1.875}Ba_{0.125-x}Sr_xCuO_4$ undergo an additional structural phase transi-

tion below a temperature T_{d2} where the structure changes from orthorhombic to tetragonal [126, 73]. The latter structure is usually referred to as low-temperature tetragonal (LTT) phase in the literature. The transition temperature T_{d2} of $La_{1.875}Ba_{0.125-x}Sr_xCuO_4$ depends on the Sr concentration. At $x \gtrsim 0.08$ and below T_{d2} an additional structural transition occurs, where the structure changes from LTT to low-temperature less-orthorhombic (LTLO) [73]. The partial substitution of La by Ba leads also to the formation of static charge and spin modulation as sketch in Fig. 2.8 [73, 19]. The LTT phase, and the static charge and spin modulation are associated with a depression of T_c [73, 127].

In this work three underdoped La-based single crystals were measured: $La_{1.98}Sr_{0.02}CuO_4$, $La_{1.88}Sr_{0.12}CuO_4$ and $La_{1.875}Ba_{0.075}Sr_{0.05}CuO_4$. Results from a previously measured $La_{1.90}Sr_{0.10}CuO_4$ crystal were used for comparison. $La_{1.98}Sr_{0.02}CuO_4$ and $La_{1.90}Sr_{0.10}CuO_4$ were prepared by N. Kikugawa and T. Fujita at Hiroshima University, while $La_{1.88}Sr_{0.12}CuO_4$ and $La_{1.875}Ba_{0.125-x}Sr_xCuO_4$ were grown by K. Yamada and M. Fujita at the Tohoku University and at the Institute for Chemical Research in Kyoto. All the crystals were grown by travelling-solvent-floating-zone (TSFZ) technique and the Sr content was determind by energy dispersive X-ray spectroscopy. The measurements were performed on polished surfaces. After polishing the $La_{1.98}Sr_{0.02}CuO_4$ and $La_{1.90}Sr_{0.10}CuO_4$ samples were reannealed in flowing O_2 for 50 hours at 920 °C, cooled down to 500 °C in 50 hours, and kept for another 50 hours at this temperature. Finally, they were cooled down to ambient temperature in 50 hours. This procedure ensures that the crystal surface was strain free. $La_{1.88}Sr_{0.12}CuO_4$ and $La_{1.875}Ba_{0.125-x}Sr_xCuO_4$ were measured directly after polishing. The transition temperature T_c of $La_{1.90}Sr_{0.10}CuO_4$ was determined from the in-plane resistivity ρ_{ab}, and for $La_{1.88}Sr_{0.12}CuO_4$ and $La_{1.875}Ba_{0.075}Sr_{0.05}CuO_4$ via the magnetic susceptibility. The properties of the La-based samples studied are summarized in Tab. 4.1.

$La_{2-x-y}Ba_ySr_xCuO_4$	T_c	p	Annealing
$La_{1.98}Sr_{0.02}CuO_4$	not SC	0.02	50 h at 920 °C; cooled down to 500 °C in 50 h; 50 h 500 °C; cooled down to ambient T in 50 h
$La_{1.90}Sr_{0.10}CuO_4$	28 K	0.10	50 h at 920 °C; cooled down to 500 °C in 50 h; 50 h 500 °C; cooled down to ambient T in 50 h
$La_{1.88}Sr_{0.12}CuO_4$	31.5 K	0.12	50 h at 900 °C; cooled down to 500 °C, 10 °C per h; 50 h 500 °C; cooled down slowly to ambient T
$La_{1.875}Ba_{0.075}Sr_{0.05}CuO_4$	10 K	0.12	50 h at 900 °C; cooled down to 500 °C, 10 °C per h; 50 h 500 °C; cooled down slowly to ambient T

Table 4.1: *La-based samples studied. The corresponding transition temperatures T_c, doping levels p, and annealing parameters are indicated.*

4.1.2 $(\mathbf{Y_{1-y}(Ca_y)Ba_2Cu_3O_{6+x}}$

The structure of $(Y_{1-y}Ca_y)Ba_2Cu_3O_{6+x}$, shown in Fig. 4.2, consists of two adjacent CuO_2 planes separated by Y ions. Each pair of CuO_2 planes is separated by layers of atoms containing Ba, O and Cu, which act as charge reservoir. The O atoms of the conducting planes are shifted toward the interior of the bilayer giving rise to a buckling of the CuO_2 planes [128].

The standard way of doping is to increase the O content of the parent compound. The additional O atoms occupy the sites between the Cu (1) atoms (chain sites), along the b direction. For $x = 1$ every place between Cu atoms is occupied, and the "Cu-O chains" form a regular array. At $x = 0$ the oxidation states are Y^{3+}, Ba^{2+}, Cu^{2+} in the planes, Cu^{1+} in chains, and O^{2-}. The concentration of carriers in the conducting planes is modified by altering the O content in the Cu-O chains. Additional O turns Cu^{1+} into Cu^{2+} and attracts electrons from the CuO_2 planes thus creating holes.

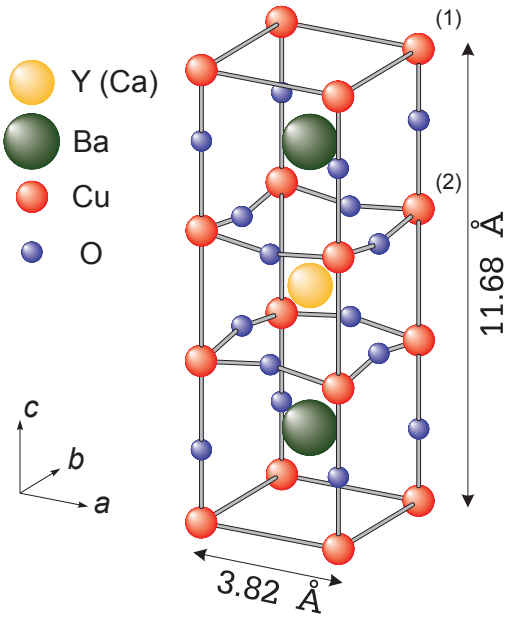

Figure 4.2: *Crystal structure of* $(Y_{1-y}Ca_y)Ba_2Cu_3O_{6+x}$.

For x close to 0, long range antiferromagnetism is observed. Above $x \approx 0.2$ ($p \approx 0.035$) a transition into a short range antiferromagnetically correlated spin-glass-like state is observed [129] and above $x = 0.353$ ($p \approx 0.05$) superconductivity evolves [130]. The maximal T_c is found at $x \approx 0.93$. At $x \approx 0.4$ a structural phase transition occurs from a tetragonal at lower doping levels to an orthorhombic phase at higher concentrations [131]. The conduction planes are almost unaffected by this transition.

O doping has two disadvantages: it breaks the tetragonal symmetry above $x \approx 0.4$ and it is very difficult to obtain high quality samples with a reliable doping level below the onset point of superconductivity.

A different way to vary the carrier concentration of $(Y_{1-y}Ca_y)Ba_2Cu_3O_{6+x}$ is to replace trivalent Y by bivalent Ca. The doping is given by the Ca content divided by 2 ($p \approx y/2$). Doping with Ca allows one to control the number of holes close to the antiferromagnetic phase without introducing strong charge trapping defects [123]. Furthermore it allows one to perform experiments in a tetragonal structure. Doping levels up to $p \approx 0.06$ were achieved with Ca. To induce superconductivity a small amount of O was necessary ($y = 0.08, x = 0.3$). The doping level of the superconducting sample was estimated from the transition temperature $T_c = 28$ K via the universal relationship $T_c(p)$ [40].

All the $(Y_{1-y}Ca_y)Ba_2Cu_3O_{6+x}$ single crystals studied in this work were prepared by A. Erb at the Walther Meissner Institut. They were grown in

the inert crucible material $BaZrO_3$ which facilitating the highest purity [132].

As grown $(Y_{1-y}Ca_y)Ba_2Cu_3O_{6+x}$ samples are close to optimal doping, ($x \approx 0.9$). The concentration of O can be varied by annealing the samples under the appropriate conditions of temperature and O partial pressure, as shown in Fig. 4.3 [133]. In order to reach an O concentration of approxi-

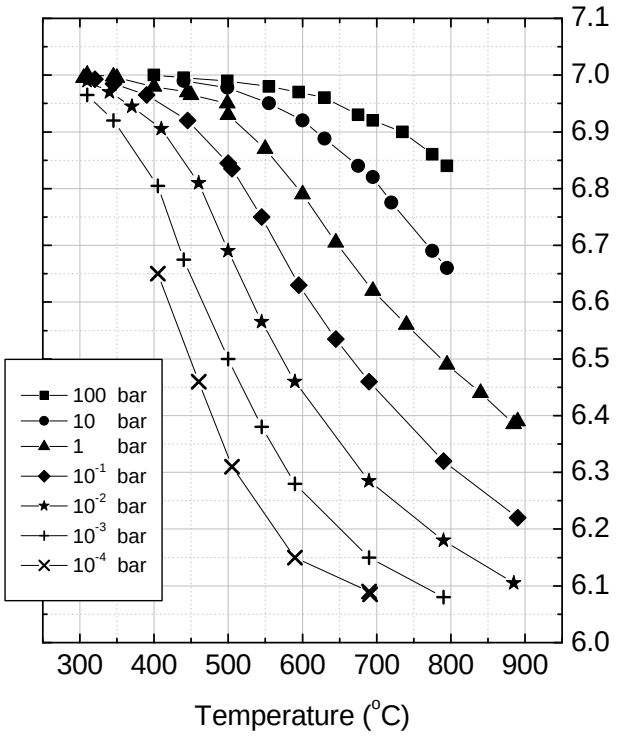

Figure 4.3: *Oxygen content of* $(Y_{1-y}Ca_y)Ba_2Cu_3O_{6+x}$ *as a function of the temperature and the O partial pressure according to the calibration of Lindermer et al. [133].*

mately 6.05 the samples were annealed for one week at 800 °C in a pure argon atmosphere. The characteristic of the samples studied in this work and the annealing parameters are summarized in Tab. 4.2.

$(Y_{1-y}Ca_y)Ba_2Cu_3O_{6+x}$	T_c	p	Annealing
$YBa_2Cu_3O_6$	Not SC	0	800 °C for one week in Ar atmosphere
$Y_{1.98}Ca_0.02Ba_2Cu_3O_6$	Not SC	0.01	800 °C for one week in Ar atmosphere
$Y_{1.97}Ca_{0.03}Ba_2Cu_3O_6$	Not SC	0.015	800 °C for one week in Ar atmosphere
$Y_{1.92}Ca_{0.08}Ba_2Cu_3O_6$	Not SC	0.04	800 °C for one week in Ar atmosphere
$Y_{1.88}Ca_{0.12}Ba_2Cu_3O_6$	Not SC	0.06	800 °C for one week in Ar atmosphere
$Y_{1.88}Ca_{0.08}Ba_2Cu_3O_{6.30}$	28 K	0.07	800 °C in 0.1 bar O partial pressure for one week
$YBa_2Cu_3O_{6.30}$	Not SC	0.04	850 °C in 0.1 bar O partial pressure for one week
$YBa_2Cu_3O_{6.40}$	26 K	0.07	750 °C in 0.1 bar O partial pressure

Table 4.2: *$(Y_{1-y}Ca_y)Ba_2Cu_3O_{6+x}$ samples studied, with the corresponding transition temperature T_c, doping level p, and annealing parameters.*

4.2 Measurements of T_c

A precise determination of the doping level of the samples is a problem of primary importance. A convenient non destructive way to determine the doping level of a superconducting sample is through the measurement of the critical temperature T_c [40]. Here a technique originally introduced to measure both the critical current J_c and the transition temperature T_c in high-temperature oxides [134] was used.

The method consists of measuring the third harmonic component of the *ac*-susceptibility of the sample. The non linear components of the *ac*-susceptibility are a measure of the losses induced by flux motion in a type-II superconductor. Above T_c the non linear response is vanishingly small. Well below T_c the critical current J_c is greater than the current induced by the *ac* magnetic field in the sample, and in this regime the dissipation is small and the third harmonic is again too small to give a detectable signal. On

the other hand close to T_c, J_c drops to zero and a hysteresis occurs in the presence of an alternating magnetic field. The non-linear response generates an anharmonic signal.

This technique has several advantages for the purpose of this work. (1) it is contactless leaving the surface unaffected. (2) it is sensitive to sample inhomogeneities, and, compared to simple susceptibility measurements, it has a much higher sensitivity that allows the measurement of a signal at the superconducting transition also in samples with sub-millimeter dimensions. Finally the measurement itself is experimentally relatively simple and fast. Details of the technique and of the setup used can be found in Ref. [135].

4.3 Setup for the Raman experiments

The experimental setup for Raman scattering experiments is schematically shown in Fig. 4.4. The light source is a commercial Ar^+ laser (Coherent Innova 304). The lines at 458, 476, 488, 505, 514, 528 nm have been used to investigate the dependence of the inelastically scattered light upon the excitation energy.

The laser light is first spatially filtered. The spatial filter consists of two achromatic lenses with focal length $f = 30$ mm and $f = 50$ mm for L1 and L2, respectively, and a pin-hole with diameter 30 μm. As a result the radiation propagating in different directions with respect to the laser light is blocked. A spectral filtering is achieved by the prism monochromator (PMC) that together with an adjustable slit (S2) between two achromatic lenses both with $f = 100$ mm (L1 and L2) allow the rejection of lines which differ from the laser line by more than 30 cm^{-1}.

With a Glan-Thompson polarizer (P1) it is possible to prepare linearly polarized light. A Soleil-Babinet compensator (CM), placed after the polarizer (P1) allows one to precisely adjust the desired polarization state of the light incident on the sample. A $\lambda/2$-retardation plate placed just before the polarizer rotates the polarization of the laser light and allows the adjustment

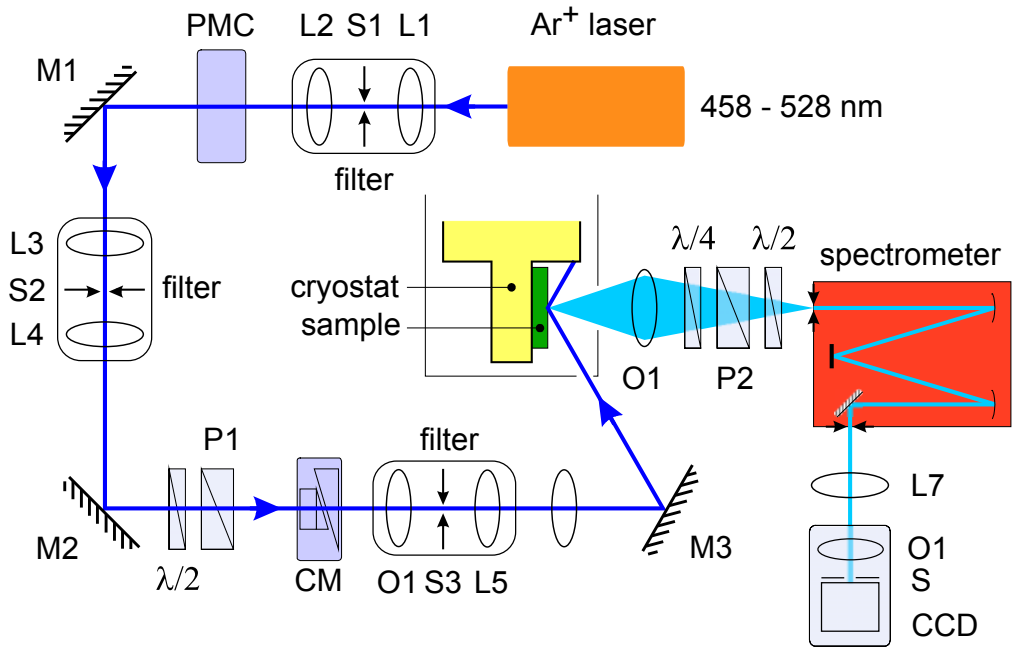

Figure 4.4: *Sketch of the Raman setup. L1-L7 are achromatic lenses; S1 and S3 pin-holes; S2 slit; PMC prism-monochromator; M1-M3 mirrors;P1-P2 polarizer;CM Soleil-Babinet compensator; O1-O3 objectives; S shutter.*

of the incident power.

Another spatial filter, consisting of a microscope objective lens (Spindler and Hoyer, x10) (O1), a pin-hole with a diameter of 20 μm (S3), and an achromatic lens with focal length $f = 30$ mm (L5), is used to obtain a Gaussian beam. A last achromatic lens with $f = 250$ mm (L6) focuses the laser beam on the sample. The angle of incidence is adjusted according to the optical constants of the sample in order to minimize the reflected intensity of parallel polarized light.

The sample is placed in a He-flow cryostat. The cryostat has a cryopumped vacuum chamber operating at a pressure of approximately 5×10^{-7} mbar. The temperature of the cold finger can be adjusted between approximately 1.5 and 350 K, and is measured by a Si diode on the sample holder. Details of the cryogenic equipment can be found in reference [136].

In order to exploit the Raman selection rules a precise orientation of the

sample is required. The orientation of the a and b crystalline axes is determined with a Laue camera. The sample is mounted into the cryostat with the a and b axes parallel or at 45° with respect to the x and y directions of the laboratory frame. A sketch of the scattering geometry (for a and b parallel to the x and y directions) is shown in Fig. 4.5. The polarized laser light hits the sample at an angle of incidence of approximately 60°; the directly reflected light is absorbed by a beam stopper.

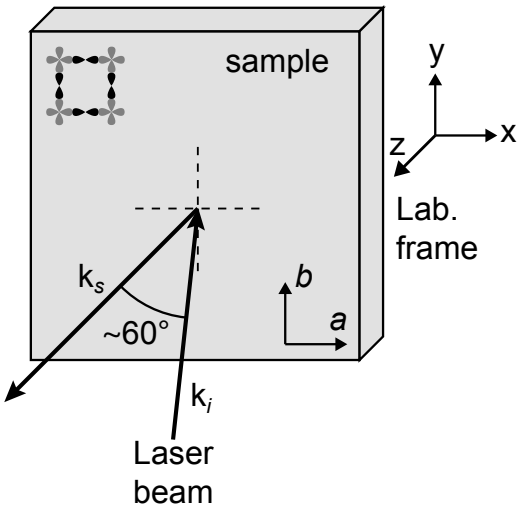

Figure 4.5: *Details of the sample orientation and scattering geometry.*

The inelastically scattered light is collected and focussed on the entrance slit of the spectrometer by a camera objective lens (O2) (Minolta, $f = 58$ mm, 1:1.4). The desired polarization state of the scattered light is selected by a $\lambda/4$-retardation plate and a second polarizer (P2). In this way, both linearly and circularly polarized photons can be selected. A $\lambda/2$ plate placed in front of the entrance slit of the spectrometer rotates the linearly polarized light into the direction of maximal transmission of the spectrometer.

The spectrometer is a Jarrel-Ash 25-100 double monochromator with Czerny-Turner configuration. The two monochromator stages are identical and subtractively coupled (Fig. 4.6). The light focussed on the entrance slit is transformed into a parallel beam by the first spherical mirror (SM1). The first grating (G1) disperses the light. Part of the dispersed light is collected by the second spherical mirror (SM2) and focussed on the intermediate slit to enter a second identical stage which produces an image of the entrance slit on the exit slit. The frequency range on the exit slit is determined by the width of the intermediate slit.

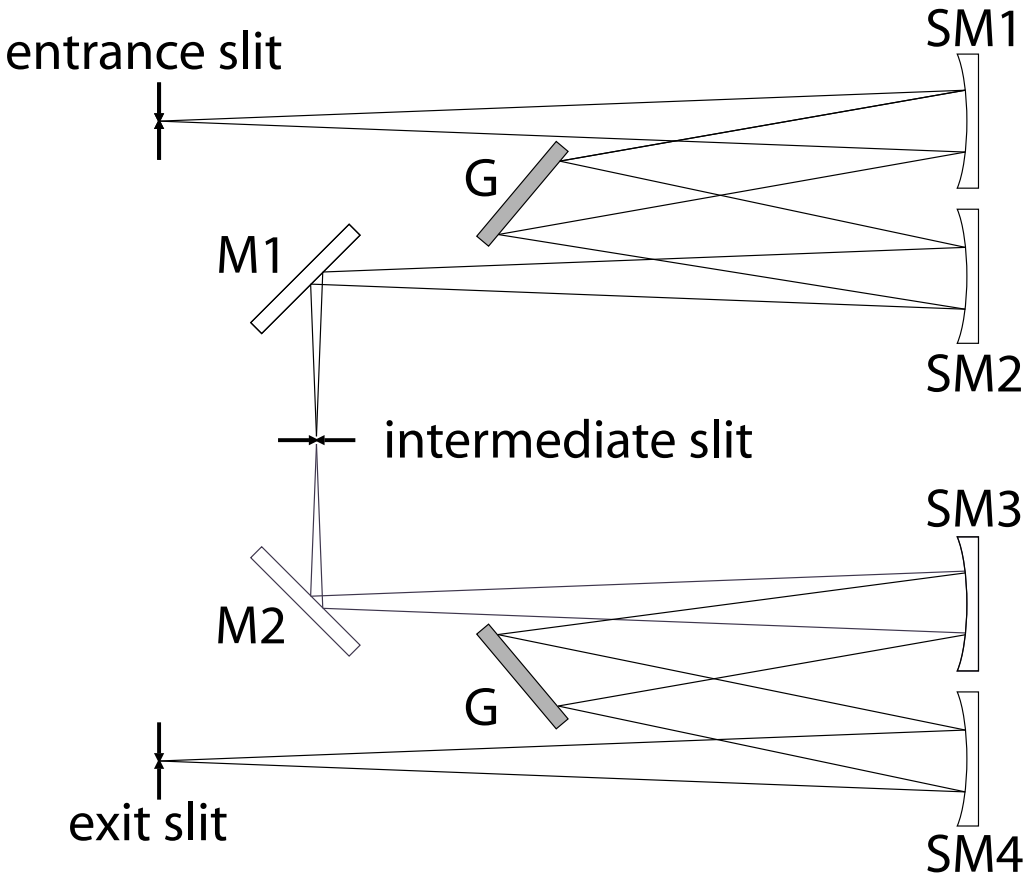

Figure 4.6: *Sketch of the double monochromator used for the Raman measurements. SM1-SM4 are spherical mirrors, M1-M2 planes mirrors and G gratings.*

The transmitted light is focussed on a cryogenically cooled CCD detector (Tektronic TK-512). Since the spectrometer is operated in subtractive mode the spectra are acquired point by point.

The measured data are corrected for the sensitivity of optics, spectrometer, and CCD, and normalized to the slit width, the acquisition time, and the absorbed power. The band width was set at approximately 5, 10, or 40 cm^{-1} depending on the required resolution. The intensity of the scattered signal is given in units of photon counts per second and mW (cps/mW). The temperatures have to be corrected for the laser heating and are determined via the comparison of Stokes and anti-Stokes spectra [137].

Chapter 5

Results

In this chapter the experimental results are presented. Here only the raw data are shown. The spectra are normalized for the acquisition time, slit width, and absorbed power, and corrected for the sensitivity curve of the spectrometer and divided by the Bose factor. Data analysis, discussion and conclusions are in Chapter 6.

5.1 Experimental results in La-based material

In this section results on La-based cuprates (see Tab 4.1) are shown. Results on $La_{1.90}Sr_{0.10}CuO_4$ previously measured [135] will be also shown for comparison. The intensity scales are absolute.

5.1.1 Raman response of $La_{2-x}Sr_xCuO_4$ at $p = 0.02$ and 0.10

The electronic Raman response $\chi''(\Omega, p, T)$ of $La_{1.98}Sr_{0.02}CuO_4$ ($p = 0.02$) and $La_{1.90}Sr_{0.10}CuO_4$ ($p = 0.10$) for B_{1g} and B_{2g} symmetry is shown in Fig. 5.1. The intensities of the B_{2g} spectra at $p = 0.10$ (Fig. 5.1 (d)) merge above approximately 300 cm^{-1}. At low energy the temperature dependence is stronger

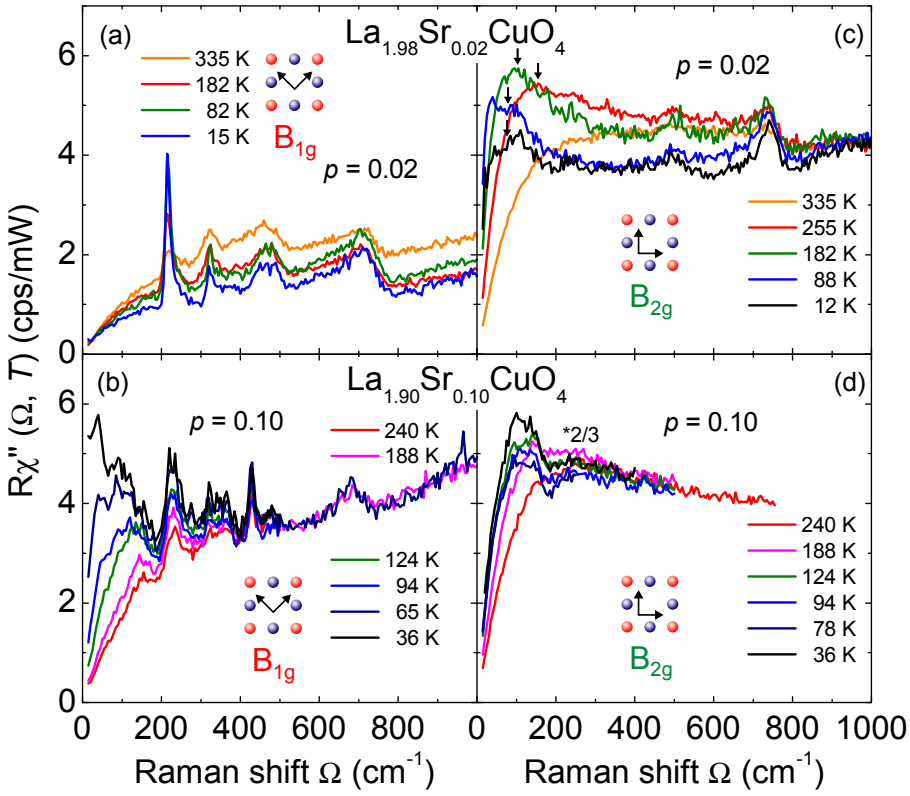

Figure 5.1: *Electronic Raman response $\chi''(\Omega, T)$ of $La_{1.98}Sr_{0.02}CuO_4$ ($p = 0.02$) and $La_{1.90}Sr_{0.10}CuO_4$ ($p = 0.10$) at different temperatures as indicated in the figures. In panels (a) and (c) results at $p = 0.02$ for B_{1g} and B_{2g} symmetries, respectively, are shown. In panels (b) and (d) results at $p = 0.10$ for B_{1g} and B_{2g} symmetries, respectively, are shown. The data of $La_{1.90}Sr_{0.10}CuO_4$ are reproduced from Ref. [135].*

and the spectral weight increases upon cooling. The initial slope of the B_{2g} spectra, proportional to the lifetime of the carriers (see Sect. 3.6), increases upon lowering the temperature, indicating metallic behaviour.

The B_{1g} spectra at $p = 0.10$ (Fig. 5.1 (b)) show sharp features superimposed on the electronic continuum corresponding to lattice vibrations. The spectra at different temperatures merge above approximately 450 cm^{-1}. At $\Omega \leq 200$ cm^{-1} the spectra show a strong temperature dependence with the spectral weight and the initial slope increasing upon cooling.

The B_{2g} Raman response at $p = 0.02$ is shown in Fig. 5.1 (c). The spectra

show a strong temperature dependence and the initial slope increases upon cooling. In contrast to $p = 0.10$ there is a temperature dependent peak which moves to lower energies upon cooling. The spectra show a suppression of intensity below approximately 900 cm^{-1}, which prevents the development of an isolated peak at low energy.

In Fig. 5.1 (a) the B_{1g} spectra at $p = 0.02$ and various temperatures are shown. The low-energy part of the spectra reacts mildly to temperature changes, and the initial slope decreases upon cooling. The overall intensity decreases upon cooling.

5.1.2 Raman response of $La_{1.88}Sr_{0.12}CuO_4$ and $La_{1.875}Ba_{0.075}Sr_{0.05}CuO_4$

In this section results on two different La-based compounds close to 1/8 doping, $La_{1.88}Sr_{0.12}CuO_4$ and $La_{1.875}Ba_{0.075}Sr_{0.05}CuO_4$ are shown.

The B_{1g} Raman responses of $La_{1.88}Sr_{0.12}CuO_4$ and $La_{1.875}Ba_{0.075}Sr_{0.05}CuO_4$ at different temperatures are plotted in Fig. 5.2 (a) and (b), respectively. The spectra of the two samples are similar, showing practically the same temperature dependence. Below $\Omega \sim 200$ cm^{-1} the temperature dependence is strong with a peak emerging at low temperature.

The B_{2g} spectra of $La_{1.88}Sr_{0.12}CuO_4$ are shown in Fig. 5.2 (c). The spectra merge above $\Omega \approx 300$ cm^{-1}. At low energy the spectral weight and the initial slope increase upon cooling, showing the same qualitative behaviour as the spectra of $La_{1.90}Sr_{0.10}CuO_4$ (see Fig. 5.1 (d)).

The B_{2g} Raman spectra of $La_{1.875}Ba_{0.075}Sr_{0.05}CuO_4$, plotted in Fig. 5.2 (d), merge similarly as those of $La_{1.88}Sr_{0.12}CuO_4$. The low-energy spectral weight and the initial slope increase upon lowering the temperature down to $T \approx 40$ K, in a similar way as the spectra of $La_{2-x}Sr_xCuO_4$ at $p = x = 0.10$ and 0.12. Below $T \approx 40$ K the Raman response of $La_{1.875}Ba_{0.075}Sr_{0.05}CuO_4$ changes qualitatively with respect to the Raman response of $La_{1.88}Sr_{0.02}CuO_4$. Spectral weight is suppressed at low energies, up to approximately 500 cm^{-1}.

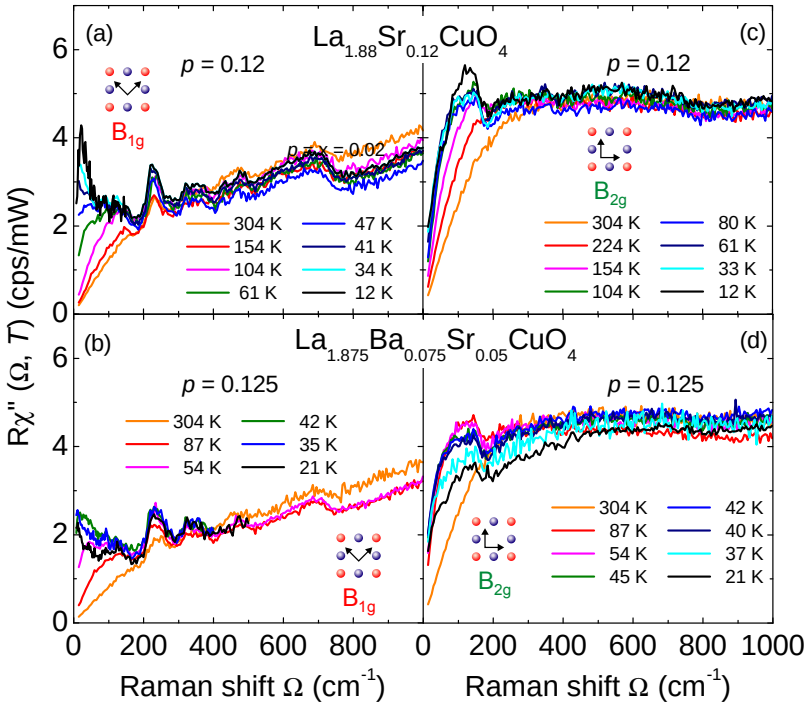

Figure 5.2: *Electronic Raman response* $\chi''(\Omega, T)$ *of* $La_{1.88}Sr_{0.12}CuO_4$ *(*$p = 0.12$*) and* $La_{1.875}Ba_{0.075}Sr_{0.05}CuO_4$ *(*$p = 0.125$*) for* B_{1g} *((a) and (b)) and* B_{2g} *((c) and (d)) symmetries at different temperatures as indicated in the figures.*

5.2 Experimental results in $(Y_{1-y}Ca_y)Ba_2Cu_3O_{6+x}$

In this section results on differently doped $(Y_{1-y}Ca_y)Ba_2Cu_3O_{6+x}$ crystals (see Tab. 4.2) are shown. The measurements were performed as a function of temperature, doping, polarization, and excitation energy. The intensity scales are absolute.

5.2.1 Ca vs O doping in $(Y_{1-y}Ca_y)Ba_2Cu_3O_{6+x}$

In order to check whether or not the Raman response shows features related to the specific route along which the doping level is adjusted, data of Ca doped, O doped and Ca and O co-doped $(Y_{1-y}Ca_y)Ba_2Cu_3O_{6+x}$ are compared.

In Fig. 5.3 (a) the B_{1g} spectra of $(Y_{0.92}Ca_{0.08})Ba_2Cu_3O_{6.05}$ and $YBa_2Cu_3O_{6.30}$ ($p = 0.04$) are plotted. The data are very similar, and the

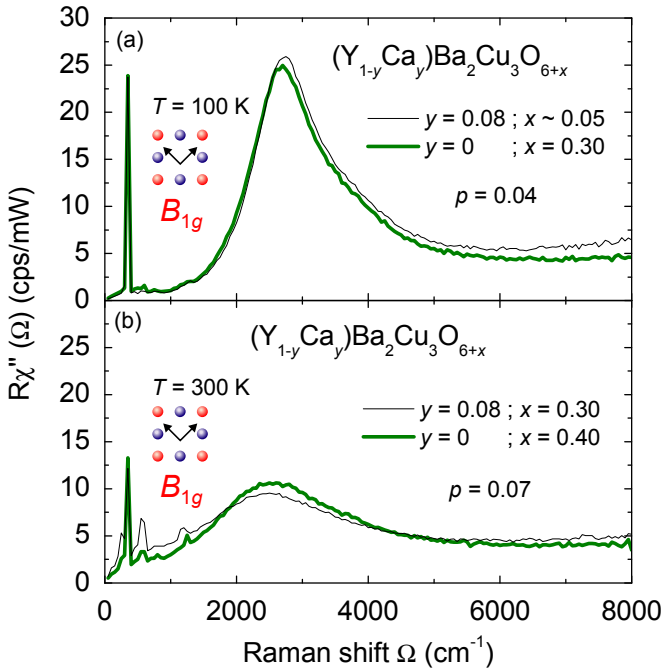

Figure 5.3: *B_{1g} Raman response $\chi''(\Omega)$ of $(Y_{1-y}Ca_y)Ba_2Cu_3O_{6+x}$ at $p = 0.04$ (a) and $p = 0.07$ as indicated in the figure. The quantities x and y refer to the formula and indicate how the doping is achieved.*

large peak around 2800 cm^{-1}, corresponding to the two-magnon excitation, has practically the same spectral shape and energy for both samples. Spectra $(Y_{0.92}Ca_{0.08})Ba_2Cu_3O_{6.30}$ and $YBa_2Cu_3O_{6.40}$ ($p = 0.07$) are plotted in Fig. 5.3 (b). The data show small discrepancies at low and high energies, as well as around the two-magnon peak that can arise from slightly different doping levels. However, the differences between the two superconducting samples are an order of magnitude smaller than the changes across the onset

point of superconductivity $p_{sc1} \approx 0.05$.

Details of the B_{1g} phonon for $(Y_{0.92}Ca_{0.08})Ba_2Cu_3O_{6.05}$ and $YBa_2Cu_3O_{6.30}$ ($p = 0.04$) and for $(Y_{0.92}Ca_{0.08})Ba_2Cu_3O_{6.30}$ and $YBa_2Cu_3O_{6.40}$ ($p = 0.07$) are plotted in Fig. 5.4 (a) and (b), respectively. At $p = 0.04$ the B_{1g} phonons

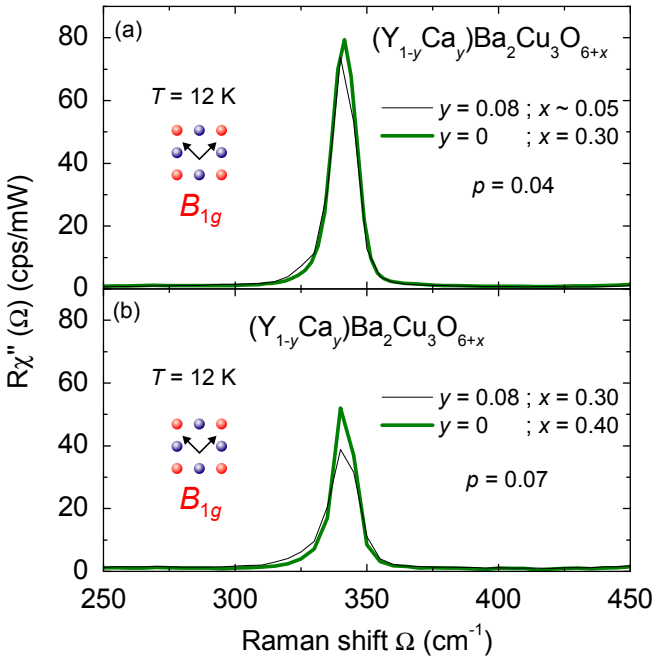

Figure 5.4: *B_{1g} phonon of $(Y_{1-y}Ca_y)Ba_2Cu_3O_{6+x}$ at $p = 0.04$ (a) and $p = 0.07$ (b). The quantities x and y refer to the formula and indicate how the doping is achieved.*

for the Ca and the O doped samples are very similar. The maximum intensity of the phonon of the O doped sample is slightly higher than that of the Ca doped one. At $p = 0.07$ the height of the phonon of the O doped sample is approximately 40% higher than that of the Ca and O co-doped one. However, this difference is much smaller than that between the height of the phonons at $p = 0.04$ and 0.07 that differ by a factor of approximately 2. Moreover, the spectral shape of the B_{1g} phonon for the Ca and O co-doped, and for the O doped samples at $p = 0.07$ are practically equal. Both phonons show an asymmetric profile, being substantially different from the essentially

symmetric one observed at $p = 0.04$.

Finally, the B_{2g} spectra of $(Y_{0.92}Ca_{0.08})Ba_2Cu_3O_{6.05}$ and $YBa_2Cu_3O_{6.30}$ ($p = 0.04$) are plotted in Fig. 5.5. The spectra are practically equal, and both samples show a peak at low energy.

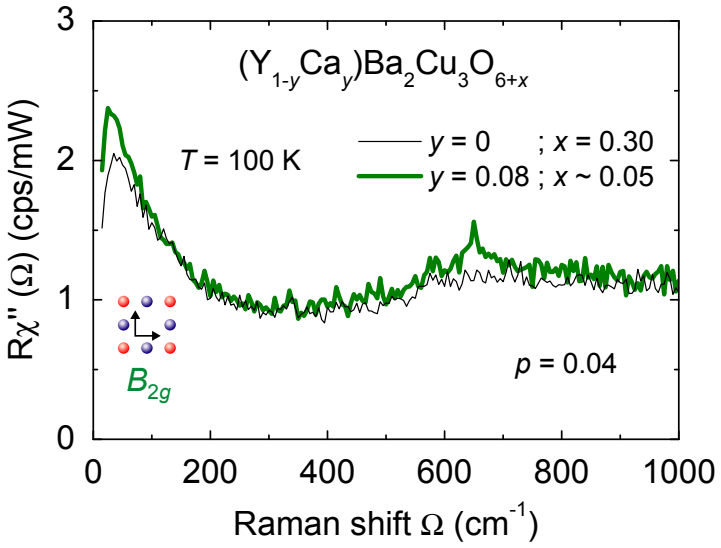

Figure 5.5: *B_{2g} Raman response of $(Y_{1-y}Ca_y)Ba_2Cu_3O_{6+x}$ at $p = 0.04$. The quantities x and y refer to the formula and indicate how the doping is achieved.*

This results show that the Raman response is independent of the specific route along which the carrier concentration is adjusted, at least in the doping range considered in this work. Therefore, only the doping level counts, and apparently Ca and O doping is additive and neither introduces strong disorder for $y < 0.1$ and $x < 0.4$.

5.2.2 High energy B_{1g} Raman response of $(Y_{1-y}Ca_y)Ba_2Cu_3O_{6+x}$

The temperature dependence of the B_{1g} Raman response $\chi''(\Omega, T)$ of differently doped $(Y_{1-y}Ca_y)Ba_2Cu_3O_{6+x}$ samples is shown in Fig. 5.6. The main feature in the B_{1g} spectra is a large peak at approximately 2800 cm^{-1}, corresponding to the two-magnon excitation. Generally, the two-magnon ex-

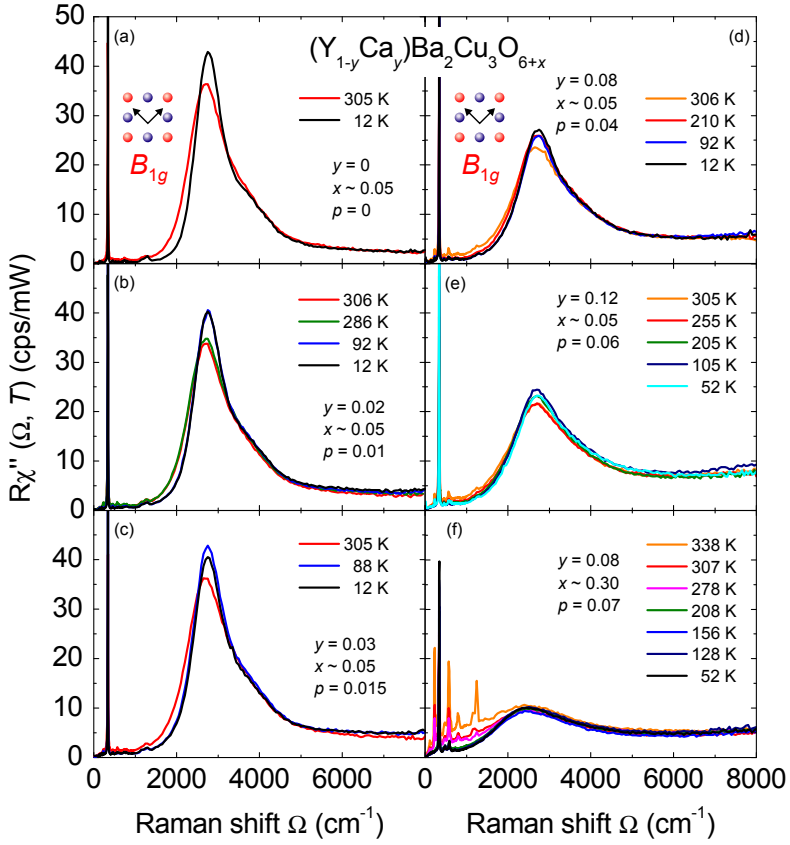

Figure 5.6: *Raman response $\chi''(\Omega, T)$ at various temperatures of differently doped $(Y_{1-y}Ca_y)Ba_2Cu_3O_{6+x}$ samples for the B_{1g} symmetry. In panels (a), (b), (c), (d), (e), and (f) results at $p = 0$, 0.01, 0.015, 0.04, 0.06, and 0.07 are shown, respectively.*

citation reacts only mildly to temperature slightly decreasing towards high temperature.

In order to better visualize the doping dependence of the two-magnon peak, spectra at low temperature and various doping levels are plotted in Fig. 5.7. The two-magnon peak height reduces continuously upon increasing the doping while the energy stays practically constant up to $p = 0.06$. Between $p = 0.06$ and $p = 0.07$ the height of the magnetic excitation drops abruptly and the energy of the peak, decreases by approximately 250 cm^{-1}.

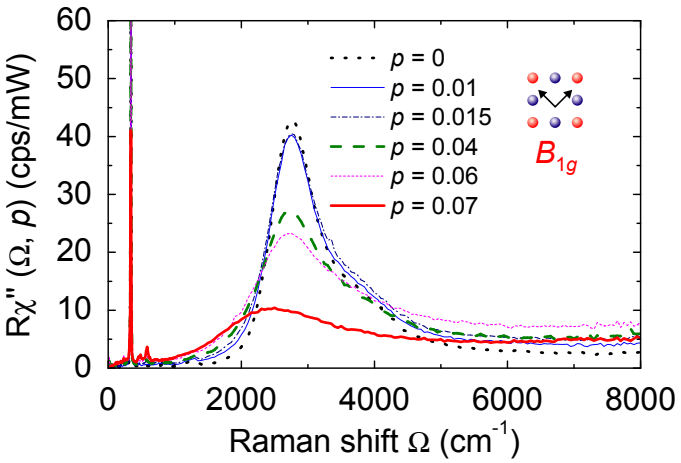

Figure 5.7: *Raman response $\chi''(\Omega, p)$ of differently doped $(Y_{1-y}Ca_y)Ba_2Cu_3O_{6+x}$ single crystals in the normal state at low temperature for the B_{1g}.*

5.2.3 Low energy B_{1g} Raman response of $(Y_{1-y}Ca_y)Ba_2Cu_3O_{6+x}$

A zoom-in on the low-energy Raman response $\chi''(\Omega, T)$ for B_{1g} symmetry is plotted in Fig. 5.8. Independent of doping the initial slope of the spectra decreases upon cooling.

Superimposed on the electronic response there are several sharp peaks corresponding to lattice vibrations such as the B_{1g} phonon at approximately 340 cm^{-1}. The B_{1g} phonon corresponds to an out-of-phase out-of-plane vibration (buckling mode) of the oxygen atoms of the CuO_2 planes. At $p = 0.07$, the intensity of all phonons except for the 340 cm^{-1} mode increase rapidly above approximately 260 K. Apparently, a strong resonance effect of so far unidentified origin sets in. Details of the doping dependence of the B_{1g} phonon are shown in Fig. 5.9. The phonon height stays practically constant in the range $0 < p < 0.06$, while at $p = 0.07$ it drops by a factor of approximately 2.

The phonon spectral shape is symmetric at zero doping. With increasing the doping it develops a shoulder on the low-energy side (Fig. 5.9). The asymmetric shape, hardly visible at $p = 0.04$, becomes substantial at $p = 0.06$ and 0.07. In Fig. 5.10 (a) the B_{1g} phonon of $(Y_{0.88}Ca_{0.12})Ba_2Cu_3O_{6.05}$

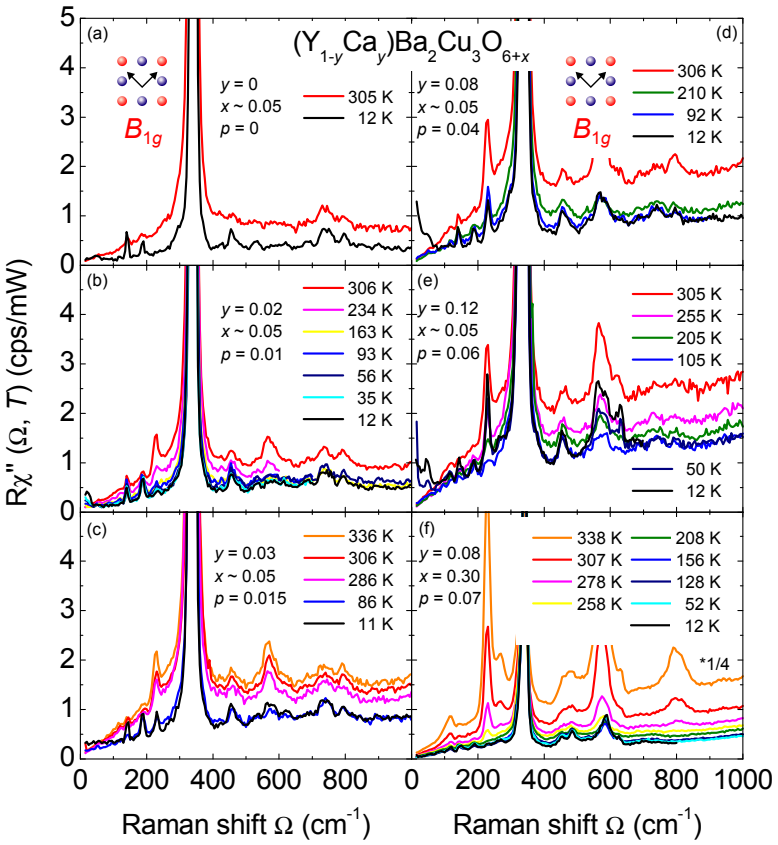

Figure 5.8: *Raman response $\chi''(\Omega, T)$ at various temperatures of differently doped $(Y_{1-y}Ca_y)Ba_2Cu_3O_{6+x}$ samples for B_{1g} symmetry. In panels (a), (b), (c), (d), (e), and (f) results at $p = 0$, 0.01, 0.015, 0.04, 0.06, and 0.07 are shown, respectively.*

($p = 0.06$) measured with a resolution of 5 cm^{-1} is plotted. Here a second peak at approximately 328 cm^{-1} is visible, and it explaines the shoulder of the spectrum at $p = 0.06$ plotted in Fig. 5.9, where the second peak is not resolved. In Fig. 5.10 (b) the B_{1g} phonon of $(Y_{0.92}Ca_{0.08})Ba_2Cu_3O_{6.30}$ ($p = 0.07$) measure with a resolution of 5 cm^{-1} is plotted. At $p = 0.07$ the second peak is not visible, indicating a different origin of the shoulder of the phonon with respect to $p = 0.06$. Finally, in Fig. 5.10 (c) the B_{1g} phonons of $(Y_{0.92}Ca_{0.08})Ba_2Cu_3O_{6.05}$ and $YBa_2Cu_3O_{6.30}$ ($p = 0.04$) are plotted. The data show that at $p = 0.04$ the phonon is almost symmetric independent of the way of doping.

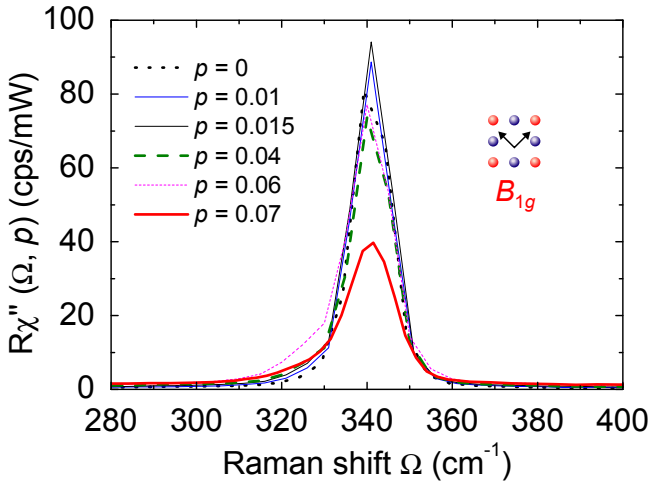

Figure 5.9: *Doping dependence of the B_{1g} phonon of $(Y_{1-y}Ca_y)Ba_2Cu_3O_{6+x}$ at low temperature.*

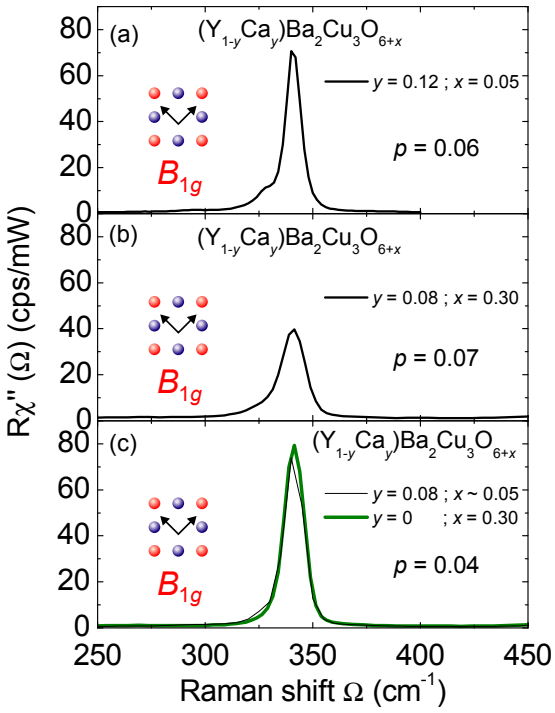

Figure 5.10: *Raman spectra of the B_{1g} phonon of $(Y_{1-y}Ca_y)Ba_2Cu_3O_{6+x}$ at different doping levels as indicated in the figure. The quantities x and y refer to the formula and indicate how the doping is achieved.*

5.2.4 B_{2g} Raman response of $(Y_{1-y}Ca_y)Ba_2Cu_3O_{6+x}$

The temperature dependence of the Raman response $\chi''(\Omega, T)$ of $(Y_{1-y}Ca_y)Ba_2Cu_3O_{6+x}$ at different doping levels is plotted in Fig. 5.11. The

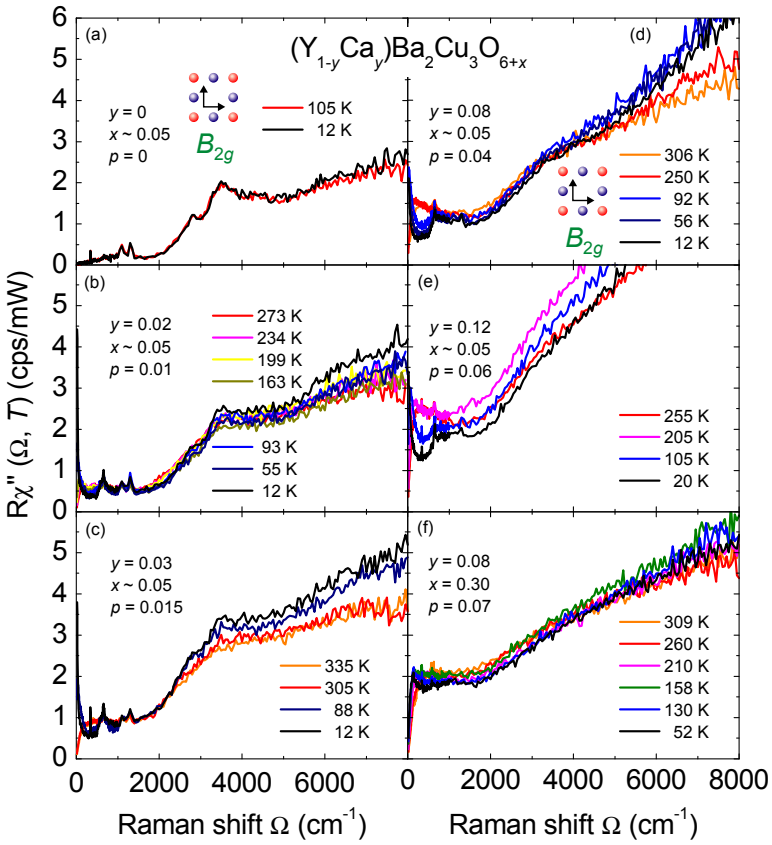

Figure 5.11: *Raman response $\chi''(\Omega, T)$ at various temperatures, as indicated in the figures, of differently doped $(Y_{1-y}Ca_y)Ba_2Cu_3O_{6+x}$ samples for the B_{2g} symmetry. In panels (a), (b), (c), (d), (e), and (f) results at $p = 0$, 0.01, 0.015, 0.04, 0.06, and 0.07 are shown, respectively.*

spectra show a hump at approximately 3700 cm^{-1} corresponding to the second-order two-magnon scattering process.

Upon reducing the temperature a spectral weight depletion becomes visible in a wide energy range, up to at least 3000 cm^{-1}, at $p = 0.04$ and 0.06 (Fig. 5.11 (d) and (e)). Below approximately 650 cm^{-1} a second spectral weight depletion sets in. The low-energy spectral weight depletion is visible

also at $p = 0.01$ and 0.15, and it will be described more in detail below. At $p = 0.07$ there is only one spectral weight depletion visible up to at least 1000 cm^{-1}.

To better visualize the doping dependence of the B_{2g} spectra the Raman response at low temperature for the various doping levels studied is plotted in Fig. 5.12. The overall intensity increases with doping in the range $0 < p <$

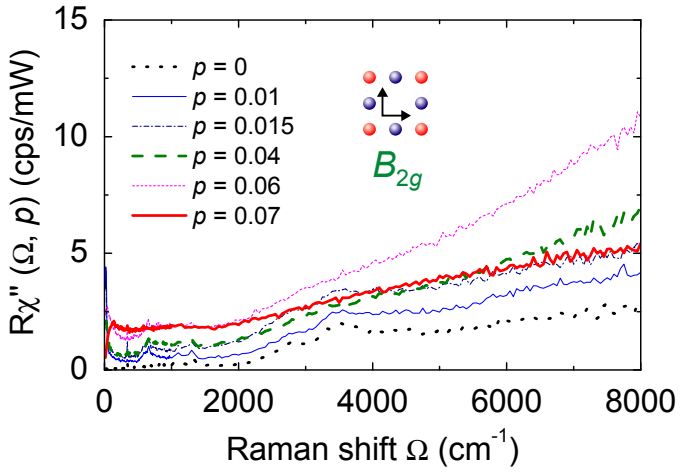

Figure 5.12: *Raman response $\chi''(\Omega, p)$ of differently doped $(Y_{1-y}Ca_y)Ba_2Cu_3O_{6+x}$ single crystals in the normal state at low temperature for the B_{2g}.*

0.06. At $p = 0.07$ the signal does not increases anymore with doping, the spectrum assume a more convex shape and is depressed at high energy. The hump around 3700 cm^{-1} practically vanishes at $p = 0.07$.

A zoom-in on the low-energy Raman response $\chi''(\Omega, T)$ for B_{2g} symmetry is plotted in Fig. 5.13. In the undoped antiferromagnet (Fig. 5.13 (a)) the Raman response is extremely weak. The spectra approach linearly zero. The Raman signal, as well as the initial slope of the spectra, decrease on lowering the temperature. A weak feature around 650 cm^{-1} is superimposed to the electronic continuum. The peak at approximately 340 cm^{-1} is a leakage of the strong B_{1g} phonon due to a small misalignment of the sample. At finite doping additional features appear.

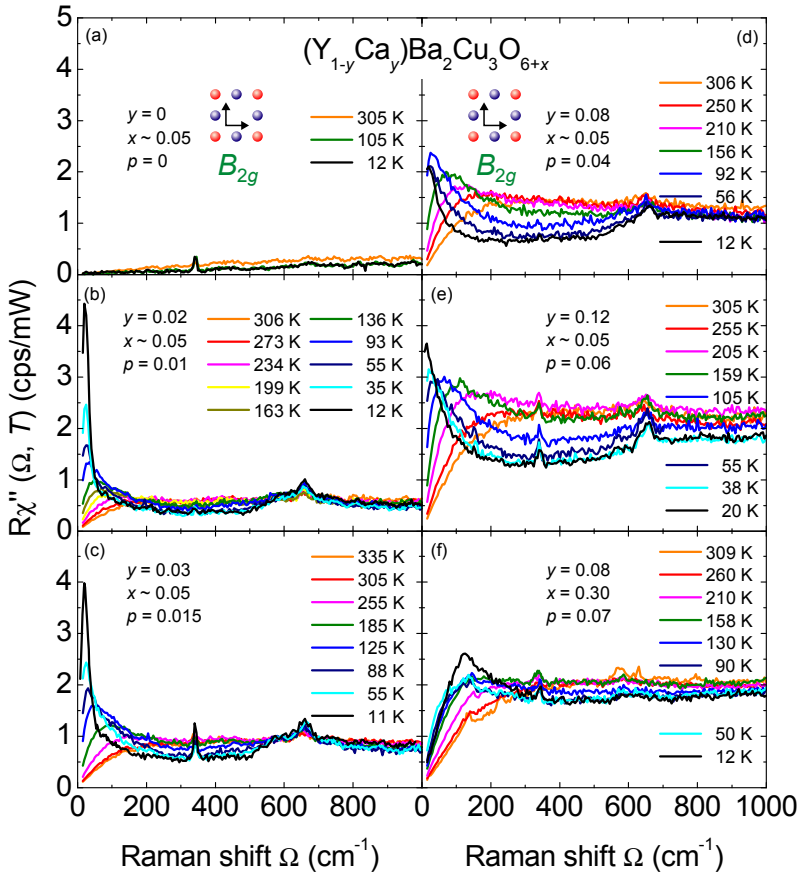

Figure 5.13: *Raman response $\chi''(\Omega, T)$ at various temperatures, as indicated in the figures, of differently doped $(Y_{1-y}Ca_y)Ba_2Cu_3O_{6+x}$ samples for the B_{2g} symmetry. In panels (a), (b), (c), (d), (e), and (f) results at $p = 0$, 0.01, 0.015, 0.04, 0.06, and 0.07 are shown, respectively.*

One of the main characteristics of the spectra in the doping range $0.01 \leq p \leq 0.06$ (Fig. 5.13 (b-e)) is a strong peak below $\Omega \approx 50$ cm^{-1} emerging at low temperature. Independent of the doping levels the peak position shifts towards to lower energies upon cooling.

The dependence on excitation energy of the quasi-elastic peak was also investigated. Spectra of $(Y_{0.98}Ca_{0.02})Ba_2Cu_3O_{6.05}$ ($p = 0.01$) and $(Y_{0.92}Ca_{0.08})Ba_2Cu_3O_{6.05}$ ($p = 0.04$) measured with the 458 and 514.5 nm laser lines are plotted in Fig. 5.14. The quasi-elastic peak becomes weaker upon reducing the excitation energy.

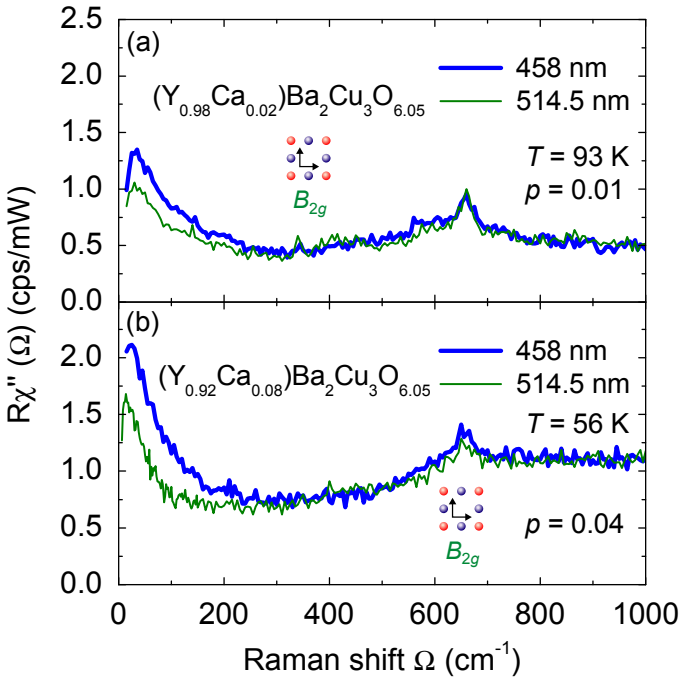

Figure 5.14: *Raman response* $\chi''(\Omega, T)$ *of* $(Y_{0.98}Ca_{0.02})Ba_2Cu_3O_{6.05}$ *(a) and* $(Y_{0.92}Ca_{0.08})Ba_2Cu_3O_{6.05}$ *(b) measured with the 458 and 514.5 nm laser lines, as indicated in the figure.*

Another important feature in the range $0.01 < p < 0.06$ is a depression of the spectral weight below approximately 650 cm^{-1} upon cooling. At $p = 0.01$ the spectra at different temperatures show practically the same intensity above approximately 650 cm^{-1}. Below this energy a clear depression of the spectral weight is visible, and the same holds for $p = 0.04$. The energy range of the depression increases with doping. At $p = 0.06$ the spectral weight depression starts around 700 cm^{-1}. The magnitude of the depression increases monotonically with doping.

At $p = 0.07$ the Raman response changes qualitatively. First of all the spectra do not show the peak at low energy. In addition the spectral weight depletion changes. It shows a larger energy range, up to at least 1000 cm^{-1}, and here the trend of the magnitude of the spectral weight depletion is reversed and it is smaller than at $p = 0.06$.

5.3 Superconductivity

In this section Raman data of underdoped cuprates in the superconductive state are shown. Measurements in the superconducting phase were performed also in the deeply underdoped regime close to the onset point of superconductivity where information is missing.

Spectra of $La_{1.88}Sr_{0.12}CuO_4$ in the normal and superconducting state are plotted in Fig. 5.15. The B_{1g} Raman response (Fig. 5.15 (a)) does not change upon entering the superconducting state. The increase of spectral weight visible at low energy is determined by the peak at low energy described in Sect. 5.1.2. In B_{2g} spectra a superconducting-induced peak pops up below the transition temperature T_c, and spectral weight is transferred from low energy into the peak. The Raman response in the superconducting state extrapolates to zero in the limit $\Omega \rightarrow 0$.

The spectra of $(Y_{0.92}Ca_{0.08})Ba_2Cu_3O_{6.30}$, plotted in Fig. 5.16, show the same qualitative behaviour of those of $La_{1.88}Sr_{0.12}CuO_4$. The B_{1g} spectra do not change upon entering into the superconducting state, while in B_{2g} symmetry the data show that also very close to the onset point of superconductivity a peak at approximately 125 cm^{-1} pops up below T_c. Similar to $La_{1.88}Sr_{0.12}CuO_4$ the Raman response extrapolate to zero in the limit $\Omega \rightarrow 0$.

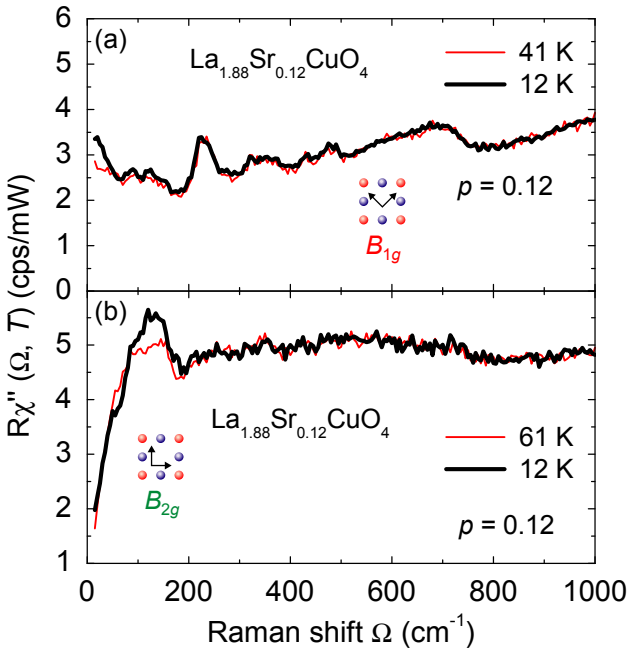

Figure 5.15: *Raman response $\chi''(\Omega, T)$ of $La_{1.88}Sr_{0.12}CuO_4$ ($p = 0.12$) in the normal and superconducting state for, B_{1g} (a) and B_{2g} (b) symmetry.*

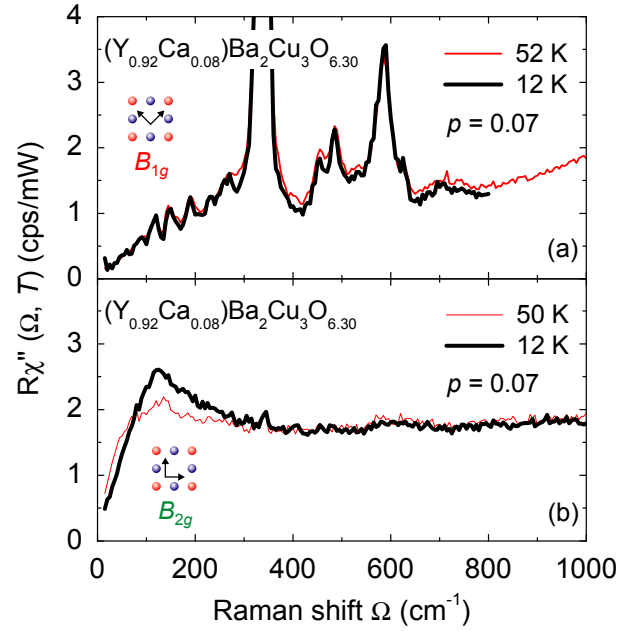

Figure 5.16: *Raman response $\chi''(\Omega, T)$ of $(Y_{0.92}Ca_{0.08})Ba_2Cu_3O_{6.30}$ ($p = 0.07$) in the normal and superconducting state, for B_{1g} (a) and B_{2g} (b) symmetry.*

Chapter 6

Discussion

In this chapter the Raman measurements performed in this thesis and presented in the previous chapter are discussed and interpreted based on various model considerations developed so far. It is found that charge and spin ordering is a universal feature of the cuprates. The relation between charge and spin ordering, and superconductivity is discussed, and a connection between the symmetry of the ordering and the superconducting critical temperature T_c is found. The quantum critical point scenario is considered taking into account the new pieces of information obtained in this work. Furthermore, the pseudogap phenomenon and its relation with charge and spin ordering is discussed. Finally, data obtained in the superconducting phase close to the onset point of superconductivity are analyzed and compared with previous results at higher doping levels.

6.1 Raman scattering and transport in cuprates: $0.05 < p < 0.26$

In this section a brief summary of the previous Raman scattering results of cuprate superconductors ($p > p_{\rm sc1}$) is given. The evolution of the Raman scattering spectra from the overdoped regime down to the underdoped regime (above the onset point of superconductivity $p_{\rm sc1}$) is discussed, and the

information obtained from the Raman data is compared to that obtained by transport measurements. The various features observed in the Raman spectra, such as the (different) evolution of the B_{1g} and B_{2g} spectra with doping and temperature established in previous works, together with the new information obtained from the data measured in this thesis above p_{sc1}, are discussed. These pieces of information are necessary to properly interpret the new data measured here.

6.1.1 B_{2g} symmetry

In order to quantify the dynamics of the carriers and to study its evolution with temperature, the Raman relaxation rates $\Gamma(\Omega, T)$ are extracted from the response $\chi''(\Omega, T)$. The static relaxation rates (*dc* limit) $\Gamma_0(T) \equiv \Gamma(\Omega \to 0, T)$ are related to the initial slope of the spectra and represent the inverse of the quasiparticle lifetime. Therefore, they have similar relevance as the resistivity data obtained from transport experiments ([122] and Sect. 3.6). The method to calculate $\Gamma(\Omega, T)$ is described in Sect. 3.7.

In Fig. 6.1 the temperature dependence of the static Raman relaxation rates of differently doped $Bi_2Sr_2CaCu_2O_{8+\delta}$ single crystals (reproduced from Ref. [122]) are plotted together with resistivities derived by applying a Drude model (Eq. (3.42)). The B_{2g} rates agree with the resistivities at all doping levels with discrepancies smaller than 30%.

The temperature dependence of the Raman rates of $(Y_{1-y}Ca_y)Ba_2Cu_3O_{6+x}$ and its evolution with doping is plotted in Fig. 6.2, together with the derived resistivities. The static rates at $p = 0.10$, 0.16, and 0.19 are reproduced from Ref. [122]. Similarly to $Bi_2Sr_2CaCu_2O_{8+\delta}$ the Raman rates of $(Y_{1-y}Ca_y)Ba_2Cu_3O_{6+x}$ agree with the resistivity, with discrepancies less than 30%. The new data measured at $p = 0.07$ confirm the results previously obtained at higher doping levels, showing the agreement between Raman rates and resistivity also close to the onset point of superconductivity.

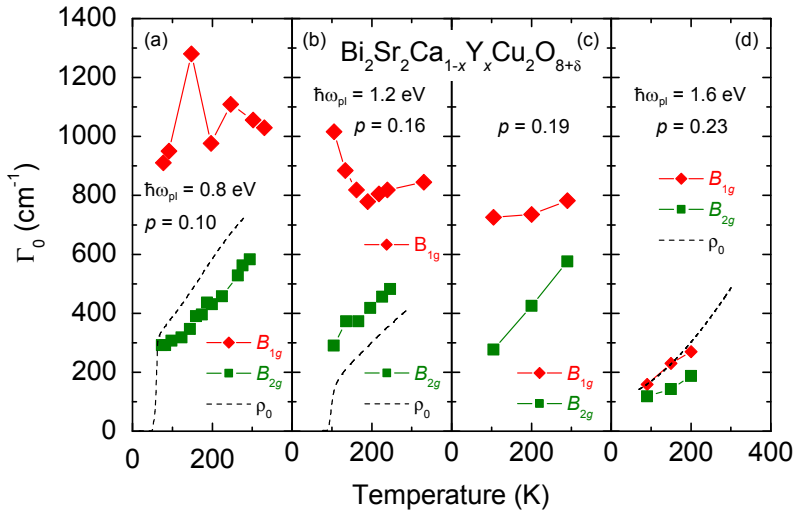

Figure 6.1: *Temperature dependence of the static relaxation rates $\Gamma_0(T)$ for $Bi_2Sr_2CaCu_2O_{8+\delta}$ at different doping levels as indicated in the figure. The dashed lines in (a), (b), and (d) are relaxation rates calculated from the resistivity through Eq. (3.42). $\rho(T)$ and the plasma frequencies are taken from Ref. [138]. The figure is reproduced from Ref. [122].*

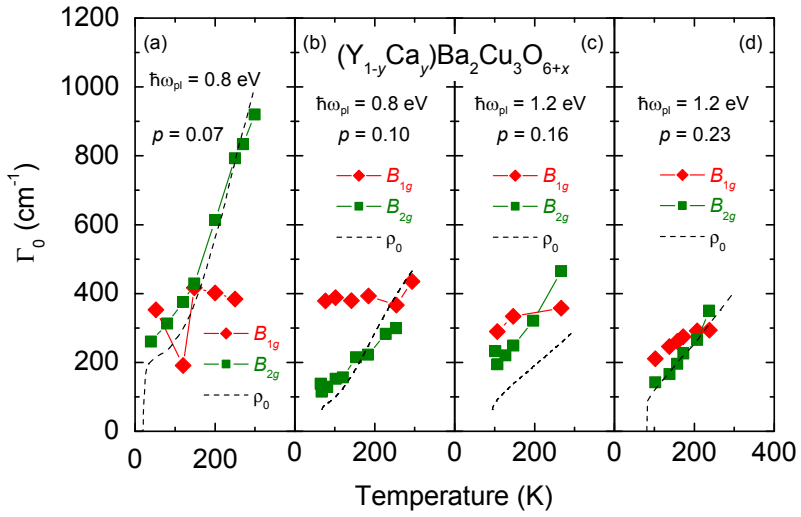

Figure 6.2: *Temperature dependence of the static relaxation rates $\Gamma_0(T)$ for $(Y_{1-y}Ca_y)Ba_2Cu_3O_{6+x}$ at different doping levels as indicated in the figure. The data at $p = 0.10$, 0.16, and 0.19 are taken from Ref. [122]. The dashed lines are relaxation rates calculated from the resistivity of sample at comparable doping levels, taken from Ref. [96] ((b)-(d)) and Ref. [68] (a), through Eq. (3.42). The plasma frequencies are taken from Ref. [139].*

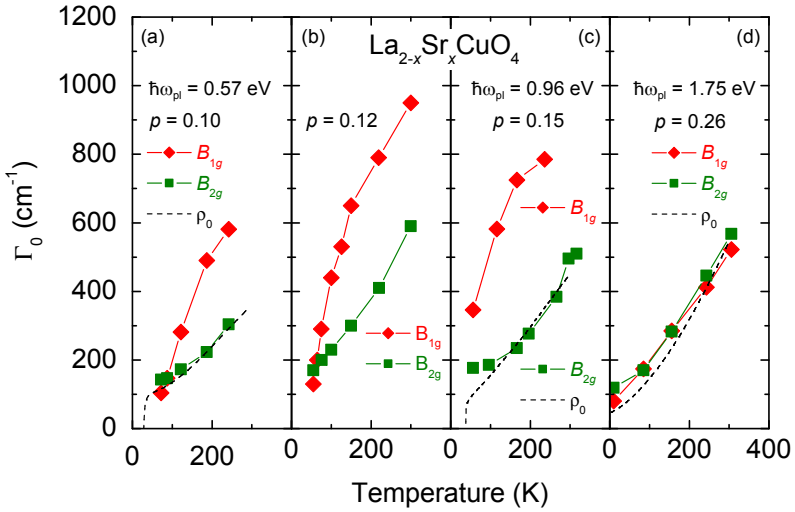

Figure 6.3: *Temperature dependence of the static relaxation rates* $\Gamma_0(T)$ *for* $La_{2-x}Sr_xCuO_4$ *at different doping levels as indicated in the figure. The dashed lines are relaxation rates calculated from the resistivity through Eq. (3.42). The plasma frequencies have been used to scale the transport rates to those measured with the Raman scattering. The data at* $p = 0.10$*, 0.15, and 0.26 are taken from Ref. [135].*

Finally, the temperature dependence of the static rates of differently doped $La_{2-x}Sr_xCuO_4$ samples, reproduced from Ref. [135] are plotted in Fig. 6.3. Again the B_{2g} static rates agree with the resistivities.

In summary, apart from the different cuprate families and doping levels, all measurement performed so far show agreement between the B_{2g} static Raman rates and the resistivity.

6.1.2 B_{1g} symmetry

In the overdoped regime the B_{1g} and the B_{2g} rates of $Bi_2Sr_2CaCu_2O_{8+\delta}$ (Fig. 6.1 (d)) show almost the same values and the same temperature dependences. Upon reducing the doping the B_{1g} rates of $Bi_2Sr_2CaCu_2O_{8+\delta}$ become almost temperature independent or show insulating behaviour, and have always higher values with respect to the B_{2g} rates.

At the highest doping level the B_{1g} and B_{2g} static rates of $(Y_{1-y}Ca_y)Ba_2Cu_3O_{6+x}$ (Fig. 6.2 (d)) show different values. The differences are

small and both rates decrease upon cooling. Upon reducing the doping level the discrepancy between the B_{1g} and the B_{2g} rates increases, with the B_{1g} rates becoming almost temperature independent. In $(Y_{1-y}Ca_y)Ba_2Cu_3O_{6+x}$ the anisotropy of the rates pertains only to the temperature dependence, and in contrast to $Bi_2Sr_2CaCu_2O_{8+\delta}$ the B_{1g} rates do not have systematically bigger values than the B_{2g} rates.

In strongly overdoped $La_{2-x}Sr_xCuO_4$ (Fig. 6.3 (d)) the static rates for B_{1g} and B_{2g} symmetry practically coincide at all temperatures. At lower doping levels the B_{1g} and B_{2g} rates assume substantially different values at high temperature, with the B_{1g} rates bigger than those at the B_{2g} symmetry. Upon reducing the temperature the B_{1g} rates decrease instead of becoming almost temperature independent as in $Bi_2Sr_2CaCu_2O_{8+\delta}$ and $(Y_{1-y}Ca_y)Ba_2Cu_3O_{6+x}$.

While the temperature and doping dependences of the static rates in B_{2g} symmetry show a coherent picture for all cuprate families studied up to now, for B_{1g} symmetry it is less clear and at first glance the evolution with doping and temperature of the B_{1g} rates in different compounds seems to be unrelated. However, to a more accurate observation of the data common scenarios are found.

The B_{1g} rates of $Bi_2Sr_2CaCu_2O_{8+\delta}$ undergo a metal-insulator transition upon reducing the doping levels at the critical doping $p \approx 0.21$ [140]. The data of $(Y_{1-y}Ca_y)Ba_2Cu_3O_{6+x}$ show, similarly to $Bi_2Sr_2CaCu_2O_{8+\delta}$ almost temperature independent B_{1g} rates. Moreover, the descrepancies between the two rates become continuously smaller upon increasing the doping. Opposite to $Bi_2Sr_2CaCu_2O_{8+\delta}$, here the two rates show different values also at the highest doping level, and even if both rates decrease upon cooling the slopes are different. However, the highest doping of $(Y_{1-y}Ca_y)Ba_2Cu_3O_{6+x}$ is only 0.19, and at this doping level also the B_{1g} and B_{2g} rates of $Bi_2Sr_2CaCu_2O_{8+\delta}$ show different values and slopes. The temperature and doping dependences of the B_{1g} rates of $Bi_2Sr_2CaCu_2O_{8+\delta}$ and $(Y_{1-y}Ca_y)Ba_2Cu_3O_{6+x}$ can be well understood in the metal-insulator framework with the critical doping higher than 0.19 for $(Y_{1-y}Ca_y)Ba_2Cu_3O_{6+x}$ (as it is for $Bi_2Sr_2CaCu_2O_{8+\delta}$). While a

common scenario emerges for $Bi_2Sr_2CaCu_2O_{8+\delta}$ and $(Y_{1-y}Ca_y)Ba_2Cu_3O_{6+x}$, the data of $La_{2-x}Sr_xCuO_4$ do not seem to fit in the metal-insulator scenario. However, B_{1g} and B_{2g} rates at the highest doping level show practically the same values, and if only the high temperature B_{1g} rates are taken into consideration, upon reducing the doping levels different values of the two rates similar to $Bi_2Sr_2CaCu_2O_{8+\delta}$, with the B_{1g} rates greater than the B_{2g} rates, are observed. This behaviour suggests that the metal-insulator transition is a general feature of all cuprates, and that in $La_{2-x}Sr_xCuO_4$ it occurs along with an additional phenomenon. Both determine the evolution with doping and temperature of the B_{1g} static rates.

In Fig. 6.4 the spectra of $Bi_2Sr_2CaCu_2O_{8+\delta}$, $(Y_{1-y}Ca_y)Ba_2Cu_3O_{6+x}$, and $La_{2-x}Sr_xCuO_4$ at the same doping level $p = 0.10$ are plotted. The spectra of $La_{2-x}Sr_xCuO_4$ are different from those of $Bi_2Sr_2CaCu_2O_{8+\delta}$ and $(Y_{1-y}Ca_y)Ba_2Cu_3O_{6+x}$. The quasi-elastic peak emerging at low temperature determines the initial slope of the Raman response and therefore the static rates. The anomalous B_{1g} rates of $La_{2-x}Sr_xCuO_4$ demonstrate that the low energy peak is an additional response on top of the ordinary quasiparticle response.

6.2 New features in $La_{2-x}Sr_xCuO_4$ and $(Y_{1-y}Ca_y)Ba_2Cu_3O_{6+x}$

In this section the Raman response across the onset point of superconductivity, $p_{sc1} \approx 0.05$ is discussed. Evidence of an additional response coming from charge and spin ordering is found.

6.2.1 $La_{2-x}Sr_xCuO_4$ below and above p_{sc1}

In order to try to understand the additional response observed in the B_{1g} spectra of $La_{1.90}Sr_{0.10}CuO_4$ (see Sect. 6.1.2) measurements of $La_{2-x}Sr_xCuO_4$ single crystals at lower and higher doping levels have been performed. In

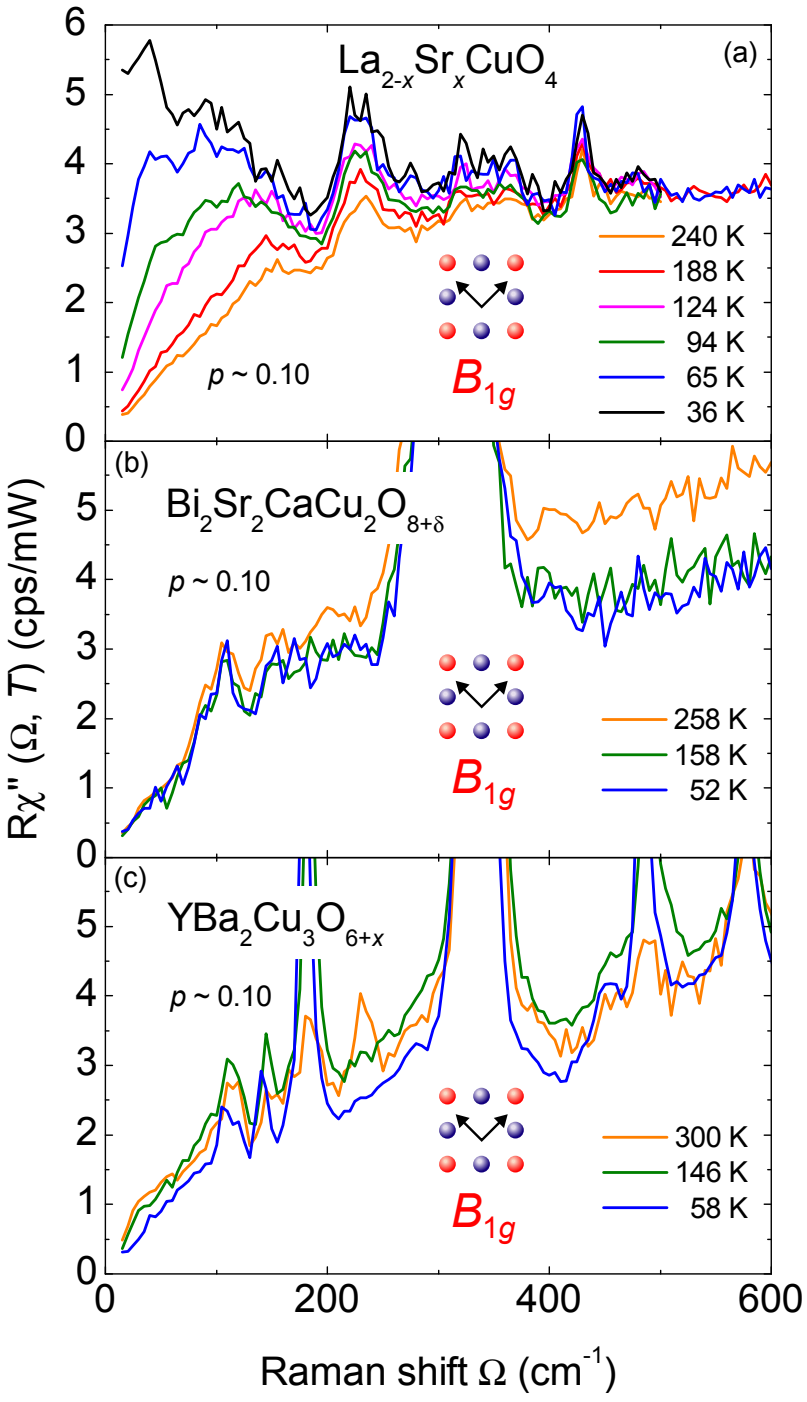

Figure 6.4: *Temperature dependence of the Raman response of $La_{2-x}Sr_xCuO_4$ (a), $Bi_2Sr_2CaCu_2O_{8+\delta}$, and $YBa_2Cu_3O_{6+x}$ at similar doping levels, as indicated in the figure. The data are taken from Ref. [141]*

Fig. 6.5 the relaxation rates measured for $La_{1.98}Sr_{0.02}CuO_4$ ($p = 0.02$) together with the static rates at higher doping levels are plotted as function of temperature.

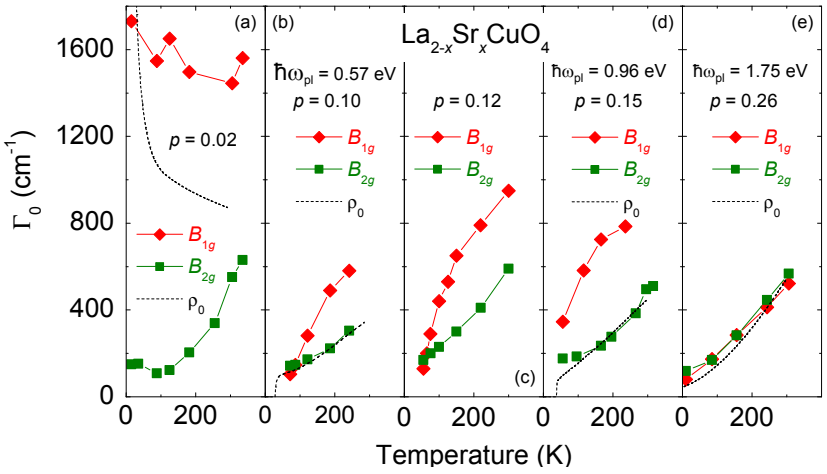

Figure 6.5: *Temperature dependence of the static relaxation rates $\Gamma_0(T)$ for $La_{2-x}Sr_xCuO_4$ at the doping levels indicated in the figure for B_{1g} and B_{2g} symmetries. The dashed lines are relaxation rates calculated from the resistivity through Eq. (3.42). The plasma frequencies were used to scale the transport rates to those measured with the Raman scattering ((b), (d), and (e)). The data at $p = 0.10$, 0.15, and 0.26 are taken from Ref. [135].*

At $p = 0.02$, the B_{1g} static rates are almost temperature independent, and much higher than the B_{2g} rates. The B_{1g} rates of $La_{1.98}Sr_{0.02}CuO_4$ ($p = 0.02$) are qualitatively different from those at $p = 0.10$ and 0.12, since they do not show the "anomalous" decrease upon cooling. This difference arises from the low energy peak, that is absent at $p = 0.02$, as one can see comparing the spectra of Fig. 5.1 (a) with those plotted in Figs. 5.1 (b) and 5.2 (a). On the other hand, the B_{1g} static rates at $p = 0.02$ show qualitatively the same temperature dependence as the static rates of $Bi_2Sr_2CaCu_2O_{8+\delta}$ and $(Y_{1-y}Ca_y)Ba_2Cu_3O_{6+x}$, corroborating the hypothesis that the metal-insulator transition occurs also in $La_{2-x}Sr_xCuO_4$ and the B_{1g} rates at $p = 0.10$, 0.12, and 0.15 are determined by a superposition of the metal-insulator transition and an additional feature, i.e. the peak at low energy.

The B_{2g} rates of $La_{1.98}Sr_{0.02}CuO_4$ decrease monotonically upon cooling, in spite of the fact that the resistivity $\rho(T)$ shows a crossover from $\partial\rho/\partial T > 0$ to $\partial\rho/\partial T < 0$. For the first time, the two quantities do not agree. The discrepancy arises from a low energy peak visible in the B_{2g} spectra of $La_{1.98}Sr_{0.02}CuO_4$ (see Fig. 5.1 (c)), and it demonstrates, similarly to $La_{1.90}Sr_{0.10}CuO_4$ for B_{1g} symmetry, that at low energy there is an additional response beyond the ordinary quasiparticle response.

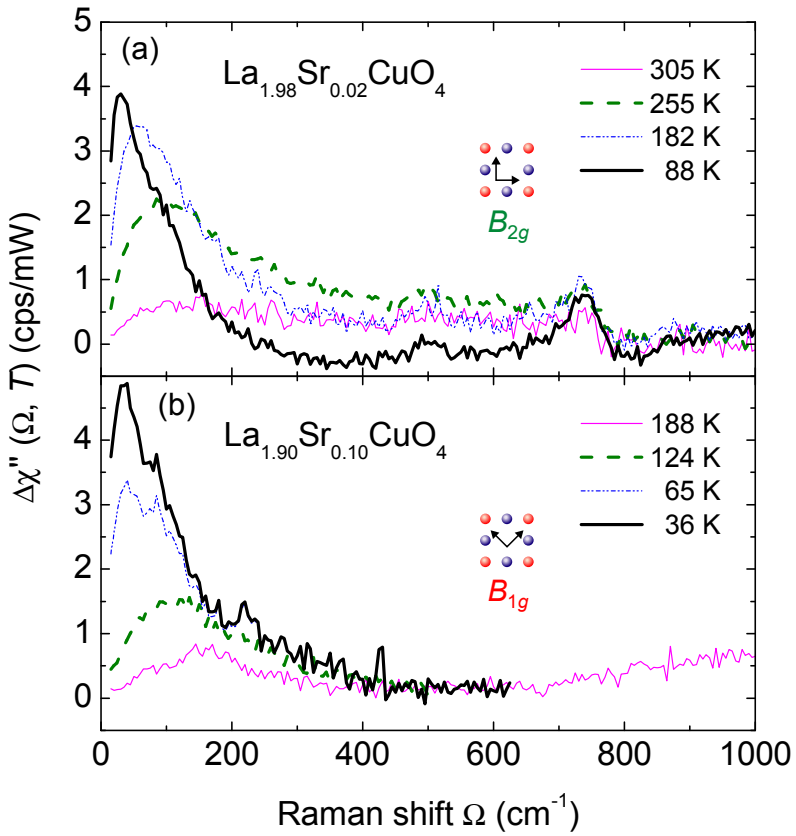

Figure 6.6: *Low-energy Raman response $\Delta\chi''(\Omega, T)$ of $La_{2-x}Sr_xCuO_4$ after the subtraction of the electronic background. In panels (a) and (b) B_{1g} at $p = 0.10$ and B_{2g} at $p = 0.02$ symmetry results are shown, respectively.*

To better visualize the new response the contribution of the electronic continuum was subtracted from the experimental data. Since not only the peak but also the continuum depend on temperature, only an approximate procedures is possible. Here, the continuum at the highest temperature was

subtracted from all spectra measured at low temperature. In this way temperature effects extrinsic to the low energy response are small. The spectra after the subtraction of the particle-hole continuum are shown in Fig. 6.6. Apart from different doping levels and symmetries the additional responses have remarkably similar spectral shapes and show the same temperature dependence, with the additional peaks softening upon cooling. These observations suggest a common underlying mechanism for the additional excitations.

The physical mechanism responsible for the additional response is not yet fully understood. The additional peaks change from B_{2g} to B_{1g} symmetry upon varying the doping level from $p = 0.02$ to 0.10. B_{1g} symmetry measures the difference $xx - yy$ (on a microscopic scale) projecting out a possible orthorhombic distortion. Fully oxygenated $YBa_2Cu_3O_7$ has $Cu - O$ chains along the crystallographic b axis making $b > a$ is a familiar example. Even if the sample is twinned, the chain contributions are always superimposed on the B_{1g} spectra, while the xx and yy spectra are equal (as opposed to a single-domain crystal). The same argumentation holds for B_{2g} symmetry with the axes rotated by 45°.

In order to try to determine the origin of low-energy Raman response information from other experimental methods are needed. In the next section a summary of neutron scattering results, which show evidence of spin and charge ordering, is presented.

6.2.2 Neutron scattering in underdoped La-based cuprates

Neutron scattering was intensively used to investigate the magnetic excitation spectrum of several families of cuprates, and many measurements were performed on La-based crystals. Measurements performed on $La_{1.6-x}Nd_{0.4}Sr_xCuO_4$ show evidence of a static modulation of spin and charge, in which antiferromagnetic domains of copper spins are separated by periodically spaced domain walls into which the holes segregate [17] (see Fig. 2.8).

Measurements of $La_{2-x}Sr_xCuO_4$ show magnetic peaks such as those plot-

ted in Fig. 6.7 (reproduced from Ref. [142]) [74, 75, 142] indicating a magnetic superstructure similar to that observed in $La_{1.6-x}Nd_{0.4}Sr_xCuO_4$. The magnetic order in $La_{2-x}Sr_xCuO_4$ becomes dynamic at $p \gtrsim 0.06$ [22, 23, 24, 143]. The antiferromagnetic domains rotate by 45° at $p \approx 0.055$, being oriented along the diagonal of the CuO_2 planes (and will be referred to as diagonal) at $p \leq 0.055$ and along the $Cu-O$ bond direction (referred to as parallel) at $p \geq 0.055$ [142] (Fig. 6.8).

The antiferromagnetic order, as well as the charge stripes, break the symmetry of the crystal introducing an orthorhombic distortion of the structure, and their rotation represent a change of symmetry similar to the change of symmetry of the additional response measured with Raman scattering. This observation suggests a relation between the two phenomena, and indicates charge and spin ordering as a possible origin of the low-energy peaks observed in the Raman response.

6.2.3 Dynamical stripes

In contrast to $La_{1.6-x}Nd_{0.4}Sr_xCuO_4$ with $x = 0.12$, $La_{1.875}Ba_{0.125}CuO_4$ and $La_{1.875}Ba_{0.075}Sr_{0.050}CuO_4$ where together with the static magnetic superstructures static charge ordering was also found [17, 21, 19, 73], in $La_{2-x}Sr_xCuO_4$ only magnetic ordering has been observed. At present it is an open issue whether (eventually dynamic) stripes are a general feature of cuprates or whether they are a peculiar characteristic of few specific compounds [144, 145]. In particular it is intensively debated whether there are dynamical stripes in $La_{2-x}Sr_xCuO_4$ with the same preferential orientation of the antiferromagnetic domains.

Stripes have been detected mainly with neutron scattering as the indirect effect of a periodic dislocation of ions [17]. While with neutron scattering a static distribution of charge can be detected, the dynamical ordering of conducting electrons is much harder to pin down, since the ions practically do not follow the dynamical ordering of the electrons, and the effect is likely too weak to be measured. On the other hand, photons couple directly to the

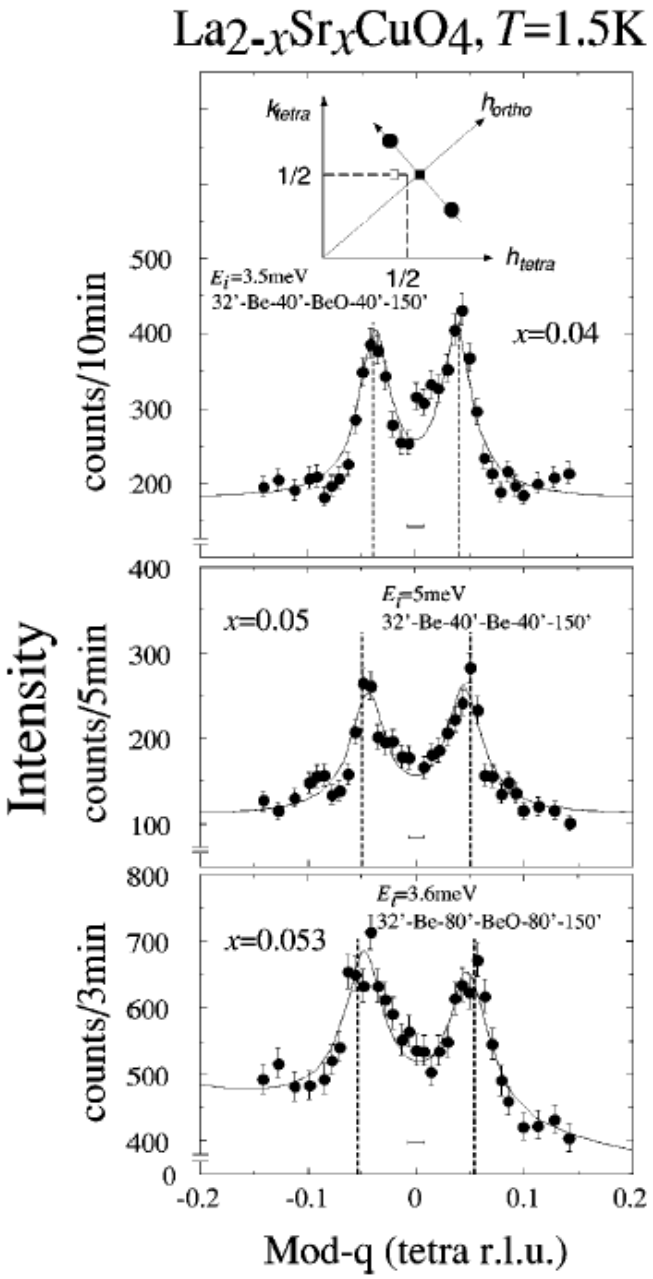

Figure 6.7: *Elastic peak profile at 1.5 K for a scan along the Brillouin zone diagonal of differently doped samples as indicated in the figure, reproduced from Ref. [142].*

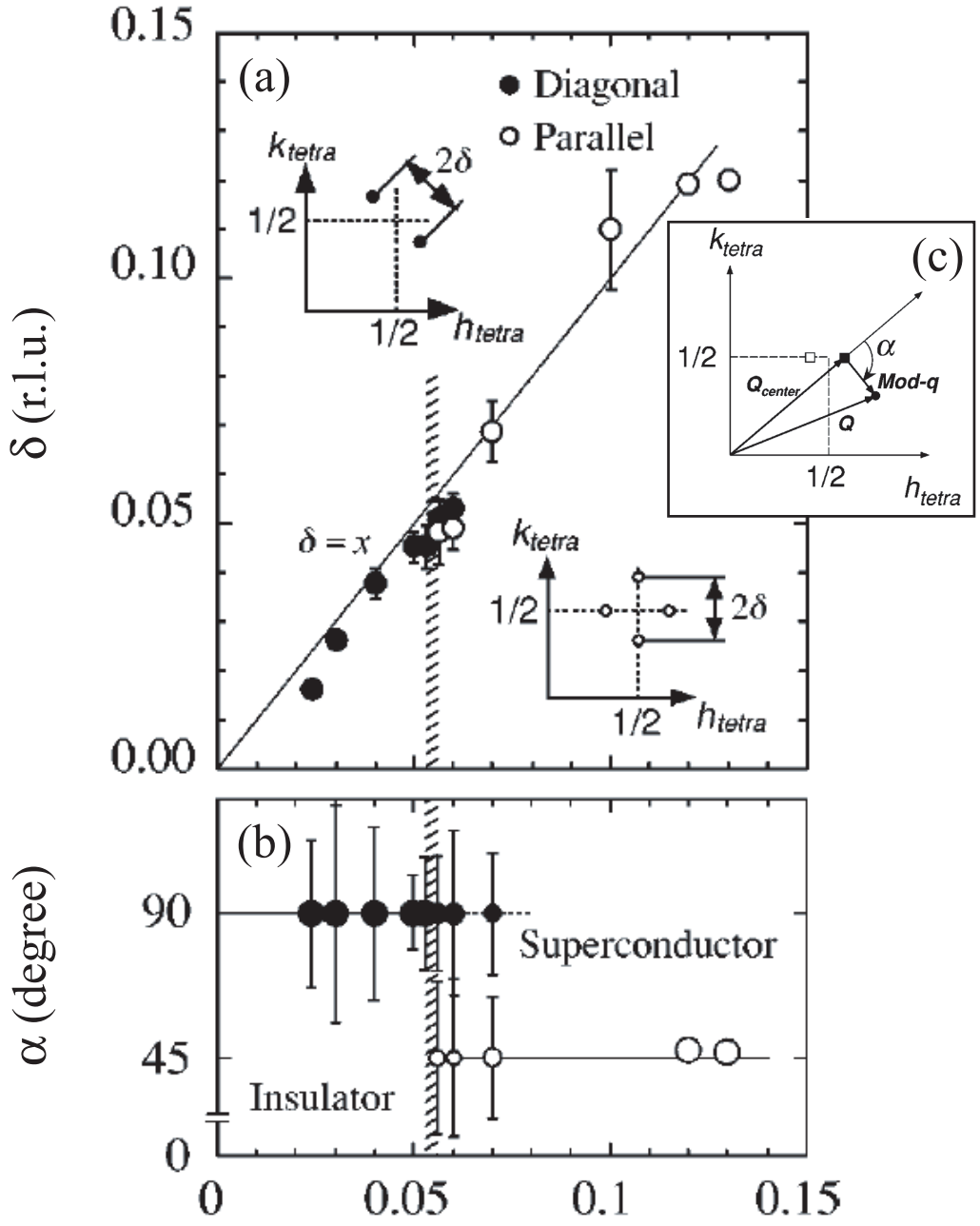

Figure 6.8: *(a) Sr concentration dependence of the incommensurability δ and (b) angle α describing the orientation of the neutron peaks. α is defined in inset (c) where solid and open squares represent the orthorhombic (1,0,0) and (0,1,0) positions from the two domains. The figures and the data are taken from Ref. [142].*

charge, and Raman scattering measures the response of charge fluctuations. Therefore inelastic (Raman) light scattering can be a powerful tool to investigate dynamical charge ordering, and the response of dynamical stripes can in principle be measured.

6.2.3.1 $\mathbf{La_{2-x}Sr_xCuO_4}$

The Raman data measured in $La_{2-x}Sr_xCuO_4$ show evidence of additional excitations in B_{2g} symmetry at $p = 0.02$ and in B_{1g} symmetry at $p = 0.10$ (see Sect. 6.2.1). As mentioned in Sect. 6.2.1 in B_{1g} symmetry the $xx - yy$ response is measured, and therefore the response of an orthorhombic distortion introduced by stripes with preferential direction along the principal axes is detected, while in B_{2g} symmetry the xy response is measured. Hence, the signal of stripes directed along the diagonal of the CuO_2 planes can be detected. Therefore, the additional peaks measured in the Raman spectra of $La_{2-x}Sr_xCuO_4$ at $p = 0.02$, 0.10, and 0.12 agree with the response of fluctuating stripes with the same preferential direction of the antiferromagnetic domains, since the additional peaks are detected in B_{2g} symmetry, at $p = 0.02$ and in B_{1g} symmetry at $p = 0.10$ and 0.12. Moreover, the energy of the additional response decreases upon cooling, indicating that the excitations are not the response of an ordered phase. The response of the ordering of the spins along an easy axis for instance, is expected to harden upon cooling.

For the symmetry argument and the temperature dependence, it is natural to conclude that in $La_{2-x}Sr_xCuO_4$ there are diagonal dynamical stripes below the onset point of superconductivity and parallel ones above that critical doping. Apparently stripes are a common feature of all La-based cuprates, and Nd, Ba, and Eu help to stabilize the stripe phase at low temperature while in $La_{2-x}Sr_xCuO_4$ the charge ordering remains dynamic [146].

6.2.3.2 $\mathbf{(Y_{1-y}Ca_y)Ba_2Cu_3O_{6+x}}$

The B_{2g} spectra of $(Y_{1-y}Ca_y)Ba_2Cu_3O_{6+x}$ plotted in Fig. 5.13, show a strong peak at very low energy in the range $0.01 \leq p \leq 0.06$. The intensities of

the peaks in $(Y_{1-y}Ca_y)Ba_2Cu_3O_{6+x}$ are higher than those in $La_{2-x}Sr_xCuO_4$. Here, the spectra look very much as if an additional peak was superimposed on the electronic continuum, similar to $La_{1.98}Sr_{0.02}CuO_4$. To better quantify this point the resistivity can be compared with the static Raman relaxation rates. In Fig. 6.9 the temperature dependences of the static relaxation rates at the two characteristic doping levels $p = 0.04$, where the low-energy peak is strong, and $p = 0.07$, where the low-energy peak is not visible, are plotted together with resistivities converted with a Drude model (Eq. (3.42)). At $p = 0.07$ the static rates and the resistivity agree, while at $p = 0.04$ the resistivity and the static rates show different temperature dependences; the resistivity increases below approximately 100 K, while the static rates decrease monotonically. The discrepancy between the Raman rates and the

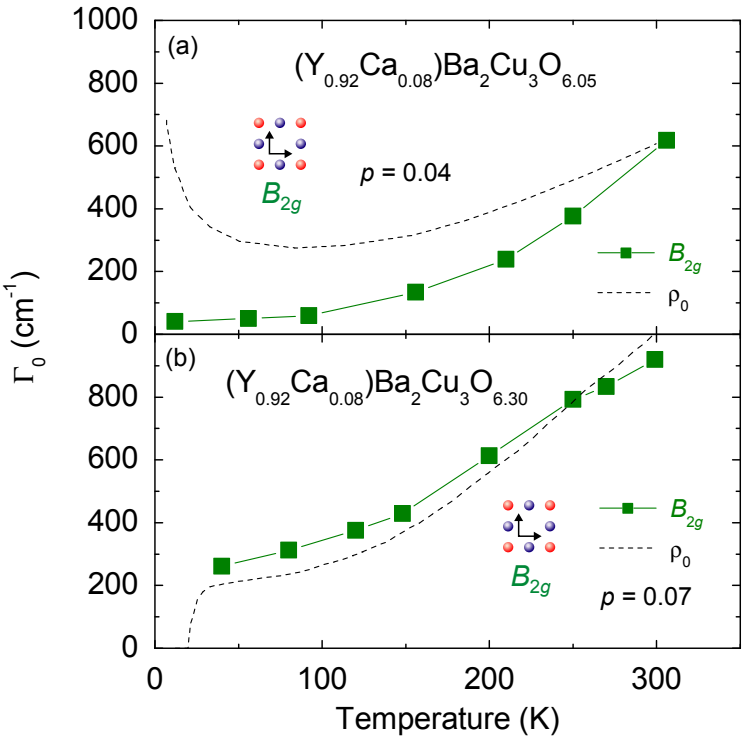

Figure 6.9: *Temperature dependence of the static relaxation rates* $\Gamma_0(T)$ *for* $(Y_{0.92}Ca_{0.08})Ba_2Cu_3O_{6.05}$ *(*$p = 0.04$*) (a) and* $(Y_{0.92}Ca_{0.08})Ba_2Cu_3O_{6.30}$ *(*$p = 0.07$*) (b). The dashed lines are relaxation rates calculated from the resistivity of samples at compareble doping levels, taken from Ref. [68].*

resistivity originates from the peak at low energy, that determines the initial slope of the Raman response, and therefore determines the static rates (see Sect. 3.6 and 3.7). Similar to $La_{2-x}Sr_xCuO_4$ the different temperature dependences of the static rates and the resistivity demonstrate that the low-energy peak of $(Y_{1-y}Ca_y)Ba_2Cu_3O_{6+x}$ is an additional response, and cannot be explained in terms of ordinary electron-hole excitations (see also the dicussion of Sect. 6.1.1).

The contribution of the electronic continuum can be subtracted from the experimental data applying the same procedure as described for $La_{2-x}Sr_xCuO_4$ in Sect. 6.2.1. The result of the background subtraction is shown in Fig. 6.10. Independent of the doping level, the additional peak increases in intensity and moves towards lower energy upon reducing the temperature. After the subtraction of the electronic background the additional response of $(Y_{1-y}Ca_y)Ba_2Cu_3O_{6+x}$ shows a very similar spectral shape and temperature dependence of that of $La_{2-x}Sr_xCuO_4$. Therefore, the conclusion is that the additional peak of $(Y_{1-y}Ca_y)Ba_2Cu_3O_{6+x}$ found at $p < p_{\rm sc1}$ is the response of dynamical stripes with a preferential orientation along the diagonal of the CuO_2 planes.

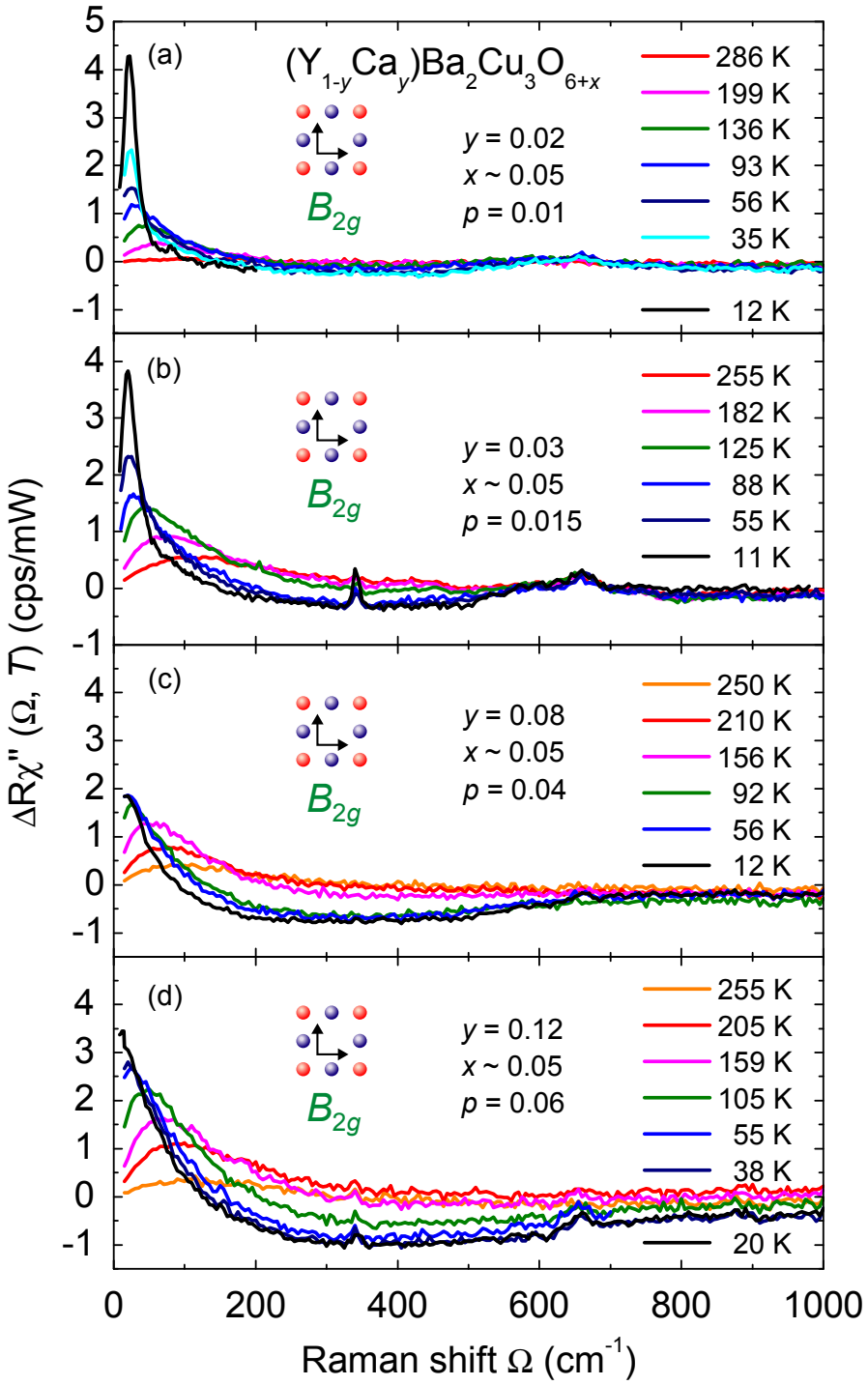

Figure 6.10: *B_{2g} Raman response of $(Y_{1-y}Ca_y)Ba_2Cu_3O_{6+x}$ after the subtraction of the electronic continuum. Temperatures, dopant concentrations, and doping levels are indicated.*

6.2.4 Temperature dependence

In Fig. 6.11 (a) and (b) the temperature dependence of the energies of the additional excitations in $La_{2-x}Sr_xCuO_4$ and $(Y_{1-y}Ca_y)Ba_2Cu_3O_{6+x}$ are plotted, respectively. In $La_{2-x}Sr_xCuO_4$ at $p = 0.10$ the peak position varies linearly with temperature above approximately 60 K and saturates at low temperature. Approximately the same behaviour is observed at $p = 0.12$, where the energy of the quasi-elastic peak saturates below approximately 50 K, and is approximately linear at high temperature. Finally, the same qualitative behaviour is observed also at $p = 0.02$ where the saturation occurs below 120 K. Here the linear part at high temperature is less defined than at $p = 0.10$ and 0.12.

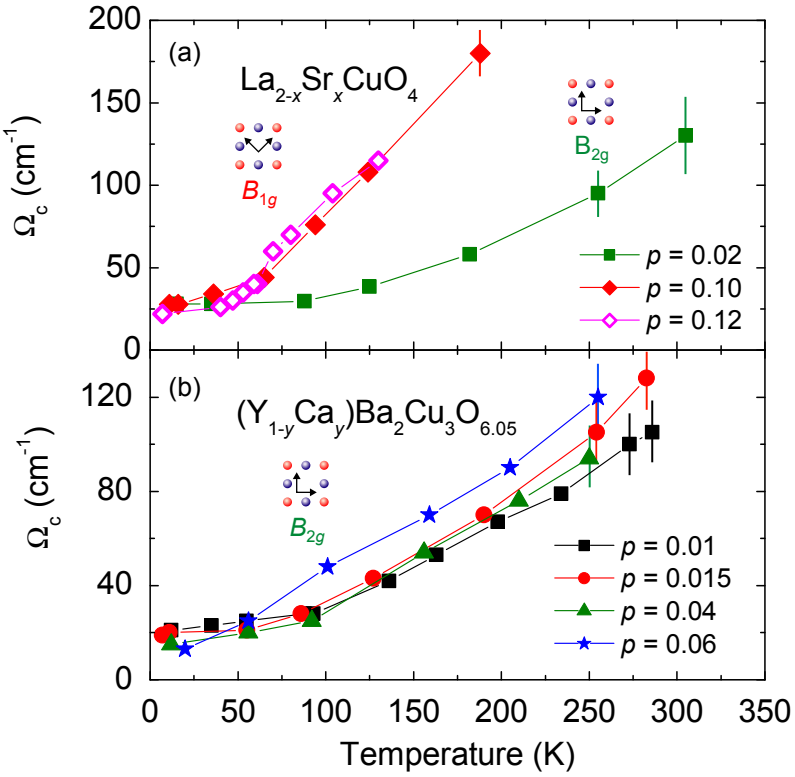

Figure 6.11: *Temperature dependence of the energy Ω_c of the quasi-elastic excitation in $La_{2-x}Sr_xCuO_4$ (a) and $(Y_{1-y}Ca_y)Ba_2Cu_3O_{6+x}$ (b) at different doping levels as indicated in the figure.*

The peak positions of the low-energy excitation in $(Y_{1-y}Ca_y)Ba_2Cu_3O_{6+x}$ in the range $0.01 < p < 0.04$ (Fig. 6.11 (b)) show a linear temperature dependence above approximately 100 K and saturates at lower temperatures. At $p = 0.06$ the temperature dependence of the peak energy is qualitatively different than at lower doping levels. Here it does not saturate down to the lowest temperature measured and the data extrapolate to zero energy linearly.

The temperature dependence of the additional response is typical for a system close to a quantum critical point (QCP) with the excitations reflecting the fluctuations [45, 116]. This point will be discussed in more detail in Sect. 6.3.2, where the implications of a QCP are discussed and compared with the experimental data.

6.3 Theory

In this section the experimental data are compared with a theoretical calculation of Raman response of fluctuating stripes, and the implications of a quantum critical point (QCP) connected with charge ordering on the physical properties are discussed. The hypothesis of a quantum critical point responsible for the peculiar behaviour of the normal state of cuprates around optimal doping and in the underdoped regime has been proposed by several authors (see Sect. 2.6). A QCP results from the competition between two ground states characterized by very similar energies but different order parameters, where the phase transition occurring at $T = 0$ is accomplished by changing a control parameter other than temperature, such as doping, pressure, magnetic field, etc. The competition between different ground states leads to fluctuations of the respective order parameters. The fluctuations lead to excitations in the energy spectrum of the system, eventually visible in the experiments. At present the nature of the ordered phase is unclear. One of the possible microscopic models for the cuprates around optimal doping and in the underdoped region is an incommensurate fluctuating charge density wave associated with the QCP, as indicated in various models [77].

6.3.1 Theoretical Raman response of dynamical stripes

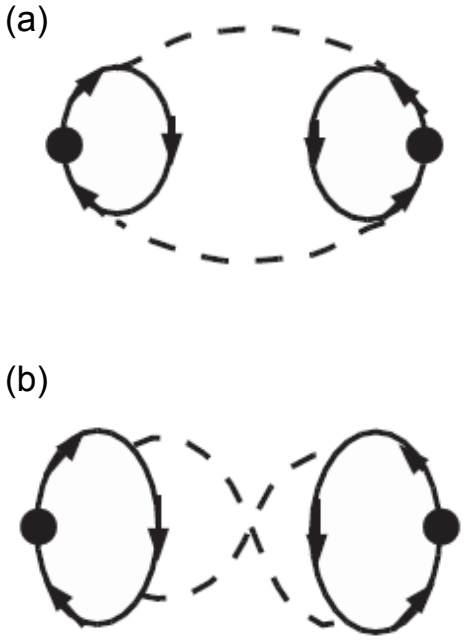

Figure 6.12: *Direct (a) and crossed (b) diagrams for the fluctuation contributions to Raman spectra. Dots, solid and dashed lines represent Raman vertices, fermionic QP propagators, and collective mode propagators, respectively. From Ref. [116].*

In order to check this proposal the Raman response of collective charge ordering (CO) excitations equivalent to stripe fluctuations is calculated and compared with the experimental data shown in Figs. 6.6 and 6.10. The role of fluctuations in the response functions was studied by Aslamazov and Larkin for the paraconductivity in superconductors [115]. This theory was extended to the particle-hole channel for one-dimensional charge-density-wave systems [147, 148]. The scheme was recently reconsidered for the Raman response in two dimensions [116]. The Feynman diagrams plotted in Fig. 6.12 represent the Raman response of incommensurate collective charge modes. These Raman diagrams generate important contributions, which depend on the selected symmetry. Each dashed line appearing in the diagrams in Figs. 6.12 (a) and (b) represent a Gaussian diffusive collective mode propagator

$$D(\mathbf{q}, \omega_m) = (|\omega_m| + \Omega_{\mathbf{q}})^{-1} \tag{6.1}$$

with $\Omega_{\mathbf{q}} = \nu|\mathbf{q} - \mathbf{q}_c|^2 + m(x,T)$ with ν a constant electronic energy scale. $m(x,T) \propto \xi^{-2} \propto \Big(T - T_{\mathrm{CO}}(x)\Big)$ is the mass of the collective modes and encodes via the charge-ordering (CO) correlation length ξ the distance from the

critical line $T_{\rm CO}(x)$ [78, 102, 44]. This propagator is largest at zero frequency and at $\mathbf{q} = \mathbf{q}_c$, the wave vector setting the modulation of the most singular charge fluctuations. The fermionic loops in Figs. 6.12 1(a) and 1(b) have the form

$$\Lambda_{\alpha,\beta}(\Omega_l;\mathbf{q},\omega_m) = CT\sum_n\sum_k \gamma_{\alpha,\beta}(\mathbf{k})G(\mathbf{k},\epsilon_n+\Omega_n)G(\mathbf{k}-\mathbf{q},\epsilon_n-\Omega_n)G(\mathbf{k},\epsilon_n), \tag{6.2}$$

with $\gamma_{\alpha,\beta}(\mathbf{k})$ the Raman vertex, and C a constant determined by the coupling of the Raman vertex with the incoming and outgoing photons and the coupling g of the collective modes with the fermions. Since the dominant contributions of the diagrams in Figs. 6.12 (a) and (b) occur when the collective modes are around $\mathbf{q}_c$, Eq. (6.2) is evaluated for $\mathbf{q} = \mathbf{q}_c$. In the $\mathbf{k}$ summation the largest contribution is obtained when the three fermions are around the regions on the Fermi surface that are connected by $|\mathbf{q_c}|$.

Here, the two relevant cases corresponding to Raman verteces with B_{1g} and B_{2g} symmetry will be discussed, and the Raman selection rules will be derived. $\gamma_{B_{1g}} = \cos(k_x) - \cos(k_y)$ vanishes along the Brillouin zone diagonals and changes sign under $x-y$ interchange (see section 3.4). In the case of B_{1g} symmetry, regions with the same sign are connected by the modulation vector of stripes or eggbox charge-ordering fluctuations with preferential direction along the Cu − O bonds, as indicated in Fig. 6.13 (a). When the Raman vertex of B_{2g} symmetry, $\gamma_{B_{2g}} = \sin(k_x)\sin(k_y)$ (see section 3.4), is considered for the same $\mathbf{q}_c$, the leading contribution vanishes since the regions connected by $\mathbf{q}_c$ (see Fig. 6.13 (b)) give contributions from regions whith opposite sign. The reverse occurs when the modulation vector is directed along the diagonal of the CuO_2 plane. Then again regions in $\mathbf{k}$-space with the same sign are connected by $\mathbf{q}_c$. The leading contribution to Eq. (6.2) is finite in B_{2g} symmetry, while it vanishes in B_{1g} symmetry.

Using similar arguments it is possible to show that the spin collective modes at $\mathbf{q}_c = (\pm\pi, \pm\pi)$ and with diagonal wave vectors $\mathbf{q}_c \approx (\pm(\pi - \delta), \pm(\pi - \delta))$ give vanishing contributions for B_{1g} and B_{2g} symmetry [116].

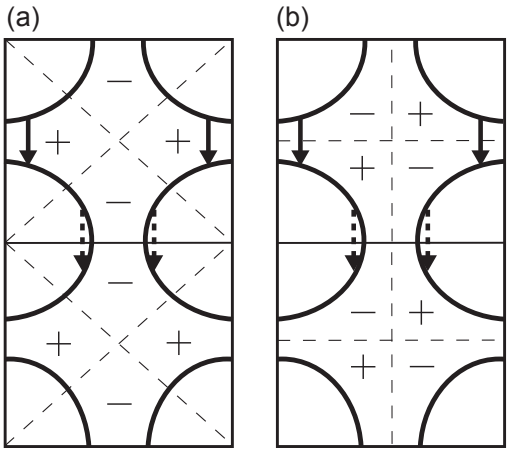

Figure 6.13: *Sketch of symmetry selection rules for charge-ordering (CO) fluctuations. Hot spots connected by the critical wave vector* $\mathbf{q_c} = (0, -q_c)$ *are represented by arrows. Equivalent hot spots have arrows of the same type (solid or dashed). The signs + and - indicate the regions where the Raman vertices (*B_{1g} *and* B_{2g}*) are positive and negative, respectively. From Ref. [116].*

However, for small vertical and horizontal incommensuration $\mathbf{q}_c = (\pm(\pi-\delta), \pm\pi), (\pm\pi, \pm(\pi-\delta))$, there is no complete cancellation in B_{1g} symmetry and a finite contribution of spin collective modes in Eq. (6.2) cannot be excluded. Summarizing, a small contribution from spin collective modes could add to the CO contribution at not too small doping for $La_{2-x}Sr_xCuO_4$ where the stripes are expected to be incommensurate and along the Cu−O bond direction, while only the response of collective charge order should be present in the deeply underdoped regime of $La_{2-x}Sr_xCuO_4$ with diagonal order.

The resulting contribution from collective modes, $\Delta\chi''_B$ ($B = B_{1g}, B_{2g}$), to Raman scattering was calculated in Ref. [116]. The theoretical curves for $\Delta\chi''$ are shown in Fig. 6.14 (reproduced from Ref. [116]), together with the experimental data measured in this thesis. The theoretical calculations agree with the experimental data corroborating the interpretation of the quasi-elastic peaks in terms of fluctuating stripes. The strong temperature dependence of the Raman peaks is basically governed by the temperature dependence of the low-energy scale $m(T)$.

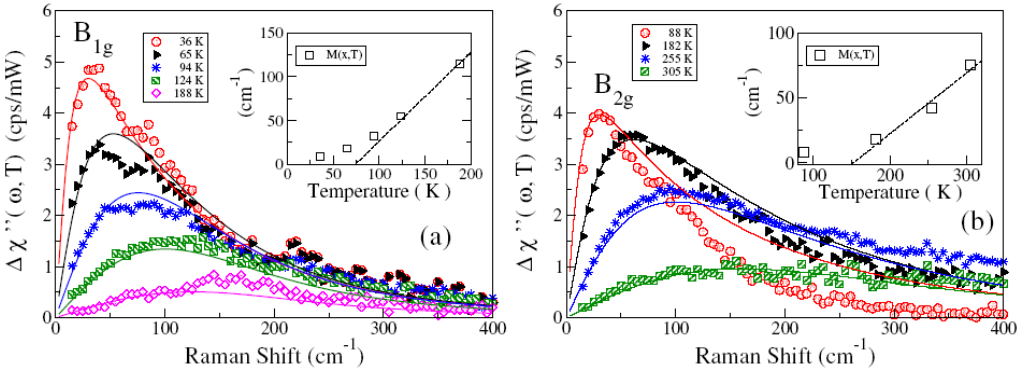

Figure 6.14: *Comparison between the additional Raman response and the calculated Raman response due to collective charge order fluctuations of* $La_{2-x}Sr_xCuO_4$ *at* $x = 0.10$ *(a) and* $x = 0.02$ *(b). The mass used to fit the curves at different temperatures is reported in the inset. Experimental data measured in this thesis; figure from Ref. [116].*

6.3.2 Quantum critical point

The theory of quantum critical points can be summarized in the diagram shown in Fig. 6.15 [77, 149] where δ is the controll parameter that can be doping, pressure, magnetic field, etc. A quantum critical point divides the phase diagram into three regions: the "ordered" phase (where the system is partially ordered at $T > 0$) on the left hand side of the quantum critical point, the quantum critical region, above the quantum critical point, and the quantum disordered region, on the right hand side. The various regions are characterized by different functional dependences of the mass m in the collective mode propagator (Eq. (6.1)). For a quantum critical point associated with a charge density instability $m \propto (T - T^*)$ holds in the quantum critical regime and $m \propto (\delta - \delta_c)$ in the quantum disordered regime, with δ_c the critical value of the controll parameter marking the quantum critical point (Fig. 6.15). The simultaneous excitation of two collective modes leads to a Raman peak with energy $\Omega_c \propto m$, and therefore Ω_c should show the same functional dependence as the mass m. The characteristic energies of the additional response plotted in Fig. 6.11 show a behaviour consistent with that of the mass of critical modes in the underdoped regime, since the peak posi-

tion varies linearly with temperature for $T > T^*$, while below the crossover temperature T^* the mode practically saturates in the partially ordered phase where the charge ordering transition is quenched by other effects [44, 116]. Therefore, also the temperature dependence of the additional Raman response supports the interpretation of the additional excitation in terms of dynamical stripes.

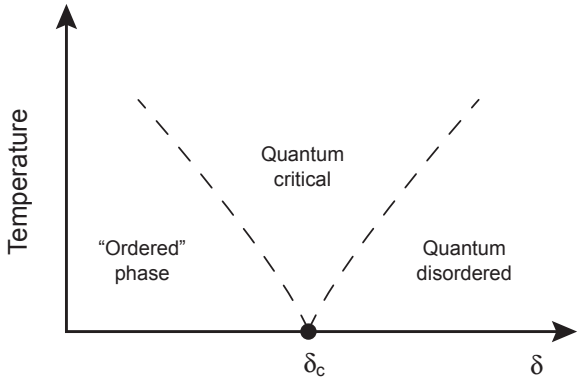

Figure 6.15: *Schematic representation of the phase diagram around a quantum critical point (QCP). The QCP divides the phase diagram in three regions: "ordered", quantum critical, and quantum disordered, on the left, above, and on the right hand side of the QCP, respectively. δ is the control parameter that can be doping, pressure, magnetic field, etc.*

The saturation of the characteristic energy determines T^*. Ω_c of $La_{2-x}Sr_xCuO_4$ at $p = 0.02$, 0.010. and 0.12 saturates around 120 K, 60 K, and below 50 K, respectively. However, due to the limited number of experimental points and to the large error bars of the peak positions at the highest temperatures seriously affecting the results of the linear extrapolation to zero of Ω_c, the estimated T^*s have large error bars. The data of the three samples can be mapped on top of each other by scaling the temperature by a factor of approximately 2 between $p = 0.02$ and 0.10, and 2.5 between $p = 0.02$ and 0.12, $\Omega_c(0.02, T) \approx \Omega_c(0.10, 2T) \approx \Omega_c(0.12, 2.5T)$ (see Fig. 6.16), corroborating $T^*(0.02) \approx 2T^*(0.10) \approx 2.5T^*(0.12)$. Even if the absolute numbers obtained for T^* are accurate only to within $\pm 20\%$, the ratios of the T^*s at the various doping levels are robust. Therefore, in order to obtain an estimate of x_c (here δ corresponds to the doping x) the relation $\Omega_c(0.02, T) \approx \Omega_c(0.10, 2T) \approx \Omega_c(0.12, 2.5T)$ is used. Assuming a linear dependence of T^* on the control parameter x $T^*(x) \propto |x - x_c|$ as supported

by both theory and experiment [13, 44, 102, 150], the result $x_c = 0.18 \pm 0.02$ is obtained [146].

In spite of the good agreement of x_c with the expected value, this result has to be treated with care. The procedure applied to estimate x_c is correct only in the hypothesis of a single QCP effecting the properties of the normal state of cuprates. Measurements of $(Y_{1-y}Ca_y)Ba_2Cu_3O_{6+x}$ indicate that this could not be the case. The data of $(Y_{1-y}Ca_y)Ba_2Cu_3O_{6+x}$ at $p = 0.06$ show a linear temperature dependence of the energy Ω_c of the additional peak down to very low temperature, while at lower doping levels the high temperature linear part saturate at low temperature (Fig.6.11 (b)). The experimental evidence that at $p = 0.06$ temperature is the only energy scale, and therefore that the system never enter the quasi-ordered phase, indicates a quantum critical point around $p = 0.06$.

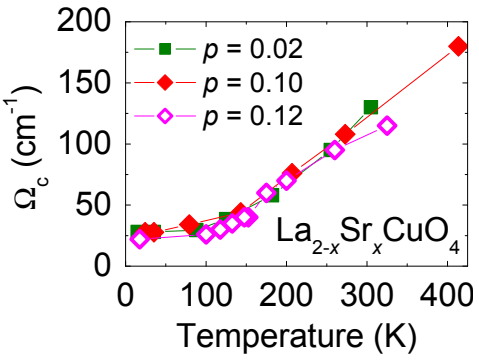

Figure 6.16: *Characteristic energies of the low-energy peaks plotted with temperatures changed by a factor of approximately 2 at $p = 0.10$, and 2.5 at $p = 0.12$.*

The picture is complicated, and different phenomena superimpose. It is possible that different quantum critical points, associated with a different type of charge order, determine the normal properties of cuprates at different doping regimes. Additional experimental and theoretical work is needed in order to have a complete understanding of the underdoped normal state of cuprates. However, the Raman data measured in this thesis highlight the importance of charge ordering and quantum critical points in the context of cuprates.

6.4 $La_{1.88}Sr_{0.12}CuO_4$ and $La_{1.875}Ba_{0.075}Sr_{0.05}CuO_4$

In this section the data of $La_{1.875}Ba_{0.075}Sr_{0.05}CuO_4$ and $La_{2-x}Sr_xCuO_4$ at similar doping levels $p = 0.125$ and 0.12, respectively, are discussed. $La_{1.875}Ba_{0.075}Sr_{0.05}CuheyO_4$ at 1/8 filling shows evidence of static charge and spin ordering (stripes) below an ordering temperature $T_{CO} \approx 37$ K [73] as shown in Fig. 6.17 reproduced from Ref. [73].

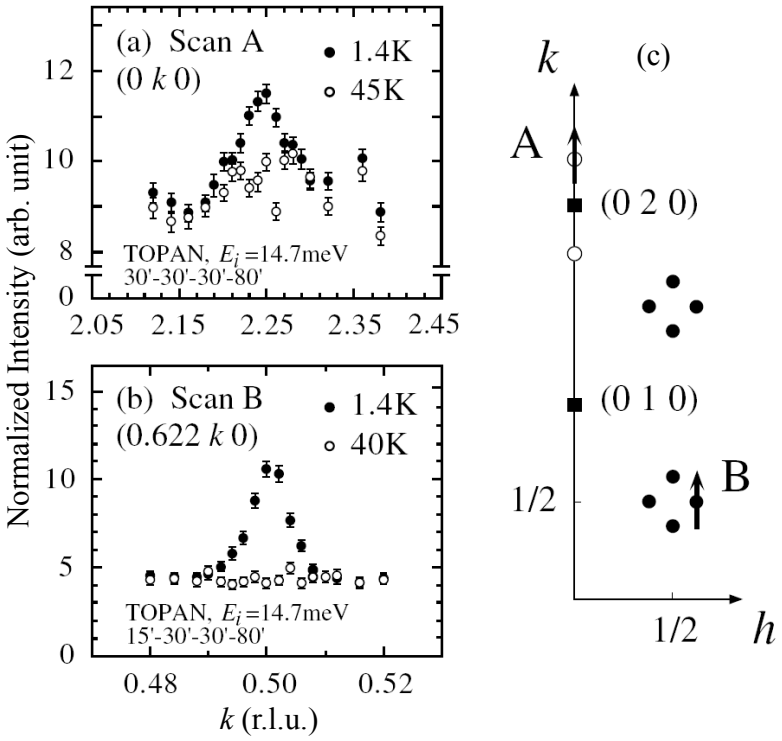

Figure 6.17: *Incommensurate peaks from charge-density-waves (CDW) (a) and spin-density-waves (SDW) (b) orders in $La_{1.875}Ba_{0.075}Sr_{0.05}CuO_4$. Closed and open circles referred to measurements below and above with respect to the ordering temperature T_{d2}, respectively. (c) Scan geometry in the (h, k, 0) tetragonal plane. Closed squares referred to nuclear Bragg peaks, while open and closed circles denote nuclear and magnetic incommensurate superlattice peaks, respectively. From Ref. [73].*

Above the ordering temperature the stripes melt and probably the charge and spin ordering become dynamic. Therefore, data of $La_{1.875}Ba_{0.075}Sr_{0.05}CuO_4$ are particular interesting since they allow the comparison of the Raman response $\chi''(\Omega, T)$ of the ordered state with that of the dynamical regime.

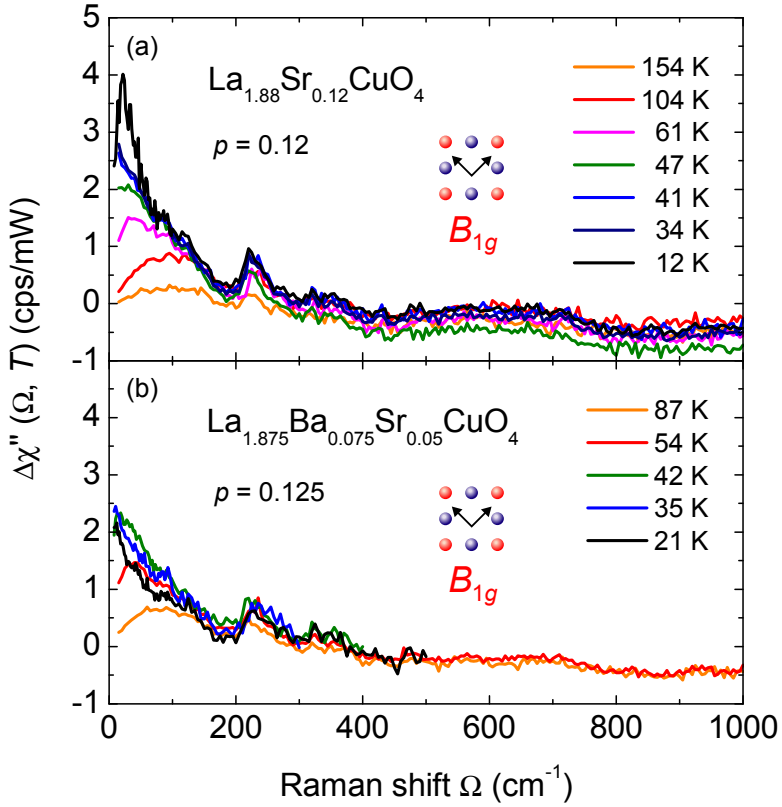

Figure 6.18: *(a) B_{1g} Raman response of $La_{1.88}Sr_{0.12}CuO_4$ after the subtraction of the electronic response at different temperatures, as indicated in the figure. The subtraction procedure of the electronic response is described in Sect. 6.2.1. (b) Same as (a) for $La_{1.875}Ba_{0.075}Sr_{0.05}CuO_4$.*

In addition the comparison of the data of $La_{1.875}Ba_{0.075}Sr_{0.05}CuO_4$ with those of $La_{2-x}Sr_xCuO_4$ allows one to compare $\chi''(\Omega, T)$ of two systems at similar doping levels, one entering an ordered phase at low temperature while the other stays in the dynamical regime.

The B_{1g} Raman responses of $La_{1.875}Ba_{0.075}Sr_{0.05}CuO_4$ and $La_{1.88}Sr_{0.12}CuO_4$ are plotted in Fig. 5.2 (b) and (a), respectively. The

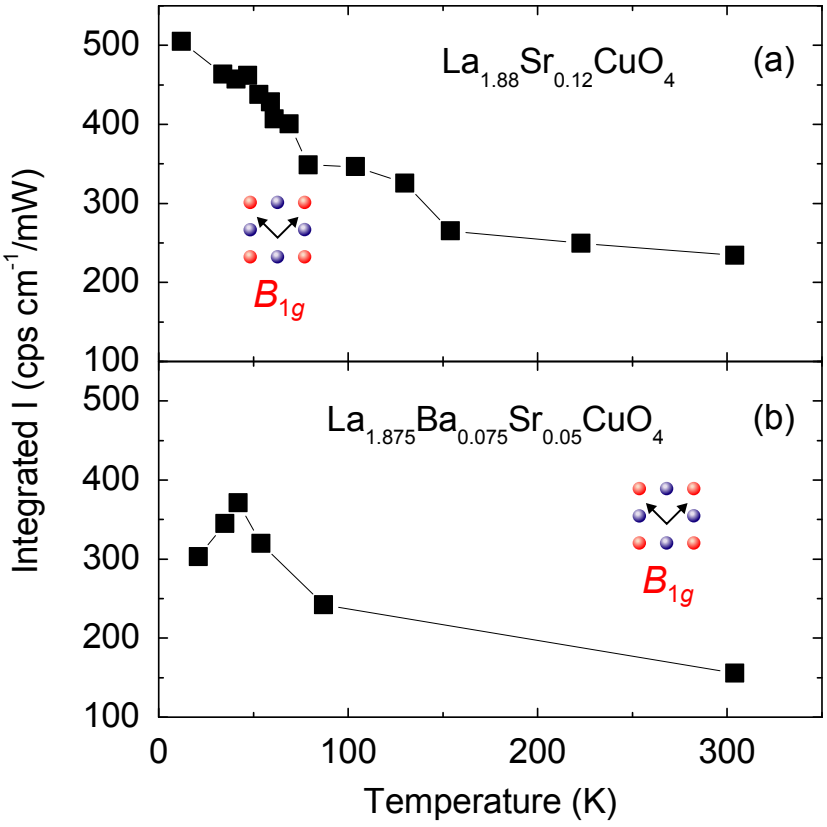

Figure 6.19: *Integrated area of the quasi elastic excitation in the range 15-200 cm^{-1} for $La_{1.88}Sr_{0.12}CuO_4$ (a) and $La_{1.875}Ba_{0.075}Sr_{0.05}CuO_4$ (b).*

data of $La_{1.875}Ba_{0.075}Sr_{0.05}CuO_4$ show a peak at very low energy, emerging upon cooling, that, at first glance, resembles very much the Raman response of $La_{1.88}Sr_{0.12}CuO_4$. In order to better analyze the temperature dependence of the low-energy peak the contribution of the electronic continuum can be subtracted from the experimental data of $La_{1.875}Ba_{0.075}Sr_{0.05}CuO_4$

(Fig. 6.18) applying the same procedure described for $La_{2-x}Sr_xCuO_4$ in Sect. 5.1. At $T > T_{CO}$ the Raman response of $La_{1.875}Ba_{0.075}Sr_{0.05}CuO_4$ and $La_{1.88}Sr_{0.12}CuO_4$ is the same, and the low-energy peaks show the same temperature dependence for both compounds (Fig. 6.18). At $T < T_{CO}$ the spectra of $La_{1.875}Ba_{0.075}Sr_{0.05}CuO_4$ and $La_{1.88}Sr_{0.12}CuO_4$ show a different behaviour of the quasi-elastic peak. Upon reducing the temperature the peak increases monotonically in $La_{1.88}Sr_{0.12}CuO_4$, while in $La_{1.875}Ba_{0.075}Sr_{0.05}CuO_4$ it increases down to T_{CO} but then decreases in the ordered phase. This behaviour can be better visualized when the integrated area of the additional response is plotted as a function of temperature (Fig. 6.19).

The experimental observation that the additional peak measured in $La_{1.88}Sr_{0.12}CuO_4$ (and in $La_{1.90}Sr_{0.10}CuO_4$) shows the same shape, energy and temperature dependence as that in $La_{1.875}Ba_{0.075}Sr_{0.05}CuO_4$ above T_{CO}, meaning a system with dynamical stripes, corroborates the hypothesis that the quasi-elastic peak is the response of fluctuating stripes. Further support comes from the reduction of the intensity of the additional response of $La_{1.875}Ba_{0.075}Sr_{0.05}CuO_4$ below T_{CO}. The Raman response is obviously expected to vanish for static order, at least below a threshold energy corresponding to the pinning energy of the stripes. The decreasing in intensity of the additional response is a signature of the static order. The fact that the quasi-elastic peak only decreases in intensity but does not vanish indicates that only a fraction of the stripes is frozen.

The B_{2g} spectra of $La_{1.875}Ba_{0.075}Sr_{0.05}CuO_4$ show a behaviour similar to that of the B_{1g} channel. Above the ordering temperature the Raman response of $La_{1.875}Ba_{0.075}Sr_{0.05}CuO_4$ and $La_{1.88}Sr_{0.12}CuO_4$ are practically equal (see Fig. 5.2 (c) and (d)). Below the ordering temperature the B_{2g} data of $La_{1.875}Ba_{0.075}Sr_{0.05}CuO_4$ show a loss of spectral weight up to approximately 600 cm^{-1}. In the ordered phase the spectral weight reduces by approximately 30%.

This spectral weight depletion resembles that observed in $(Y_{1-y}Ca_y)Ba_2Cu_3O_{6+x}$ and $Bi_2Sr_2CaCu_2O_{8+\delta}$ at similar doping levels

but much higher temperature due to the pseudogap (see Sect. 6.5). Here the spectral weight depletion is at least 50% larger than in the pseudogap regime of $(Y_{1-y}Ca_y)Ba_2Cu_3O_{6+x}$ and $Bi_2Sr_2CaCu_2O_{8+\delta}$. Therefore, the data of $La_{1.875}Ba_{0.075}Sr_{0.05}CuO_4$ show which kind of effect can be observed in the Raman spectra due to correlation effects leading to charge and spin order. This observation suggest that the B_{2g} pseudogap (see Sect. 6.5) could originate from charge and spin ordering phenomena.

6.5 Pseudogap

The pseudogap is a reduction of the density of states observed in the normal state of cuprates. It was originally found at the Fermi surface crossing close to $(\pi, 0)$ and is smaller around the zone diagonal ([13] and reference therein, and Sect. 2.4). At present the pseudogap phenomenon is one of the most important unsolved problems in the cuprates and it is a matter of intense research. The commonly considered scenarios are fluctuating superconductivity and quantum critical points. The fluctuating superconductivity picture refers to the idea that superconductivity in the underdoped range is determined by the phase stiffness of the superfluid [151, 152, 153, 154, 155]. In this frame work the pseudogap would be a precursor of superconductivity and it would reflect pre-formed Cooper pairs without phase coherence below the crossover temperature $T^* > T_c$. On the other hand, in the quantum-critical-point scenario the superconducting gap and the pseudogap would be of different origin, and the suppression of T_c in the underdoped regime would be determined by the development of competing ordered phases. In this context, the proposed microscopic descriptions for the pseudogap phase are charge-density-waves [78], a flux phase with spontaneous orbital currents [98, 99], and d-density-wave short-range fluctuations [156]. Finally, in addition to fluctuating superconductivity and quantum critical points it was also proposed that the pseudogap could result from antiferromagnetic spin fluctuation and spinon pairing [157, 158, 159, 160, 161].

In this section Raman scattering measurements of the pseudogap of $La_{2-x}Sr_xCuO_4$ and $(Y_{1-y}Ca_y)Ba_2Cu_3O_{6+x}$ are discussed. In particular, the pseudogap in the range $p < p_{sc1}$ is discussed which was discovered for the first time in the work described here. So far it was believed that the pseudogap has only one energy scale. However, here three distinct energy scales of the pseudogap were found. Indications of spin and charge order has a possible mechanism for the B_{2g} pseudogap were found.

6.5.1 B_{2g} symmetry

Here the pseudogap observed in B_{2g} is discussed for $La_{2-x}Sr_xCuO_4$ and $(Y_{1-y}Ca_y)Ba_2Cu_3O_{6+x}$. The B_{2g} spectra of $(Y_{1-y}Ca_y)Ba_2Cu_3O_{6+x}$ in the range $0.01 \leq p \leq 0.06$ (Figs. 5.13 (b-e) and 5.11 (b-e)) show a loss of spectral weight below approximately 600 cm^{-1} upon cooling. The energy range of the spectral weight depletion increases with doping, being visible approximately up to 700 cm^{-1} at $p = 0.06$. A loss of spectral weight in B_{2g} symmetry below approximately 700 cm^{-1} was observed in previous studies at higher doping levels and interpreted as an effect of the pseudogap [71, 122]. At $p = 0.04$ and more clearly at $p = 0.06$ a second spectral weight depletion, extending at least up to 3000 cm^{-1}, is visible (Figs. 5.11 (d) and (e)). In the rest of the section the high- and the low-energy losses of spectral weight are referred to as the small and the large pseudogap, respectively. The small and the large pseudogap become effective at different doping levels indicating that the two features are probably independent. A spectral weight depletion is detected also in the B_{2g} spectra of $La_{1.98}Sr_{0.02}CuO_4$ ($p = 0.02$). Here only a single pseudogap is observed below approximately 800 cm^{-1}, and this spectral weight depletion resembles very much the small pseudogap of $(Y_{1-y}Ca_y)Ba_2Cu_3O_{6+x}$. The data measured in this thesis show for the first time evidence of the pseudogap also in underdoped non-superconducting samples, down to $p = 0.01$.

Above the onset point of superconductivity (p_{sc1}) the pseudogap changes qualitatively. At $p = 0.07$ the loss of spectral weight in $(Y_{1-y}Ca_y)Ba_2Cu_3O_{6+x}$ has a much smaller magnitude than that of the small pseudogap at $p = 0.06$,

and it has a wider energy range extending at least up to 1000 cm^{-1}. At $p > p_{sc1}$ only one energy scale of the pseudogap is visible. Moreover, also the temperature dependences of the spectral weight depletions at $p > p_{sc1}$ and $p < p_{sc1}$ are different. At $p = 0.07$ the spectral weight drops abruptly below approximately 150 K while at $p < p_{sc1}$ the spectral weight depletion is more continuous upon reducing the temperature (compare Figs. 5.13 (a-d) and 5.13 (e), and Figs. 6.21 (a-d) and 6.21 (e)). A qualitative change of the pseudogap across p_{sc1} is observed also in $La_{2-x}Sr_xCuO_4$. Here, the pseudogap vanishes above p_{sc1} (Figs. 5.1 (d) and 5.2 (c)). Likely the loss of spectral weight becomes too weak to be resolved in the present measurements. The latter result is in contrast with previous studies where evidence of the pseudogap was found for B_{2g} symmetry in $La_{2-x}Sr_xCuO_4$ at $x = 0.08$, 0.11, and 0.13 [162]. Here, the B_{2g} pseudogap was deduced from a reduction of Raman scattering rates upon cooling, rather than by a spectral weight depletion. However, Raman rates measured in this thesis show the opposite temperature dependence. The two sets of data cannot be reconciled. The different quality of the samples could be an explanation.

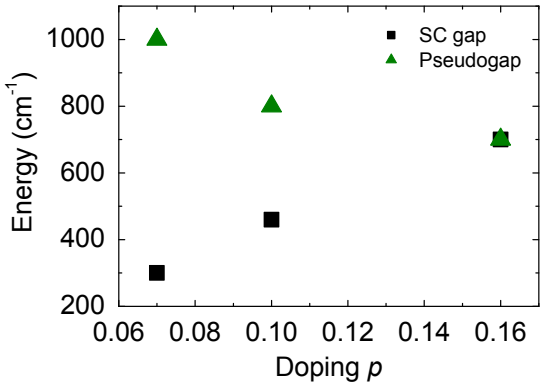

Figure 6.20: *Energy of the superconduting gap and energy range of the pseudogap at $p = 0.07$, 0.10, and 0.16 in $(Y_{1-y}Ca_y)Ba_2Cu_3O_{6+x}$. Data at $p = 0.10$ and 0.16 are from Ref. [71] and [122], respectively.*

Previous Raman scattering measurements, performed on $YBa_2Cu_3O_{6+x}$ at $p \approx 0.10$, showed that the superconducting gap and the pseudogap (both measured in B_{2g} symmetry) have different energy ranges [71]. Here the energy ranges of the pseudogap and of the superconducting gap are defined as

the energy at which loss and gain, respectively, of spectral weight become visible. With those definitions the pseudogap of $YBa_2Cu_3O_{6+x}$ at $p \approx 0.10$ is approximately 30% wider than the superconducting gap. The data of $(Y_{0.92}Ca_{0.08})Ba_2Cu_3O_{6.30}$ ($p = 0.07$) measured in this thesis confirm these results. Here, the pseudogap is at least 3 times as large as the superconducting gap. In addition, it is shown that the superconducting gap and the pseudogap have the opposite doping dependence. In Fig. 6.20 the superconducting gap and the pseudogap energy ranges at $p = 0.07$, 0.10, and 0.16 are plotted. The superconducting gap increases proportional to T_c. The data at $p = 0.07$ do not show a clear energy onset of the pseudogap (see Fig 5.11 (f)). However, a spectral weight depletion at $p = 0.07$ is clearly visible up to at least 1000 cm^{-1}, while at $p = 0.10$ and 0.16 the pseudogap closes at around 800 and 700 cm^{-1}, respectively [71, 122]. Qualitatively similar results are obtained if the energy of the superconducting-induced peaks are plotted. This experiment indicates that pseudogap and superconducting gap have different origins, and therefore the phase fluctuation picture is at least insufficient for explaining the pseudogap.

On the other hand, below the onset point of superconductivity the B_{2g} spectra of both $La_{2-x}Sr_xCuO_4$ and $(Y_{1-y}Ca_y)Ba_2Cu_3O_{6+x}$ show the quasi-elastic peak and a loss of spectral weight in the range $200 - 700$ cm^{-1}. The two features show a similar temperature dependence upon cooling. Crossing p_{sc1} the low-energy peak in B_{2g} symmetry vanishes for both compounds, and the pseudogap vanishes in $La_{2-x}Sr_xCuO_4$ and changes qualitatively in $(Y_{1-y}Ca_y)Ba_2Cu_3O_{6+x}$ as described above. These observations suggest a possible relationship between the pseudogap and the low-energy excitation. In Fig. 6.21 the integrated intensities of the low-energy peak ($15-200$ cm^{-1}) and of the part of the spectra where the spectral weight depletion is maximal ($300-500$ cm^{-1}) are plotted as a function of temperature. In $(Y_{1-y}Ca_y)Ba_2Cu_3O_{6+x}$ the integrated area of the quasi-elastic peak increases approximately linearly upon cooling at high temperature, reaches a maximum and slowly decreases at low temperature. This behaviour is found at all

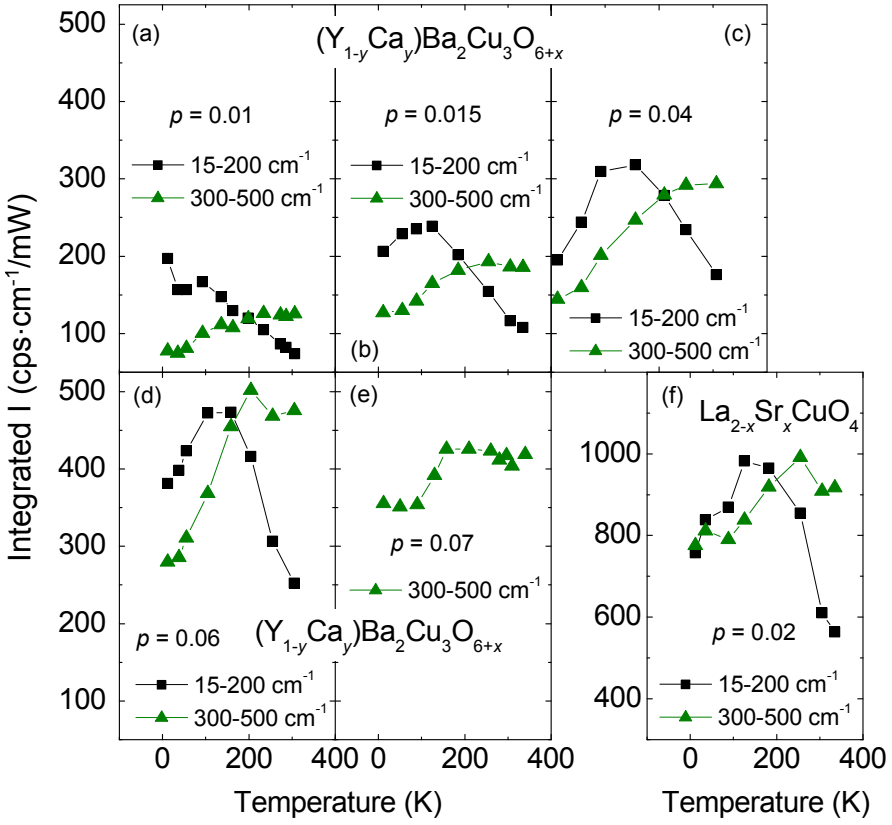

Figure 6.21: *(a) Integrated intensity of the quasi elastic excitation (15-200 cm^{-1}) and of the part of the spectra where the spectral weight depletion is maximal (300-500 cm^{-1}) for $(Y_{1-y}Ca_y)Ba_2Cu_3O_{6+x}$ at $p = 0.01$. (b), (c), and (d) Same as (a) for $(Y_{1-y}Ca_y)Ba_2Cu_3O_{6+x}$ at $p = 0.015$, 0.04, and 0.06, respectively. (e) Integrated intensity of the pseudogap (300-500 cm^{-1}) for $(Y_{1-y}Ca_y)Ba_2Cu_3O_{6+x}$ at $p = 0.07$. (f) Same as (a) for $La_{1.98}Sr_{0.02}CuO_4$ ($p = 0.02$).*

studied doping levels except for $p = 0.01$ where the integrated intensity at the lowest temperature has the biggest magnitude. In $La_{2-x}Sr_xCuO_4$ the average intensity of the quasi-elastic peak and of the spectral weight in the pseudogap range show the same qualitative behaviour as in $(Y_{1-y}Ca_y)Ba_2Cu_3O_{6+x}$. In both cases the low-energy peak and the pseudogap show different onset temperatures. Therefore, a relationship between these two phenomena can not be directly derived from the data. However, it has been shown in a measurement of $La_{1.74}Sr_{0.26}CuO_4$ that the spectral weight increases upon cooling in a wide temperature range before it decreases at low temperature [163]. There-

fore a partial compensation of the pseudogap effect and an increase of spectral weight upon cooling cannot be excluded. This may effect the individual onset temperatures of the low-energy peak and of the pseudogap, and they could originate from the same charge and spin ordering phenomena. The hypothesis that ordering phenomena could lead to suppression of spectral weight is supported also by the measurements performed on $La_{1.875}Ba_{0.075}Sr_{0.05}CuO_4$. Here, the spectral weight of the B_{2g} Raman response is suppressed by at least 30% in the ordered state (Fig. 5.2 (d)). Suppression of spectral weight can be expected also with dynamical order, and charge and spin order are good candidates to explain the small pseudogap in B_{2g} symmetry.

6.5.2 B_{1g} symmetry

Change of spectral weight is also observed in B_{1g} symmetry. The Raman response of $(Y_{1-y}Ca_y)Ba_2Cu_3O_{6+x}$ is plotted in Figs. 5.6 and 5.8. The data at $p < p_{sc1}$ show a loss of spectral weight in a wide frequency range, approximately up to 2500 cm^{-1}, where the intensity continuously decreases upon cooling. The loss of spectral weight is almost linear with temperature, as shown in Fig. 6.22 (a) where the integrated intensities in the range $800 - 2500$ cm^{-1} are plotted. Therefore, in addition to the different energy range the reduction of spectral weight in B_{1g} symmetry shows also a temperature dependence different from that of the small pseudogap in B_{2g} symmetry (compare Figs. 6.21, and 6.22). This experimental evidence suggests a different mechanism for the pseudogap in B_{1g} and B_{2g} symmetries. A loss of spectral weight is visible also in the B_{1g} spectra of $La_{1.98}Sr_{0.02}CuO_4$ (Fig. 5.1 (a)). Due to a technical problem of the cryopumping system occurred during the measurements it was not possible to properly measure spectra up to high energy, and information at energies higher than 1000 cm^{-1} is missing. However, the low-energy spectra of $La_{1.98}Sr_{0.02}CuO_4$ and $(Y_{1-y}Ca_y)Ba_2Cu_3O_{6+x}$ at $p < p_{sc1}$ are similar and the integrated intensities in the range $800-1000$ cm^{-1} show similar temperature dependences (Fig. 6.22 (b)).

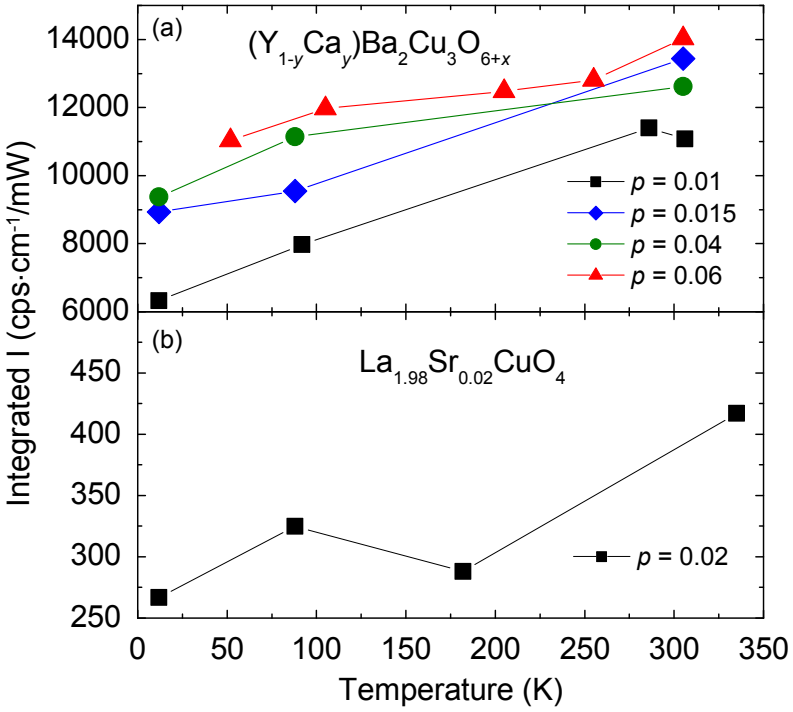

Figure 6.22: *(a) Integrated intensities in the pseudogap part of the spectra (800-2500 cm^{-1}) for differently doped $(Y_{1-y}Ca_y)Ba_2Cu_3O_{6+x}$ at B_{1g} symmetry as function of temperature. The doping levels are indicated. (b) Integrated intensities in the phonon free part of the spectra (800-1000 cm^{-1}) at B_{1g} symmetry as function of temperature.*

For $p > p_{sc1}$ the B_{1g} pseudogap hardly changes its behaviour. This can be seen in both $(Y_{1-y}Ca_y)Ba_2Cu_3O_{6+x}$ and $La_{2-x}Sr_xCuO_4$. In $(Y_{1-y}Ca_y)Ba_2Cu_3O_{6+x}$ one is confined to the temperature range below 250 K since strong phonon resonances partially cancel the pseudogap above 250 K.

The data of $La_{1.90}Sr_{0.10}CuO_4$ at $p = 0.10 > p_{sc1}$ do not show any evidence of the B_{1g} pseudogap. However, data of $La_{1.88}Sr_{0.12}CuO_4$ ($p = 0.12$) show a spectral weight depletion similar to that of $La_{1.98}Sr_{0.02}CuO_4$ in the range $200 - 1000$ cm^{-1}. Indications of a B_{1g} pseudogap come also by measurements performed on $La_{1.82}Sr_{0.08}CuO_4$ ($p = 0.08$) [164]. Apparently, the B_{1g} pseudogap does not change across p_{sc1} for $La_{2-x}Sr_xCuO_4$ either.

A possible mechanism for the B_{1g} spectral weight depletion could be con-

nected with correlation effects. For instance it has been shown in a theoretical study of the Falicov-Kimball model at zero doping [165] that the B_{1g} Raman response develops an isosbestic point and spectral weight is shifted from the low-energy part to higher energy, upon increasing the interaction strength. The calculation provides only a qualitative indication, since the Falikov-Kimball model is not the physically relevant model for all correlated systems. However, it provides information on the possible effects of correlations in the Raman response suggesting electronic correlations as a good candidate for the mechanism leading to the B_{1g} pseudogap.

6.6 Ordering phenomena and superconductivity

The discovery of a new ordered phase observed for the first time in $La_{1.48}Nd_{0.4}Sr_{0.12}CuO_4$ and characterized by a static charge and spin modulation (see Fig. 2.8), and the observation of dynamical stripes in underdoped $La_{2-x}Sr_xCuO_4$ and $(Y_{1-y}Ca_y)Ba_2Cu_3O_{6+x}$ (Sect. 6.2.3.2 and 6.2.3.2) raise new questions. One issue is whether charge and spin order is a general feature of cuprates, and the second being which kind of order takes place in different compounds and different doping levels. Another important question is whether or not there is a relationship between ordering phenomena and superconductivity in the cuprates.

In this section results on charge and spin order obtained in this work for two compounds characterized by very different maximal critical temperatures ($La_{2-x}Sr_xCuO_4$ and $(Y_{1-y}Ca_y)Ba_2Cu_3O_{6+x}$) are compared and discussed.

6.6.1 Renormalization effects across p_{sc1}

Here the doping dependences of the two-magnon excitation and of the B_{1g} phonon are described. The implications on charge and spin order are discussed.

6.6.1.1 Two-magnon excitation in $(Y_{1-y}Ca_y)Ba_2Cu_3O_{6+x}$

In Fig 6.23 the energy of the two-magnon excitation is plotted. Up to the onset point of superconductivity p_{sc1} the peak position is practically constant, while crossing p_{sc1} it drops by approximately 250 cm^{-1}. The two-magnon excitation corresponds to an effective two-spin flip and the scattering process is plotted in Fig. 6.24. As a result of the interaction with an incident photon an electron with spin σ hops leaving a hole and crating a double occupancy in the intermediate high-energy state. One particle of the intermediate state hops back emitting a photon with energy of the incident photon minus $zJ\sigma$, where z is the number of exchange bonds broken, σ is the spin, and J is the exchange interaction.

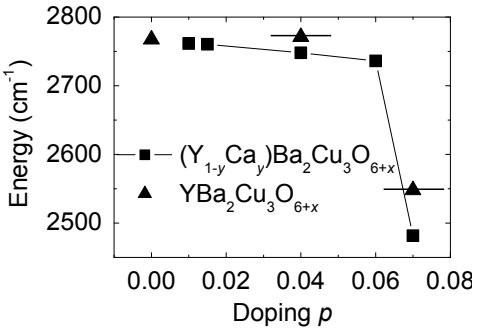

Figure 6.23: *Doping dependence of the two-magnon excitation at low temperature in* $(Y_{1-y}Ca_y)Ba_2Cu_3O_{6+x}$.

The drop of the two-magnon energy indicates a reduction of the exchange integral J by approximately 10%. The renormalization of the magnetic interaction indicates a change in the charge distribution along the principal axes at $p > p_{\mathrm{sc1}}$.

6.6.1.2 B_{1g} phonon in $(Y_{1-y}Ca_y)Ba_2Cu_3O_{6+x}$

Similar to the two-magnon excitation the B_{1g} phonon undergoes a discontinuous evolution with doping across the onset point of superconductivity. Here the energy stays practically constant (see Fig. 5.9) while the height of the phonon changes abruptly by almost a factor of 2 across p_{sc1} as shown in Fig. 6.25. In a similar fashion the width of the phonon changes abruptly and the lineshape becomes asymmetric. At first glance the shape of the phonon at $p = 0.06$ and 0.07 look similar.

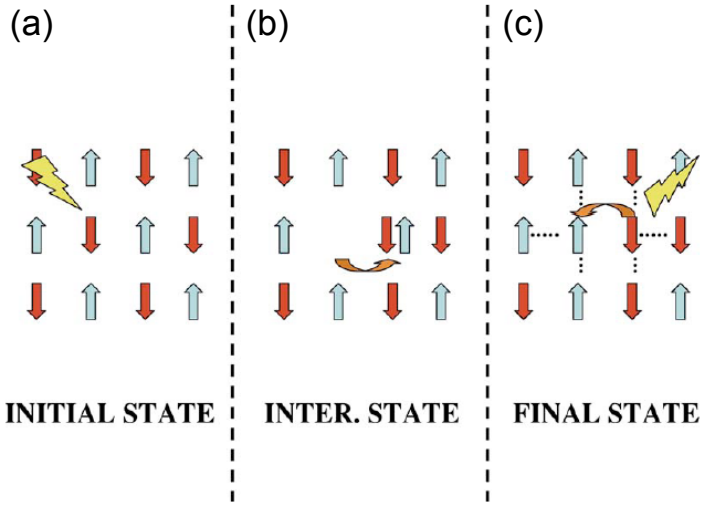

Figure 6.24: *Schematic representation of the two-magnon scattering in a 2D Heisenberg antiferromagnet. The incoming photon is absorbed by and electron with spin σ creating a double occupancy in the intermediate state (b). One particle of the doubly occupied state hops back, and a photon with energy $\hbar\omega_s = \hbar\omega_i - zJ\sigma$ is emitted, with z the number of exchange bonds broken indicated by dotted lines (c). From Ref. [34].*

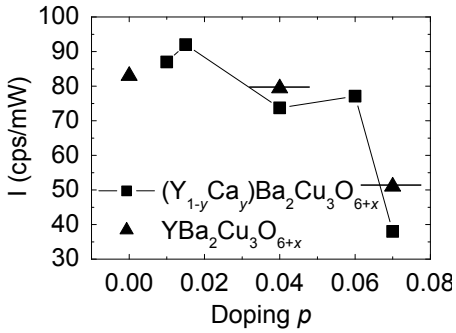

Figure 6.25: *Doping dependence of the B_{1g} phonon height at low temperature in $(Y_{1-y}Ca_y)Ba_2Cu_3O_{6+x}$.*

However, in spite of the similarity of the two spectral shapes, the physical origin of the asymmetry is different. At $p = 0.06$ the shoulder is due to inhomogeneous broadening introduced by Ca, as demonstrated by the spectrum of Fig. 5.10 where an additional peak at approximately 328 cm^{-1} is detected. The peak at lower energy corresponds to the B_{1g} phonon of the unit cells where Y is replaced by Ca. At $p = 0.07$ the sample is Ca and O co-doped (see Tab. 4.2). Neither Ca at $y = 0.08$ nor O at $x = 0.30$ lead to an inhomogeneous broadening, as shown in Fig. 5.4, meaning that here a different broadening mechanism is involved. Both the drop in height and the asymmetric profile of the phonon can be explained by the interaction of the

phonon with a continuum appearing at $p > p_{sc1}$.

6.6.2 Superconductivity

At the superconducting transition temperature spectral weight at low energy is transferred into a broad peak. The energy and the intensity of the peak depend on the symmetry (see Sect. 2.3).

Spectra in the normal and superconducting state of $La_{1.88}Sr_{0.12}CuO_4$ ($p = 0.12$) and $(Y_{0.92}Ca_{0.08})Ba_2Cu_3O_{6.30}$ ($p = 0.07$) are shown in Figs. 5.15 and 5.16, respectively. Changes at the transition temperature are not observed in

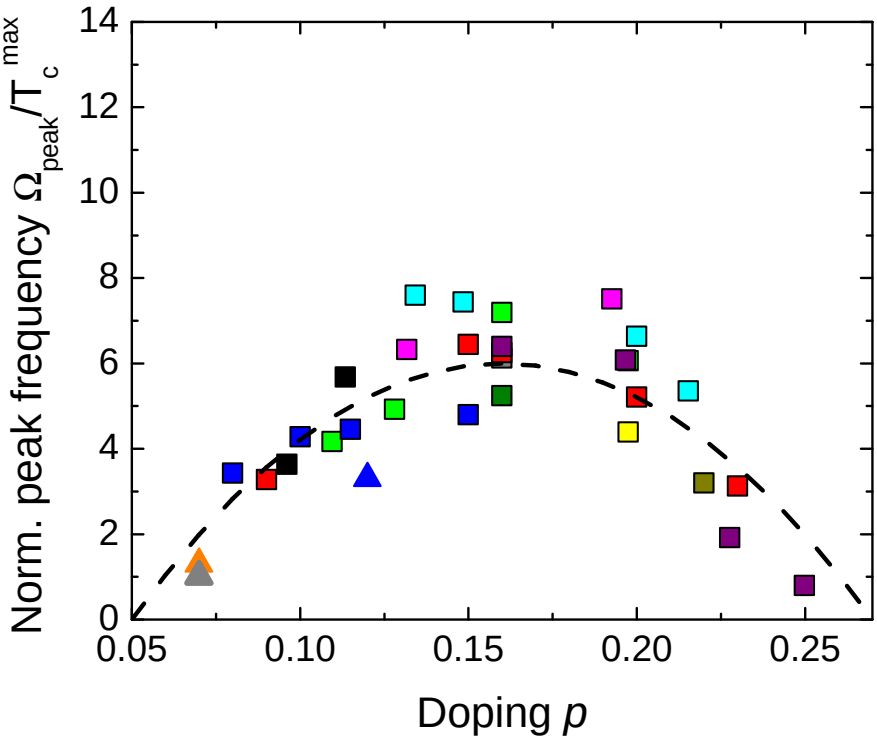

Figure 6.26: *Energy of the Raman peaks in the superconducting state. The respective references are coded as follows:* $(Y_{0.92}Ca_{0.08})Ba_2Cu_3O_{6.30}$ *(orange triangle this thesis);* $YBa_2Cu_3O_{6.40}$ *(gray triangle this thesis);* $La_{2-x}Sr_xCuO_4$ *(blue triangle this thesis and blue squares [58]);* $Bi_2Sr_2CaCu_2O_{8+\delta}$ *(red [57], green [166, 58], cyan [55], yellow [167], pink [168], [169]);* $Tl_2Ba_2CuO_{6+\delta}$ *(purple [170, 171]);* $Tl_2Ba_2Ca_2Cu_3O_{10}$ *(olive [172]);* $HgBa_2CuO_{4+\delta}$ *(black [173]). The dashed black line is the interpolation formula* $6T_c/T_c^{\mathrm{MAX}} = 6[1 - 82.6(p - 0.16)^2]$.

B_{1g} symmetry, confirming the previous results obtained in the underdoped regime. For both samples the data show superconductivity induced peaks in B_{2g} symmetry.

In Fig. 6.26 the energies of the B_{2g} peak normalized to T_c^{MAX} are plotted for $La_{1.88}Sr_{0.12}CuO_4$, $(Y_{0.92}Ca_{0.08})Ba_2Cu_3O_{6.30}$, and $YBa_2Cu_3O_{6.40}$ together with data of samples at different doping levels. The data show that the B_{2g} peak tracks T_c confirming the results of previous measurements. In particular, the B_{2g} superconducting peak was measured for the first time with Raman scattering at a doping level as low as 0.07. The B_{2g} superconducting peak scales with T_c also at this doping level close to the onset point of superconductivity.

6.6.3 Is there a relationship between charge ordering and superconductivity?

In this section a possible relationship between ordering phenomena and superconductivity is discussed. At present it is clear that static order competes with superconductivity. This is supported by the suppression of T_c of $La_{1.48}Nd_{0.4}Sr_{0.12}CuO_4$ [17, 31], $La_{1.875}Ba_{0.125}CuO_4$ [126, 127], and $La_{1.875}Ba_{0.075}Sr_{0.05}CuO_4$ [73], as well as by the complete suppression of superconductivity up to approximately $p = 0.20$ in $La_{1.8-x}Eu_{0.2}Sr_xCuO_4$ [20]. The suppression of T_c and the static order occur along with a structural transition from tetragonal to orthorhombic structure. However, a similar structural transition occurs in $La_{2-x}Sr_xCuO_4$ as well, where the strong suppression of T_c was not observed. Apparently, Nd, Ba, or Eu help to stabilize the charge and spin ordering that leads to the suppression of T_c.

While the role of static order is established, it is still an open issue whether dynamical order is favorable, irrelevant, or even compete with superconductivity. Theoretical work shows that dynamical charge order can promote superconductivity [32, 33]. Therefore, dynamical order could be an essential ingredient for high temperature superconductivity.

The measurements performed in this thesis showed a new excitation at

very low energy below the onset point of superconductivity for B_{2g} symmetry in both $La_{2-x}Sr_xCuO_4$ and $(Y_{1-y}Ca_y)Ba_2Cu_3O_{6+x}$ (see Figs. 6.6 and 6.10). In $La_{2-x}Sr_xCuO_4$ the quasi-elastic excitation changes symmetry from B_{2g} to B_{1g} upon crossing p_{sc1} (see Fig. 5.1), while in $(Y_{1-y}Ca_y)Ba_2Cu_3O_{6+x}$ it vanishes and does not reappear in B_{1g} symmetry above p_{sc1} (see Figs. 5.13 and 5.8). This indicates that in $(Y_{1-y}Ca_y)Ba_2Cu_3O_{6+x}$ the stripes do not rotate from diagonal to collateral in the same way as in $La_{2-x}Sr_xCuO_4$. Either the charge order vanishes above p_{sc1} or a different kind of order takes place. Information on the charge and spin ordering in the "high-T_c" compounds with T_c of the order of 100 K is not available at present below $p \approx 0.10$. Neutron scattering data on $YBa_2Cu_3O_{6.85}$ and $YBa_2Cu_3O_{6.6}$ show the two-dimensional character of the spin excitations [174], in contrast to $La_{2-x}Sr_xCuO_4$ at similar doping levels where the spin excitations appear to be one-dimensional [143]. The

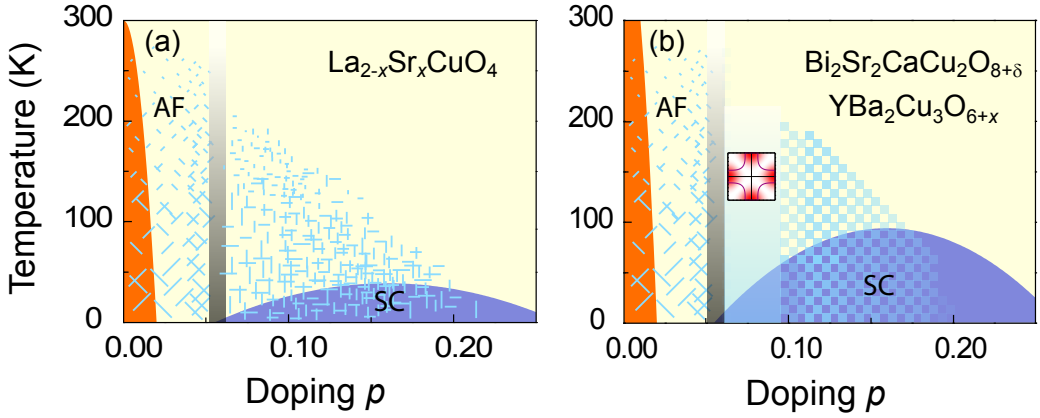

Figure 6.27: *Phase diagrams for "low" (a) and "high"-T_c (b) cuprates as derived from earlier [146] and present Raman data and from neutron scattering [174, 144, 175, 176] and scanning tunneling microscopy [76, 177] measurements. The position of the onset point of superconductivity p_{sc1} depends on the degree of disorder with the minimum at approximately 0.05 for clean materials [40]. The different line lengths qualitatively indicate doping and temperature ranges, density, orientation, and correlation lengths of stripes. The square pattern symbolizes checkerboard order which, however, is only established for $p > 0.10$. For $p_{sc1} < p < 0.10$, there are indications from the Raman results presented here for an interaction with structure in momentum space as sketched.*

Raman scattering data do not provide direct information on the ordering above the onset point of superconductivity since an ordering related peak was not observed. However, the strong renormalizations of the two-magnon excitation and of the B_{1g} phonon indicate that an excitation compatible with B_{1g} symmetry sets in above p_{sc1}.

Putting together the various pieces of information obtained from Raman and neutron scattering a new phase diagram for "high" and "low-T_c" cuprates is proposed in Fig. 6.27. Below the onset point of superconductivity diagonal stripes are a universal feature of all oxide superconductors. Above p_{sc1} the "low-T_c" $La_{2-x}Sr_xCuO_4$ shows evidence of one-dimensional stripes along the $Cu-O$ bond directions while in the "high-T_c" compounds like $(Y_{1-y}Ca_y)Ba_2Cu_3O_{6+x}$ the order appears to be more two-dimensional.

The new information obtained in this thesis clarify the relationship between dynamical charge and spin ordering and superconductivity. Diagonal order competes with superconductivity and, apparently, the two phenomena are mutually exclusive. Fluctuating order along the $Cu-O$ bonds direction leads to superconductivity with "low-T_c" (order 40 K as for $La_{2-x}Sr_xCuO_4$), and two-dimensional or checkerboard order leads to superconductivity with "high-T_c" (order 100 K as for $(Y_{1-y}Ca_y)Ba_2Cu_3O_{6+x}$).

Appendix A

Raman scattering at high pressure

Studies at elevated pressure have a great potential to better understand states of matter and transitions between them. Materials eventually become superconductors at high pressure [178]. A few examples relevant to the cuprates are the dependence of the exchange coupling J or the lattice constant [179] or of the doping p [180] or of the B_{1g} spectrum below T_c [181] on pressure. Raman measurements performed on $YBa_2Cu_3O_{6.95}$ at high pressure showed that the B_{1g} peak appearing in the superconducting state and T_c move downwards upon pressure [181]. In $La_{1.8-x}Eu_{0.2}Sr_xCuO_4$ the static spin and charge modulation (static charge and spin stripes) quenched superconductivity up to high doping ($p \approx 0.20$) [20]. Applying pressure the static order is destroyed and the superconducting phase is restored [36]. Therefore, experiments at high pressure are particularly interesting to study charge and spin ordering phenomena and superconductivity in cuprates.

In the course of this thesis a new setup for Raman spectroscopy at high pressure was designed, built up, and tested. With the new setup the parameter space is increased and now the pressure dependence of the Raman response can be studied.

A.1 High pressure technique

A.1.1 Introduction

Measurements at high pressure became possible with the development of the diamond anvil cell (DAC) [182]. A DAC consists essentially of two cone-shaped anvils attached to stationary and movable parts of the cell, as sketched in Fig. A.1. The culets (the point on the bottom of a diamond's pavilion) of the anvils point against each other and are pressed into a gasket (see Fig. A.2). Alignment between the two bodies of the cell is usually maintained by pins that are attached to the stationary part of the cell and slide in the holes in the piston or, simpler, by a piston-cylinder assembly.

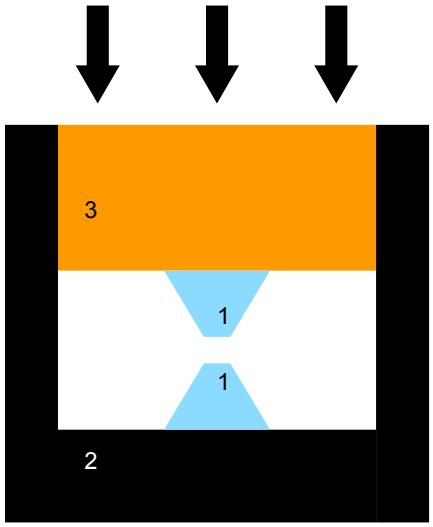

Figure A.1: *Sketch of a diamond anvil cell (DAC). 1 are the anvils, and 2 and 3 the stationary part and the movable piston, respectively.*

High pressures are generated by applying a relatively small force to the large area of the piston. The force is transmitted to the small area of the culets of the anvils. The gasket, with a typical thickness of approximately 200 μm is first indented applying pressure with the anvils in order to produce two cones. In the middle of the indent a hole is drilled (Fig. A.2 (a)) which is the sample chamber. The sample is placed into the hole along with a transmission medium (Fig. A.2 (b)). Hydrostatic conditions of high pressure are best realized with the noble gases Ar and He. At low and moderate pressure mixture of ethanol and methanol or kerosine are used succesfully.

The two anvils are usually brilliant-cut diamonds selected from gem stones. The culet is polished in order to get a flat surface parallel to the

larger surface usually referred to as the table. A typical size for an anvil is around 1/4 carat, with the diameter of the table and the culet approximately 4 and 0.5 mm, respectively. Diamond is selected since it is the hardest known material, and allows one to reach the highest pressures, and since it is transparent in a wide frequency range including infrared and visible light and X-rays.

However, not only diamond anvils are used. Sapphire and tungensten-carbide anvils are also commonly used, and recently also synthetic single crystals of SiC, commonly referred to as Moissanite, have been used in experiments [183].

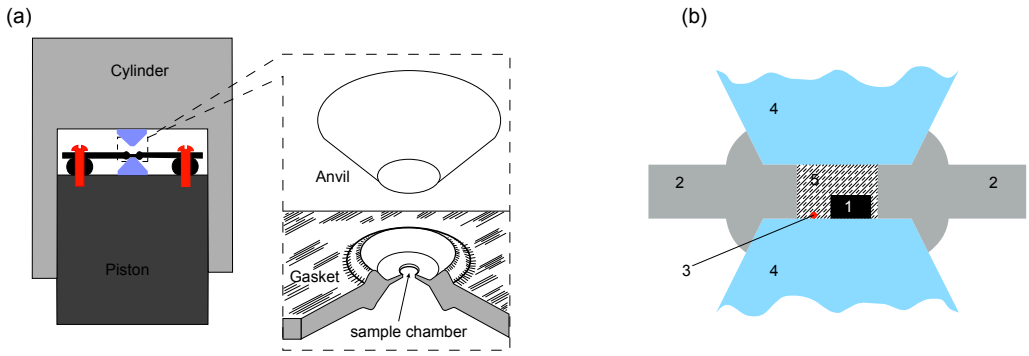

Figure A.2: *(a) Details of the diamond anvil region of a DAC. (b) Sample in the pressure cell. The sample (1) is placed between the anvils (4) together with a small piece of ruby (3) used to measure the pressure (see Sect. A.1.4). Sample and ruby are immersed in a transmission medium (5) and the lateral confinement is ensured by a metallic gasket (2).*

A.1.2 The High Pressure Cell

The pressure cell designed in this work has the goal to perform experiments up to approximately 30 GPa, in a magnetic field of 8 T, and in the temperature range $1.5 \leq T \leq 350$ K. For the body of the cell copper-beryllium was selected since is non-ferromagnetic and has excellent mechanical strength. A sketch of the high pressure cell is shown in Fig. A.3. The body of the cell has two cylindrical parts, (1) and (2) with different lengths. The disk (1)

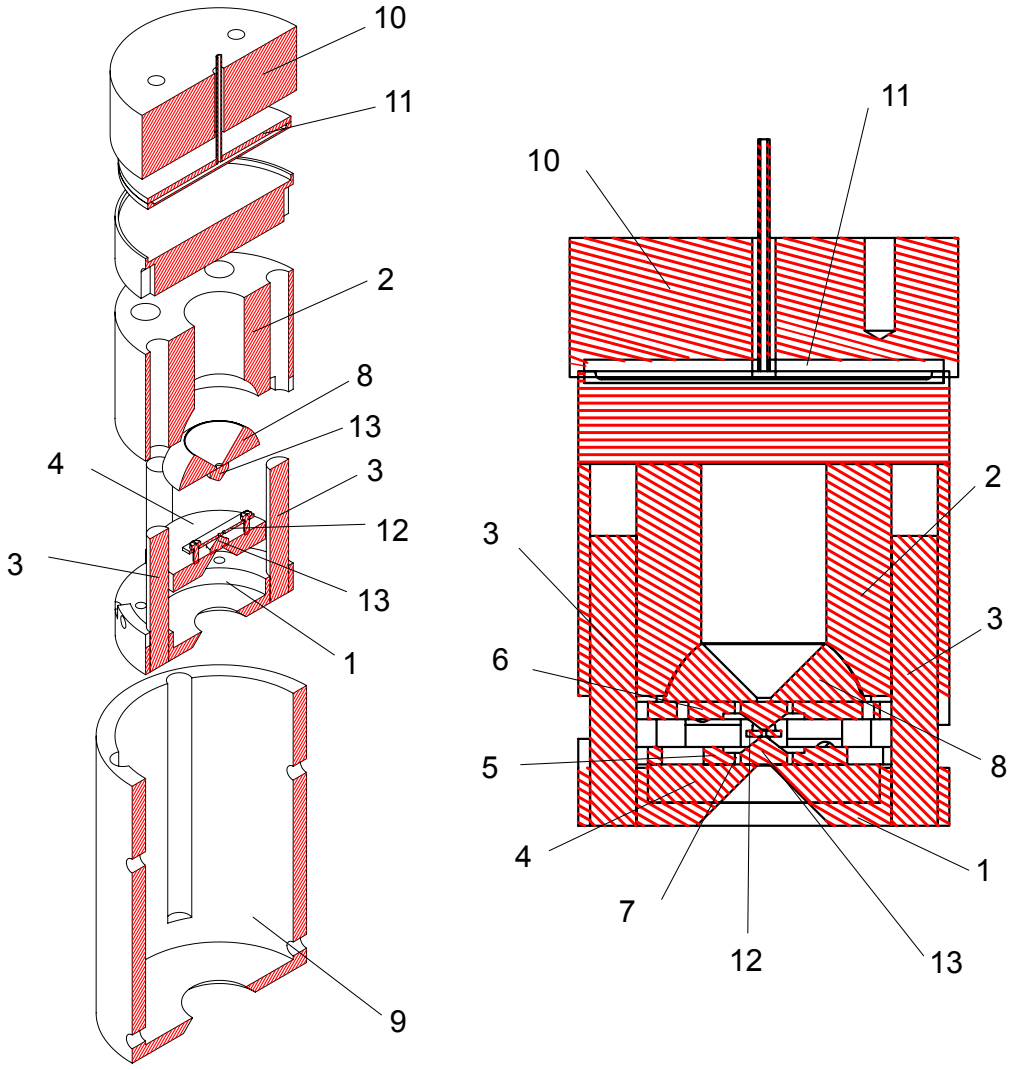

Figure A.3: *Sketch of the high pressure cell. 1 Base disk with four pins; 2 Piston with the holes for the pins; 3 pins; 4 tungsten-carbide disk supporting the lower anvil; 5 and 6 copper-beryllium disks used as holders for the anvils; 7 copper ring used to attach the anvils to the anvil-holder; 8 tungsten-carbide hemisphere supporting the upper anvil; 9 copper-beryllium container; 10 copper-beryllium screw used to clamp the cell in the container; 11 Stainless steel membrane operated with He gas; 12 gasket; 13 anvils.*

is equipped with four pins (3) which slide through the holes in the cylinder (2). The cell is designed to perform Raman measurements in back-scattering configuration. The disk (1) is on the spectrometer side and its length is chosen in order to place the sample at the proper height in the cryostat.

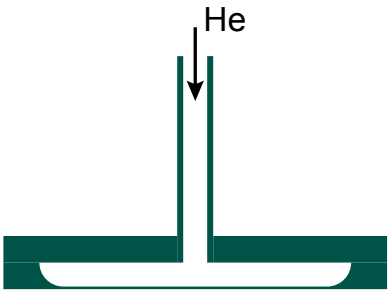

Figure A.4: *Scheme of the helium membrane used to apply pressure to the cell. Helium gas at moderate high pressure is introduced into the membrane via the capillary and produces a deformation of the thin side of the membrane.*

The disk (1) has a concentric seat for a smaller tungsten-carbide disk (4). Tungsten-carbide is an exceptionally hard material which tolerates, without appreciable deformations, the relatively high pressure generated by the base (table) of the anvil. A hole in the middle of the tungsten-carbide cylinder allows optical access to the sample. On the spectrometer side side the hole in the tungsten-carbide disk has a cone profile with an angle of 60 degrees. The holders of the anvils are copper-beryllium disks (5) and (6), and the anvils is attached to them with a copper ring (7). The disk (5) can translate in x and y direction to properly align the anvil with respect to the hole.

The cylinder (2) has a seat for a tungsten-carbide hemisphere (8). The hemisphere allows the tilting of the anvil with respect to the axis of the body of the cell, and this degree of freedom is used to align the anvils parallel to each other. The cell is placed inside a copper-beryllium container (9) which is closed by a screw (10). In this way the cell is clamped, and the anvils will be pressed against each other by the piston when pressure is applied to the membran. The membrane, schematically shown in Fig. A.4, is made of one 3 mm thick disk and a second disk processed in order to obtain a thin (approximately 300 μm) central part. The two disks are welded together laterally. The membrane is filled with helium up to a pressure of typically 100 bar through a capillary.

A.1.3 Experimental details

To properly plane an experiment the pressure range must be known. Then the material for the anvil and for the gasket can be selected. In this work CuBe was chosen for the gasket. The hole in the middle of the indent is realized with a spark erosion system built up for this work. Holes with diameters 100, 150, 200, 300, and 500 μm can be realized. In the measurements performed in this work diameters of 300 and 500 μm were used. The size of the samples studied was of the order of 100x100 μm. In order to handle crystals of a such small size a micro-manipulator consisting of a metallic capillary with a nozzle diameter of approximately 30 μm, an xy translational stage, and a binocular optical system, was used. When the capillary is punped with a membrane pump small samples stick to the capillary and can be placed into the desired position. In addition, a small piece of ruby is putted in the hole with the sample for determining the pressure (see Sect. A.1.4).

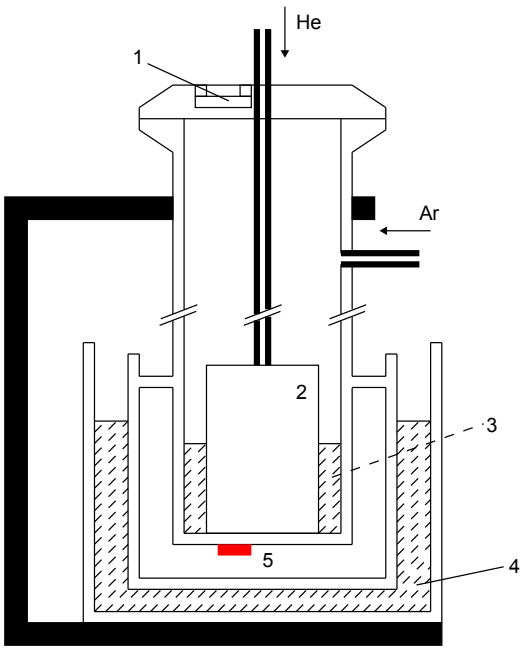

Figure A.5: *Sketch of the argon loading system. 1 quartz windows; 2 pressure cell; 3 liquid argon; 4 liquid nitrogen, 5 temperature sensor.*

Ar was selected as transmission medium since it ensures excellent hydrostatic conditions and since it can be liquefied at liquid nitrogen temperature. In order to fill the hole with argon the cell with the sample properly placed into the hole of the gasket is placed in a vacuum chamber with the anvils almost in contact with the gasket but not tightly closed. The vacuum chamber is first evacuated, then filled with Ar at ambient pressure and cooled down to approximately 90 K right below the boiling point of the Ar (Fig. A.5). When the level of the liquid Ar is above the gasket position the cell can be closed by applying pressure to the membrane.

A.1.4 Determination of the pressure

The pressure in the sample volume was determined via the ruby (Al_2O_3 with Cr^{3+} impurities) fluorescence. When excited the ruby emits two fluorescence bands, R_1 and R_2 at 694.28 and 692.7 nm, respectively, at ambient pressure and temperature (Fig. A.6). The wavelength of the two bands increases with pressure. The pressure dependence was calibrated by several groups using the equation of state of simple compounds such as sodium chlorine [184] or metals such as copper, gold etc. [185].

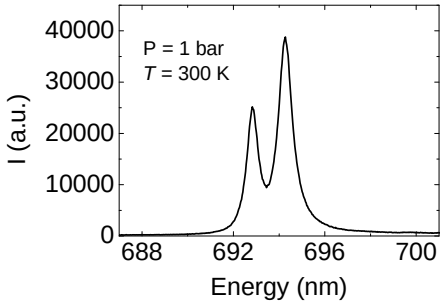

Figure A.6: *Double fluorescence peak of the ruby at ambient pressure and temperature.*

The frequency of the ruby emission depends also on temperature, and the pressure and temperature dependences are assumed to be independent. The temperature contribution to the frequency of the ruby fluorescence has been calibrated at zero pressure by several groups [186, 187, 188]. The two contributions are combined in a single relation that defines a practical scale for the pressure. Commonly the R_1 peak is used to determine the pressure.

In this work the pressure and temperature calibrations of Ref. [185] and

[189], respectively, are used leading to the relation

$$P(\lambda_{\mathrm{R}_1}) = \frac{1904}{7.665} \cdot \left[\left(\frac{\lambda_{\mathrm{R}_1}(P,T) - \Delta\lambda_{\mathrm{R}_1}(T)}{\lambda_{\mathrm{R}_1}(0,T_0)} \right)^{7.665} - 1 \right], \qquad \text{(A.1)}$$

where $\lambda_{R_1}(P,T)$ and $\Delta\lambda_{\mathrm{R}_1}(T)$ are the position of the R_1 line at pressure P and temperature T and the pressure-independent temperature contribution of the position, respectively, and $\lambda_{\mathrm{R}_1}(0,T_0)$ is the position of the R_1 line at zero pressure and room temperature. $\Delta\lambda_{\mathrm{R}_1}(T)$ is approximated by a polynomial up to 3^{rd} order,

$$\Delta\lambda_{R_1}(T) = C_1 \cdot (T - T_0) + C_2 \cdot (T - T_0)^2 + C_3 \cdot (T - T_0)^3 \qquad \text{(A.2)}$$

with $T_0 = 300$ K, $C_1 = 6.554 \cdot 10^{-3}$ nm/K, $C_2 = 8.670 \cdot 10^{-6}$ nm/K^2, $C_3 = 1.099 \cdot 10^{-8}$ nm/K^3.

A.2 Setup for Raman experiment at high pressure

The optical setup for a Raman experiment at high pressure is schematically shown in Fig. A.7. The light source is a commercial Kr^+ ion laser (Coherent Innova 400). Several lines are available, and the measurements were been performed using the lines at 530, 647 nm.

A first spatial filter composed of a microscope objective lens (Spindler and Hoyer, x10)(O1), a pin-hole with diameter 20 μm (S2) and a second objective lens (L1) is used. As a result the radiation propagating in different directions with respect to the laser light is blocked. A spectral filtering is achieved by the prism monochromator (PMC) that together with an adjustable slit (S2) between two achromatic lenses both with $f = 100$ mm (L1 and L2) allow the rejection of lines which differ from the laser line by more than 30 cm^{-1}.

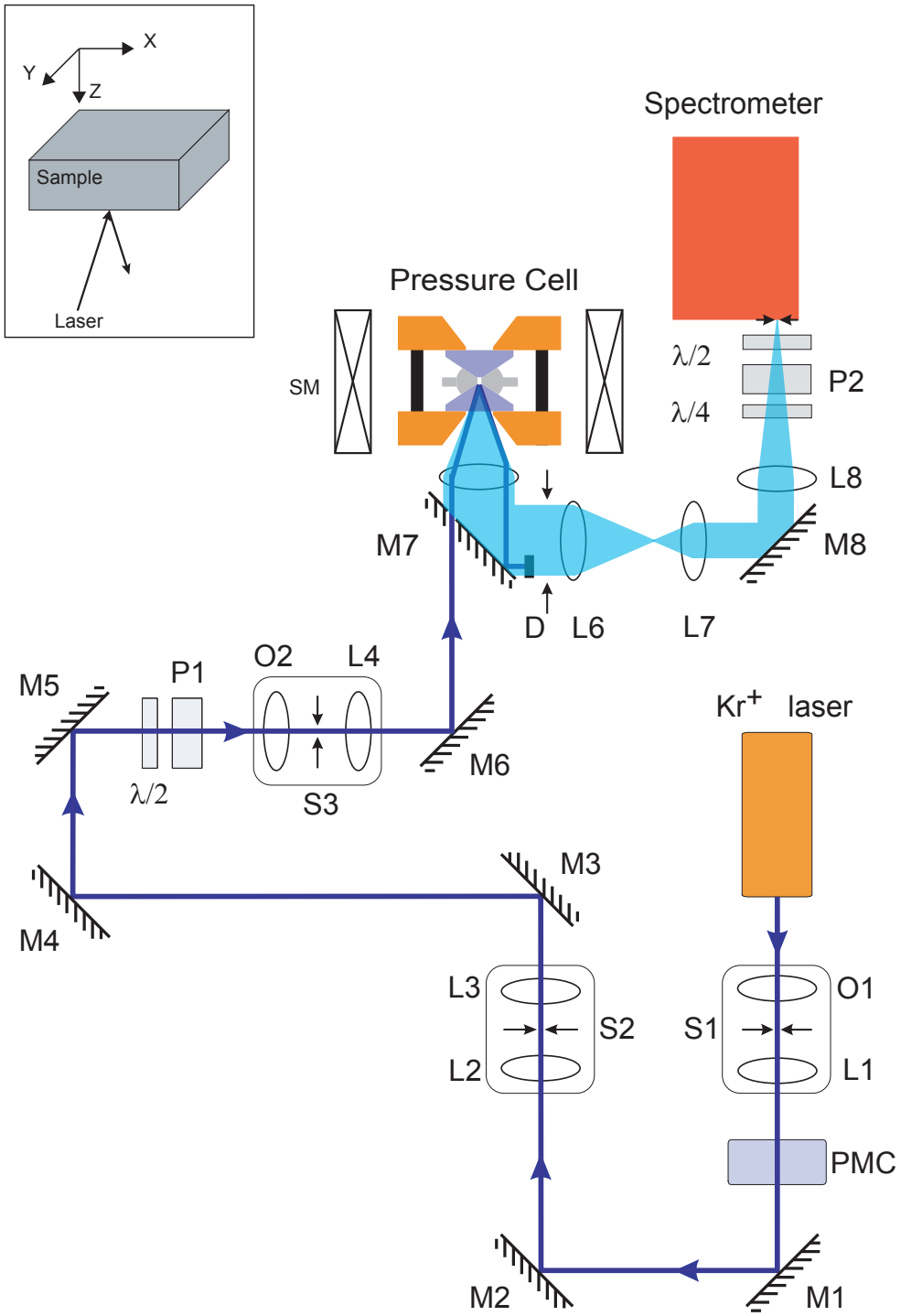

Figure A.7: *Scheme of the experimental setup for Raman scattering at high pressure. L1-L8 achromatic lenses; S1-S3 pin-holes or slits; PMC prism-monochromator; M1-M8 mirrors; P1-P2 polarizers; O1-O2 objectives; D diaphragm ; SM superconductive magnet. Inset, detail of the sample orientation.*

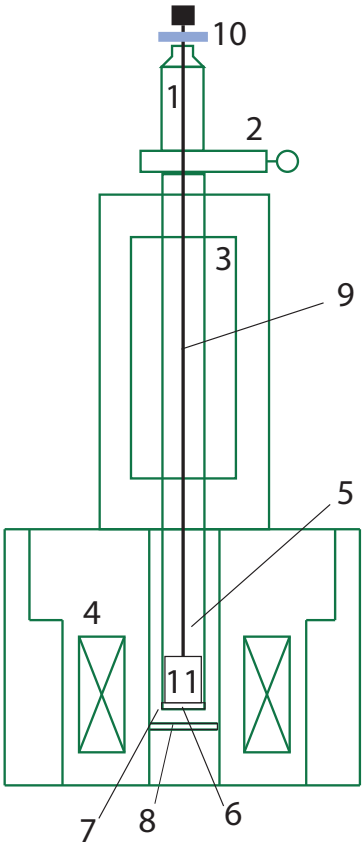

Figure A.8: *Scheme of the cryostat for high pressure Raman spectroscopy. 1 Loading chamber; 2 lock valve; 3 helium tank; 4 superconducting magnet; 5 cold chamber; 6 quartz window; 7 Insulating vacuum chamber; 8 glass window; 9 holder of the pressure cell; 10 rotational device for the pressure cell; 11 pressure cell.*

With a Glan-Thompson polarizer (P1) linearly polarized light is prepared. The $\lambda/2$-retardation plate before the polarizer rotates the polarization of the laser light and allows the adjustment of the power incident on the sample.

An additional spatial filter, consisting of a microscope objective lens (Spindler and Hoyer, x5) (O2), a pin-hole with diameter 30 μm (S3) and an achromatic lens with focal length $f = 30$ mm (L4), is finally used to obtain an homogeneous Gaussian beam. An additional lens (L5) with focal length $f = 60$ focuses the light on the surface of the sample. The laser goes through the edge of the lens in order to keep the reflected light away from the optical axis.

The scattered light is collected by the same objective lens used to focus the incident light. Two achromatic lenses (L6, L7) are used to reduce the diameter of the scattered beam, and a last lens (L8) focuses the scattered light on the entrance slit of the spectrometer. A second Glan-Thompson polarizer (P2) and a $\lambda/4$-retardation plate allow the selection of the desired polarization states of the scattered light. A $\lambda/2$-retardation plate placed after the polarizer allows the rotation of the linearly polarized light into the direction of maximal transmission of the spectrometer. For the analysis of the scattered light a commercial triple monochromator (Jobin Yvon T64000) is used. The

first and second stages are symmetric and subtractively coupled and select an energy band of typically 100 meV which is dispersed by the third stage. The spectrum is recorded by a CCD chip cooled by liquid nitrogen down to $-140°$ C. The intensity of the spectra is given in units of photon counts for seconds (cps) normalized to the power absorbed by the sample.

The high pressure cell can be placed in a helium flow cryostat equipped with a superconducting magnet (not realized yet). The scheme of the cryostat is plotted in Fig. A.8. In the lower part of the cryostat there is the superconducting magnet (4) with a window at the bottom (8) for optical access to a vacuum chamber (7). Inside the vacuum chamber there is a second chamber (5) equipped with a quartz windows (6) for optical access where the cell is placed. The temperature can be adjusted in the range $1.5 < T < 350$ K by the He flow and an electrical heather. The pressure cell is in gaseous or liquid He. The pressure cell is attached to a holder (9), which facilitates rotations with a precision to better than half a degree (10).

A.3 Raman spectra at high pressure

Raman measurements at high pressure and room temperature were performed on $(Y_{0.98}Ca_{0.02})Ba_2Cu_3O_{6.05}$ single crystals. The purpose of the measurements was the test of the high pressure setup with particular attention to the pressure cell, the pressure adjustment and determination, and the intensity of the Raman signal. Spectra at different pressures are shown in Fig. A.9. Measurements were preformed in xx polarization (see inset of Fig. A.7) with the 530.8 nm excitation line. The peaks at approximately 140 and 340 cm^{-1} correspond to the A_{1g} and B_{1g} phonons, respectively, while the other excitations are contributions coming from the sapphire anvil. The energy of both phonons increases monotonically with pressure. The peak positions for the A_{1g} and B_{1g} phonons are plotted in Fig. A.10 (a) and (b), respectively. The data demonstrate the excellent performance of the high pressure setup concerning the signal intensity and the operation of the pressure cell. With this

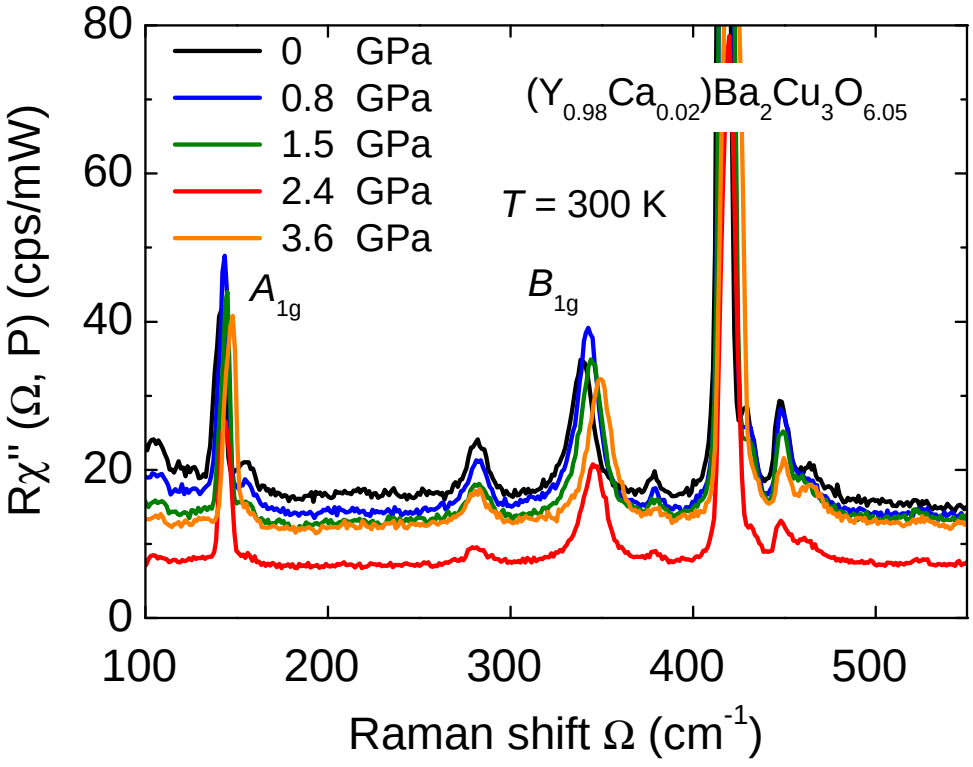

Figure A.9: *Raman spectra of* $(Y_{1.98}Ca_{0.02})Ba_2Cu_3O_{6.05}$ *at room temperature and different pressures as indicated in the figure. The measurements have been performed in xx polarization (see inset of Fig. A.7).*

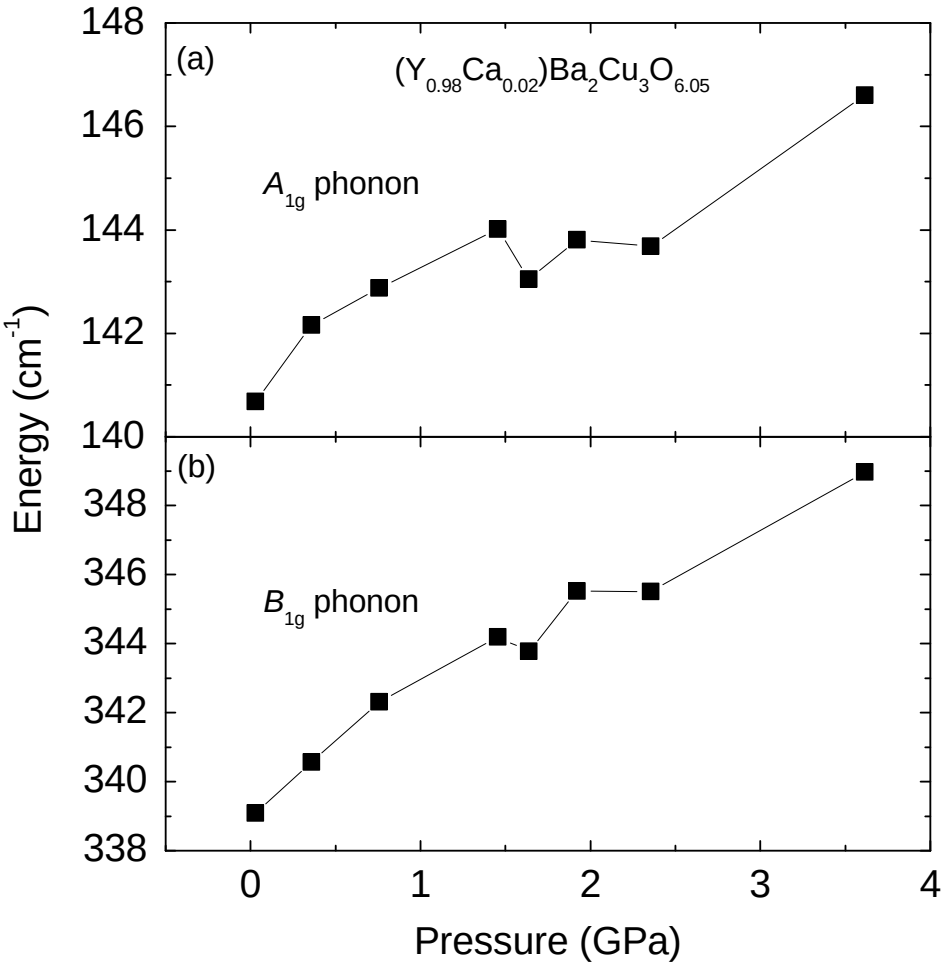

Figure A.10: *Pressure dependence of the energy of A_{1g} (a) and B_{1g} (b) phonons at room temperature.*

equipment measurements with pressure steps smaller than 0.1 GPa can be performed.

In Fig. A.11 (a) spectra of $(Y_{1.98}Ca_{0.02})Ba_2Cu_3O_{6.05}$ measured in xx and xy polarization, acquired with the optical configuration described in sect. A.2, are shown. In the spectrum measured in xy polarization the A_{1g} and B_{1g} phonons are still relatively strong though being forbidden (see Sect. 3.4). The reason is a strong birefringence in the anvils induced by mechanical stress. Spectra in xx and xy polarization, measured with a slightly different optical configuration, with the laser beam propagating along the optical axis and a reduced aperture for the scattered light are shown Fig. A.11 (b). Here the data show a much stronger suppression of the A_{1g} and B_{1g} phonons in xy polarization, indicating that the polarization state of incoming and scattered light is practically preserved and the desired polarization configuration can be selected at the price of a reduced Raman intensity.

Summarizing, a setup for Raman spectroscopy at high pressure is now established. Raman measurements up to 3.6 GPa can be performed. With some limitations measurements with defined polarization states of incoming and outgoing light are possible. The cell is designed in a way that it can be inserted into a magnetic field.

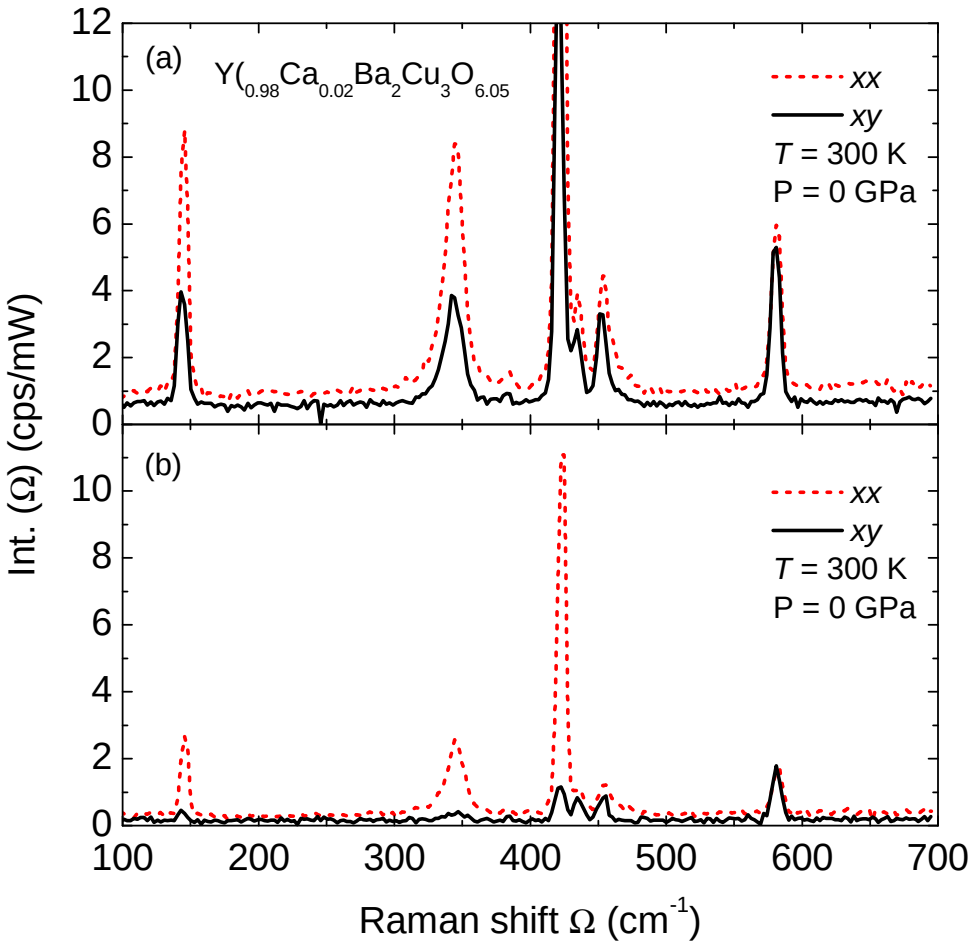

Figure A.11: *Raman spectra of* $(Y_{1.98}Ca_{0.02})Ba_2Cu_3O_{6.05}$ *at room temperature for xx and xy polarizations (see inset of Fig. A.7). Panel (a), incoming laser propagating out of the optical axis, and full aperture for the scattered light; (b) incoming laser propagating on the optical axis and 14 mm aperture of the diaphragm on the scattered light path (see Fig. A.7).*

Summary

In this thesis electronic properties of two prototypical copper-oxygen superconductors were studied with Raman scattering as a function of polarization, incident photon energy, temperature and doping. The emphasis was put on the doping range $0 \leq p \leq 0.07$ holes per CuO_2 formula unit including the onset point of superconductivity p_{sc1}.

Below p_{sc1} new excitations in the range up to 200 cm^{-1} were found in the B_{2g} (xy) Raman spectra of both $La_{2-x}Sr_xCuO_4$ and $(Y_{1-y}Ca_y)Ba_2Cu_3O_{6+x}$. Independent of the cuprate family and the doping level they show similar energies, spectral shapes, and temperature dependences indicating a common underlying physical mechanism.

In $La_{2-x}Sr_xCuO_4$ the excitation observed in B_{2g} symmetry disappears close to p_{sc1} but reappears in B_{1g} symmetry above p_{sc1}. This symmetry flip occurs along with the rotation of the spin superstructure by 45° as observed by inelastic neutron scattering. The correspondence between the orientation and the symmetry demonstrates that the low-energy excitations are a signature of the spin-charge superstructure usually referred to as stripes. In $(Y_{1-y}Ca_y)Ba_2Cu_3O_{6+x}$ the quasielastic peak also disappears upon crossing p_{sc1} but does not reappear at any symmetry. However, the energy of two-magnon excitation and the peak intensity of the B_{1g} buckling phonon change discontinuously at p_{sc1} by 8 and 50%, respectively. These renormalization effects demonstrate indirectly that a very strong interaction being peaked close to the Brillouin zone boundary at the M points becomes effective at $p > p_{\mathrm{sc1}}$. The structure in momentum space is compatible with $|d_{x^2-y^2}|$ sym-

metry and, hence, with the magnetic structure of the CuO_2 plane found by neutron scattering for $p > 0.10$ and with the superconducting gap.

The excitations have a finite energy indicating, in accordance with the neutron scattering results, the dynamical nature of the stripes. The peak energies depend linearly on temperature above a saturation range governed by doping. This type of behaviour is typical for a system close to a quantum critical point (QCP) with the excitations reflecting the fluctuations. Therefore the experimental data were compared with predictions of a theoretical model for the Raman response of incipient fluctuating charge order. The agreement is remarkable and demonstrates not only the importance of charge ordering but provides further support to the interpretation of the Raman data.

Although a gap is usually expected only with static order, partial suppression of the electronic density of states can be expected also along with fluctuating order and is indeed observed in the B_{2g} Raman spectra. Here, this pseudogap is found below p_{sc1} in both compounds studied corroborating the intimate relation to ordering. Moreover, a spectral weight suppression of at least 30% is observed below the transition to static order in $(La_{1.875}Ba_{0.075}Sr_{0.05})CuO_4$. In $(Y_{1-y}Ca_y)Ba_2Cu_3O_{6+x}$ the energy range of the pseudogap grows slightly in the range $0 < p < p_{\mathrm{sc1}}$ and increases discontinuously by at least 50% upon crossing p_{sc1}. The energy range is much larger than that of the superconducting gap which was not formerly observed by Raman scattering at a doping level as low as $p = 0.07$.

In conclusion, a hierarchy of the interrelation between ordering and superconductivity can be established. Generally, static or fluctuating diagonal order manifesting itself as low-energy modes in the B_{2g} Raman spectra below p_{sc1} is incompatible with superconductivity. Above p_{sc1} the type of order seems to determine the maximal transition temperature. As known before, static order aligned along the principal axes suppresses superconductivity as well. According to the results presented here the suppression of T_c in $La_{1.875}Ba_{0.075}Sr_{0.05}CuO_4$ at 1/8 filling can be traced back to the reduction of the superfluid density via the reduction of the density states. Fluctuating

quasi one-dimensional stripes are also reducing the maximal transition temperature in compounds such as $(La_{2-x}Sr_x)CuO_4$. If the order becomes more two-dimensional such as in $(Y_{1-y}Ca_y)Ba_2Cu_3O_{6+x}$ T_c^{MAX} may reach 100 K or more. It remains to be clarified to which extent the fluctuations themselves can support Cooper pairing.

In order to further study the interrelation of ordering and superconductivity a new setup for Raman spectroscopy at high pressure was designed and built up in the course of this work. Test measurements were successfully performed in the pressure range up to 3.6 GPa.

Zusammenfassung

In vorliegender Arbeit werden elektronische Eigenschaften zweier prototypischer Kupferoxyd-Supraleiter als Funktion der Polarisation, der Energie der einfallenden Photonen, der Temperatur und der Dotierung mittels Raman Streuung untersucht. Im Wesentlichen wurde der Dotierungsbereich von $0 \leq p \leq 0.07$ Löcher pro CuO_2 Formel Einheit studiert, in welchem auch der Einsatzpunkt der Supraleitung p_{sc1} liegt.

Bei Dotierungen unterhalb von p_{sc1} wurden in B_{2g} (xy) Symmetrie sowohl in $La_{2-x}Sr_xCuO_4$, als auch in $(Y_{1-y}Ca_y)Ba_2Cu_3O_{6+x}$, neue Anregungen in einem Bereich bis zu 200 cm^{-1} gefunden. Unabhängig von der Materialklasse und des Dotierungsgrades zeigen diese Anregungen ähnliche Energien, spektrale Verläufe und Temperaturabhängigkeiten. Es ist deshalb naheliegend, dass ein gemeinsamer Mechanismus zugrundeliegt.

In $La_{2-x}Sr_xCuO_4$ verschwindet die Anregung in B_{2g} Symmetrie nahe p_{sc1}, erscheint aber wieder in B_{1g} Symmetrie oberhalb von p_{sc1}. Dieser Wechsel der Symmetrie findet gleichzeitig mit einer Rotation der Spin-Überstruktur um 45° statt, die mittels inelastischer Neutronenstreuung nachgewiesen wurde. Dieser Zusammenhang zwischen Orientierung der Überstruktur und der Symmetrieabhängigkeit in den Raman-Streuexperimenten zeigt, dass die niederenergetischen Anregungen eine Signatur der Spin-Ladungs-Überstruktur sind, die üblicherweise als Streifen bezeichnet werden. In $(Y_{1-y}Ca_y)Ba_2Cu_3O_{6+x}$ verschwindet der quasielastische B_{2g} Peak ebenfalls beim Überschreiten von p_{sc1}, erscheint aber in keiner Symmetrie wieder. Allerdings ändern sich die Energie der Zwei-Magnonen-Anregung und die Intensität des B_{1g}- Phonons

diskontinuierlich um 8 bzw. 50%. Diese Renormalisierungseffekte zeigen indirekt, dass für $p > p_{\mathrm{sc1}}$ eine sehr starke Wechselwirkung einsetzt, die nahe der Brillouin-Zonengrenze an den M Symmetriepunkten ein Maximum hat. Die Struktur im Impulsraum ist kompatibel mit der $|d_{x^2-y^2}|$ Symmetrie und demzufolge mit der magnetischen Ordnung in den zwei-dimensionalen CuO_2-Ebenen, die in Neutronenstreuexperimenten für $p > 0.10$ gefunden wurde, und mit der Energielücke im Suprazustand.

Die Anregungen haben eine endliche Energie, die in Übereinstimmung mit den Ergebnissen aus Neutronenstreuexperimenten die dynamische Natur der Streifen verdeutlicht. Oberhalb eines dotierungsabhängigen Sättigungsbereichs variieren die Peak-Energien linear mit der Temperatur. Dieses Verhalten ist typisch für ein System nahe eines quantenkritischen Punktes (QKP), wobei die Anregungen die Fluktuationen widerspiegeln. Deshalb wurden die experimentellen Daten mit den Vorhersagen eines theoretischen Models für den Raman Response fluktuierender Ladungsordnung verglichen. Die Übereinstimmung ist bemerkenswert gut und zeigt nicht nur die Bedeutung der Ladungsordnung, sondern liefert auch weitere Unterstützung für die Interpretation der Raman Daten.

Obwohl normalerweise eine Lücke im elektronischen Spektrum nur zusammen mit statischer Ordnung erwartet wird, kann eine partielle Unterdrückung der elektronischen Zustandsdichte auch zusammen mit einer fluktuierenden Ordnung erwartet werden und wird in der Tat in den B_{2g} Raman Spektren gefunden. Diese Pseudolücke wird in den vorliegenden Daten für Dotierungen $p < p_{\mathrm{sc1}}$ in beiden untersuchten Materialsystemen gefunden, was die enge Beziehung zur Ordnung bekräftigt. Darüber hinaus wird eine Reduktion des spektralen Gewichts um mindestens 30% unterhalb des Übergangs zu statischer Ordnung in $La_{1.875}Ba_{0.075}Sr_{0.05}CuO_4$ nachgewiesen. In $(Y_{1-y}Ca_y)Ba_2Cu_3O_{6+x}$ wächst der Energiebereich der Pseudolücke leicht im Bereich $0 < p < p_{\mathrm{sc1}}$ und nimmt diskontinuierlich um mindestens 50% zu, wenn er p_{sc1} überschreitet. Der Energiebereich ist viel größer als derjenige der Energielücke im Suprazustand, was mittels Raman-Streuung noch nie bei

einer so kleinen Dotierung ($p = 0.07$) nachgewiesen werden konnte.

Zusammenfassend kann eine Rangfolge der Wechselbeziehung zwischen Ordnung und Supraleitung etabliert werden. Statische oder fluktuierende diagonale Ordnung, die sich für $p < p_{\mathrm{sc1}}$ in niederenergetischen Moden in den B_{2g} Spektren manifestiert, ist inkompatibel mit der Supraleitung. Oberhalb von p_{sc1} scheint die Art der Ordnung die maximale Übergangstemperatur festzulegen. Bekanntlich unterdrückt statische, parallel zu den Kristallachsen orientierte Ordnung die Supraleitung. Die hier gezeigten Ergebnisse belegen, dass die Unterdrückung von T_c in $La_{1.875}Ba_{0.075}Sr_{0.05}CuO_4$ bei 1/8 Bandfüllung, über das Absenken der Zustandsdichte, zur Erniedrigung der suprafluiden Dichte zurückverfolgt werden. Auch fluktuierende quasieindimensionale Streifen reduzieren die maximale Übergangstemperatur in Verbindungen wie $La_{2-x}Sr_xCuO_4$. Sobald die Ordnung einen stärker zweidimensionalen Charakter bekommt, wie z.B. in $(Y_{1-y}Ca_y)Ba_2Cu_3O_{6+x}$, sind Sprungtemperaturen von $T_c^{\mathrm{MAX}} = 100$ K möglich. Dagegen muss noch geklärt werden, ob und zu welchem Grad die Fluktuationen selbst die Bildung von Copper-Paaren fördern.

Im Zuge dieser Arbeit wurde ein neuer Versuchsaufbau für Raman-Messungen bei hohen Drücken entworfen und aufgebaut, um weitergehende Experimente zur Wechselbeziehung von Spin-Ladungsordnung und Supraleitung zu untersuchen. Testmessungen wurden erfolgreich in einem Druckbereich bis zu 3.6 GPa durchgeführt.

Bibliography

[1] J. G. Bednorz and K. A. Müller, *Z. Phys. B: Condensed Matter*, **64** 189, (1986).

[2] A. Schilling, M. Cantoni, J. D. Guo, and H. R. Ott, *Nature*, **363**, 56, (1993).

[3] N. F. Mott, *Proc. Phys. Soc.*, London, Sect. A, **62** 416, (1949).

[4] N. F. Mott, *Can. J. Phys.*, **34** 1256, (1956).

[5] N. F. Mott, *Metal Insulator transition.* Taylor and Francis, London, (1974).

[6] P. W. Anderson, *Phys. Rev.*, **115**, 2, (1959).

[7] J. Hubbard, *Proc. R. Soc. London. Ser. A*, **277** 237, (1964).

[8] J. Hubbard, *Proc. R. Soc. London, Ser. A*, **281** 401, (1964).

[9] Masatoshi Imada, Atsushi Fujimori, and Yoshinori Tokura, *Rev. Mod. Phys.*, **70**, 1039, (1998).

[10] S. Nakamae, K. Behnia, N. Mangkorntong, M. Nohara, H. Takagi, S. J. C. Yates, and N. E. Hussey, *Phys. Rev. B*, **68**, 100502, (2003).

[11] M. Gurvitch and A. T. Fiory, *Phys. Rev. Lett.*, **59**, 1337, (1987).

[12] S. Martin, A. T. Fiory, R. M. Fleming, L. F. Schneemeyer, and J. V. Waszczak, *Phys. Rev. B*, **41**, 846, (1990).

[13] T. Timusk and B. Statt, *Reports on Progress in Physics*, **62**, 61, (1999).

[14] D. S. Marshall, D. S. Dessau, A. G. Loeser, C-H. Park, A. Y. Matsuura, J. N. Eckstein, I. Bozovic, P. Fournier, A. Kapitulnik, W. E. Spicer, and Z. X. Shen, *Phys. Rev. Lett.*, **76**, 4841, (1996).

[15] A. G. Loeser, Z. X. Shen, D. S. Dessau, D. S. Marshall, C. H. Park, P. Fournier, and A. Kapitulnik, *Science*, **273** 325, (1996).

[16] M. Buchanan, *Nature*, **409**, 8, (2001).

[17] J. M. Tranquada, B. J. Sternlieb, J. D. Axe, Y. Nakamura, and S. Uchida, *Nature*, **375**, 561, (1995).

[18] J. M. Tranquada, J. D. Axe, N. Ichikawa, A. R. Moodenbaugh, Y. Nakamura, and S. Uchida, *Phys. Rev. Lett.*, **78**, 338, (1997).

[19] P. Abbamonte, A. Rusydi, S. Smadici, G. D. Gu, G. A. Sawatzky, and D. L. Feng, *Nat. Phys.*, **1**, 155, (2005).

[20] H.-H. Klauss, W. Wagener, M. Hillberg, W. Kopmann, H. Walf, F. J. Litterst, M. Hücker, and B. Büchner, *Phys. Rev. Lett.*, **85**, 4590, (2000).

[21] M. Fujita, H. Goka, K. Yamada, J. M. Tranquada, and L. P. Regnault, *Phys. Rev. B*, **70**, 104517, (2004).

[22] S-W. Cheong, G. Aeppli, T. E. Mason, H. Mook, S. M. Hayden, P. C. Canfield, Z. Fisk, K. N. Clausen, and J. L. Martinez, *Phys. Rev. Lett.*, **67**, 1791, (1991).

[23] T. E. Mason, G. Aeppli, and H. A. Mook, *Phys. Rev. Lett.*, **68**, 1414, (1992).

[24] T. R. Thurston, P. M. Gehring, G. Shirane, R. J. Birgeneau, M. A. Kastner, Y. Endoh, M. Matsuda, K. Yamada, H. Kojima, and I. Tanaka, *Phys. Rev. B*, **46**, 9128, (1992).

[25] H. Kimura, K. Hirota, H. Matsushita, K. Yamada, Y. Endoh, S. H. Lee, C. F. Majkrzak, R. Erwin, G. Shirane, M. Greven, Y. S. Lee, M. A. Kastner, and R. J. Birgeneau, *Phys. Rev. B*, **59**, 6517, (1999).

[26] H. Matsushita, H. Kimuraa, M. Fujitab, K. Yamadab, K. Hirotaa, and Y. Endoha, *J. Phys. Chem. Solids*, **60** 1071, (1999).

[27] J. Orenstein and A. J. Millis. *Science*, **288**, 468, (2000).

[28] A. Lanzara, P. V. Bogdanov, X. J. Zhou, S. A. Kellar, D. L. Feng, E. D. Lu, T. Yoshida, H. Eisaki, A. Fujimori, K. Kishio, J. I. Shimoyama, T. Noda, S. Uchida, Z. Hussain, and Z. X. Shen, *Nature*, **412**, 510, (2001).

[29] T. P. Devereaux, T. Cuk, Z.-X. Shen, and N. Nagaosa, *Phys. Rev. Lett.*, **93**, 117004, (2004).

[30] D. N. Basov and T. Timusk, *Rev. Mod. Phys.*, **77**, 721, (2005).

[31] N. Ichikawa, S. Uchida, J. M. Tranquada, T. Niemöller, P. M. Gehring, S.-H. Lee, and J. R. Schneider, *Phys. Rev. Lett.*, **85**, 1738, (2000).

[32] V. J. Emery, S. A. Kivelson, and O. Zachar, *Phys. Rev. B*, **56**, 6120, (1997).

[33] A. Perali, C. Castellani, C. Di Castro, and M. Grilli. *Phys. Rev. B*, **54**, 16216, (1996).

[34] T. P. Devereaux and R. Hackl, *Rev. Mod. Phys.*, **79**, 175, (2007).

[35] F. Venturini, Q.-M. Zhang, R. Hackl, A. Lucarelli, S. Lupi, M. Ortolani, P. Calvani, N. Kikugawa, and T. Fujita, *Phys. Rev. B*, **66**, 060502, (2002).

[36] B. Simovic, M. Nicklas, P. C. Hammel, M. Hucker, B. Buchner, and J. D. Thompson, *Europhys. Lett.*, **66** 722, (2004).

[37] P. Fulde, *Electron Correlations in Molecules and Solids.* Springer, Berlin, (1995).

[38] A. Damascelli, Z. Hussain, and Z.X. Shen, *Rev. Mod. Phys.*, **75**, 473, (2003).

[39] H. Ding, M. R. Norman, T. Yokoya, T. Takeuchi, M. Randeria, J. C. Campuzano, T. Takahashi, T. Mochiku, and K. Kadowaki, *Phys. Rev. Lett.*, **78**, 2628, (1997).

[40] J. L. Tallon, C. Bernhard, H. Shaked, R. L. Hitterman, and J. D. Jorgensen. *Phys. Rev. B*, **51**, 12911, (1995).

[41] Cyril Proust, Etienne Boaknin, R. W. Hill, Louis Taillefer, and A. P. Mackenzie, *Phys. Rev. Lett.*, **89**, 147003, (2002).

[42] N. E. Hussey, M. Abdel-Jawad, A. Carrington, A. P. Mackenzie, and L. Balicas. *Nature*, **425**, 814, (2003).

[43] N. E. Hussey, K. Takenaka, and H. Takagi, *Phil. Mag.*, **24** 2847, 2004.

[44] S. Andergassen, S. Caprara, C. Di Castro, and M. Grilli, *Phys. Rev. Lett.*, **87**, 056401, (2001).

[45] S. Caprara, C. Di Castro, S. Fratini, and M. Grilli, *Phys. Rev. Lett.*, **88**, 147001, (2002).

[46] J. Bardeen, L. N. Cooper, and J. R. Schrieffer, *Phys. Rev.*, **106**, 162, (1957).

[47] C. E. Gough, M. S. Colclough, E. M. Forgan, R. G. Jordan, M. Keene, C. M. Muirhead, A. I. M. Rae, N. Thomas, J. S. Abell, and S. Sutton, *Nature*, **326**, 855, (1987).

[48] B. O. Wells, Z. X. Shen, D. S. Dessau, W. E. Spicer, D. B. Mitzi, L. Lombardo, A. Kapitulnik, and A. J. Arko, *Phys. Rev. B*, **46**, 11830, (1992).

[49] W. N. Hardy, D. A. Bonn, D. C. Morgan, Ruixing Liang, and Kuan Zhang. *Phys. Rev. Lett.*, **70**, 3999, (1993).

[50] D. J. Scalapino, *Phsy. Rep.*, **250** 329, (1995).

[51] N. Goldenfeld J.F. Annett and edited by D.M. Ginzberg A.J. Leggett. *in Physical Properties of High-Temperature Superconductors V*. World Scientific, Singapore, (1996).

[52] S. L. Cooper, F. Slakey, M. V. Klein, J. P. Rice, E. D. Bukowski, and D. M. Ginsberg, *Phys. Rev. B*, **38**, 11934, (1988).

[53] X. K. Chen, J. C. Irwin, H. J. Trodahl, T. Kimura, and K. Kishio, *Phys. Rev. Lett.*, **73**, 3290, (1994).

[54] T. P. Devereaux, D. Einzel, B. Stadlober, R. Hackl, D. H. Leach, and J. J. Neumeier, *Phys. Rev. Lett.*, **72**, 396, (1994).

[55] C. Kendziora and A. Rosenberg, *Phys. Rev. B*, **52**, R9867, (1995).

[56] G. Blumberg, Moonsoo Kang, M. V. Klein, K. Kadowaki, and C. Kendziora, *Science*, **278**, 1427, (1997).

[57] F. Venturini, M. Opel, R. Hackl, H. Berger, L. Forro, and B. Revaz, *J. Phys. Chem. Sol.*, **63**, 2345, (2002).

[58] S. Sugai, H. Suzuki, Y. Takayanagi, T. Hosokawa, and N. Hayamizu, *Phys. Rev. B*, **68**, 184504, (2003).

[59] K. McElroy, R. W. Simmonds, J. E. Hoffman, D.-H. Lee, J. Orenstein, H. Eisaki, S. Uchida, and J. C. Davis, *Nature*, **422**, 592, (2003).

[60] A. V. Chubukov, D. K. Morr, and G. Blumberg. *Sol. Stat. Comm.*, **112**, 183, (1999).

[61] A. V. Chubukov, T. P. Devereaux, and M. V. Klein, *Phys. Rev. B*, **73**, 094512, (2006).

[62] R. Zeyher and A. Greco, *Phys. Rev. Lett.*, **89**, 177004, (2002).

[63] H. J. Tao, Farun Lu, and E. L. Wolf, *Physica C: Superconductivity*, **282-287**, 1507, (1997).

[64] H. Ding, T. Yokoya, J. C. Campuzano, T. Takahashi, M. Randeria, M. R. Norman, T. Mochiku, K. Kadowaki, and J. Giapintzakis, *Nature*, **382**, 51, (1996).

[65] D. N. Basov, R. Liang, B. Dabrowski, D. A. Bonn, W. N. Hardy, and T. Timusk, *Phys. Rev. Lett.*, **77**, 4090–4093, (1996).

[66] A. V. Puchkov, P. Fournier, D. N. Basov, T. Timusk, A. Kapitulnik, and N. N. Kolesnikov, *Phys. Rev. Lett.*, **77**, 3212, (1996).

[67] T. Startseva, T. Timusk, A. V. Puchkov, D. N. Basov, H. A. Mook, M. Okuya, T. Kimura, and K. Kishio. *Phys. Rev. B*, **59**, 7184, (1999).

[68] Y. Ando, S. Komiya, K. Segawa, S. Ono, and Y. Kurita, *Phys. Rev. Lett.*, **93**, 267001, (2004).

[69] B. Bucher, P. Steiner, J. Karpinski, E. Kaldis, and P. Wachter, *Phys. Rev. Lett.*, **70**, 2012, (1993).

[70] H. Takagi, B. Batlogg, H. L. Kao, J. Kwo, R. J. Cava, J. J. Krajewski, and W. F. Peck, *Phys. Rev. Lett.*, **69**, 2975, (1992).

[71] R. Nemetschek, M. Opel, C. Hoffmann, P. F. Müller, R. Hackl, H. Berger, L. Forró, A. Erb, and E. Walker, *Phys. Rev. Lett.*, **78**, 4837, (1997).

[72] Naeini J. G., Irwin J. C., Sasagawa T., Togawa Y., and Kishio K, *cond-mat9909342*, (2000).

[73] M. Fujita, H. Goka, K. Yamada, and M. Matsuda, *Phys. Rev. Lett.*, **88**, 167008, (2002).

[74] S. Wakimoto, G. Shirane, Y. Endoh, K. Hirota, S. Ueki, K. Yamada, R. J. Birgeneau, M. A. Kastner, Y. S. Lee, P. M. Gehring, and S. H. Lee, *Phys. Rev. B*, **60**, R769, (1999).

[75] S. Wakimoto, R. J. Birgeneau, M. A. Kastner, Y. S. Lee, R. Erwin, P. M. Gehring, S. H. Lee, M. Fujita, K. Yamada, Y. Endoh, K. Hirota, and G. Shirane, *Phys. Rev. B*, **61**, 3699, (2000).

[76] S. A. Kivelson, I. P. Bindloss, E. Fradkin, V. Oganesyan, J. M. Tranquada, A. Kapitulnik, and C. Howald, *Rev. Mod. Phys.*, **75**, 1201, (2003).

[77] C. Castellani, C. Di Castro, and M. Grilli, *Z. phys. B*, **103** 137, (1997).

[78] C. Castellani, C. Di Castro, and M. Grilli, *Phys. Rev. Lett.*, **75**, 4650, (1995).

[79] J. Sólyom, *Adv. Phys.*, **28** 201, (1979).

[80] F. D. M. Haldane, *J. Phys. C*, **14** 2585, (1981).

[81] R. Shankar, *Rev. Mod. Phys.*, **66**, 129, (1994).

[82] C. Castellani, C. Di Castro, and W. Metzner, *Phys. Rev. Lett.*, **72**, 316, (1994).

[83] A. Houghton and J. B. Marston, *Phys. Rev. B*, **48**, 7790, (1993).

[84] A. H. Castro Neto and Eduardo Fradkin, *Phys. Rev. Lett.*, **72**, 1393, (1994).

[85] P. A. Bares and X.-G. Wen. *Phys. Rev. B*, **48**, 8636, (1993).

[86] A. Houghton, H.J. Kwon, J.B. Marston, and R. Shankar, *J. Phys. Condens. Matter (UK)*, **6** 4909, (1994).

[87] G. S. Boebinger, Yoichi Ando, A. Passner, T. Kimura, M. Okuya, J. Shimoyama, K. Kishio, K. Tamasaku, N. Ichikawa, and S. Uchida, *Phys. Rev. Lett.*, **77**, 5417, (1996).

[88] S. Lupi, P. Calvani, M. Capizzi, and P. Roy, *Phys. Rev. B*, **62**, 12418, (2000).

[89] C. Berthier, M. H. Julien, , M. Horvatic, and Y. Berthier, *Journal de physque I*, **6** 2205, (1996).

[90] B. Batlogg, H. Y. Hwang, H. Takagi, R. J. Cava, H. L. Kao, and J. Kwo, *Physica C: Superconductivity*, **235-240**, 130, (1994).

[91] J. Rossat-Mignod, L. P. Regnault, C. Vettier, P. Bourges, P. Burlet, J. Bossy, J. Y. Henry, and G. Lapertot, *Physica C: Superconductivity*, **185-189**, 86, (1991).

[92] J. M. Harris, Z. X. Shen, P. J. White, D. S. Marshall, M. C. Schabel, J. N. Eckstein, and I. Bozovic, *Phys. Rev. B*, **54**, R15665, (1996).

[93] J. W. Loram, K. A. Mirza, J. R. Cooper, and W. Y. Liang. *Phys. Rev. Lett.*, **71**, 1740, (1993).

[94] J. S. Zhou and J. B. Goodenough, *Phys. Rev. Lett.*, **77**, 151, (1996).

[95] H. Y. Hwang, B. Batlogg, H. Takagi, H. L. Kao, J. Kwo, R. J. Cava, J. J. Krajewski, and W. F. Peck, *Phys. Rev. Lett.*, **72**, 2636, (1994).

[96] T. Ito, K. Takenaka, and S. Uchida, *Phys. Rev. Lett.*, **70**, 3995, (1993).

[97] A. Abanov, A. V. Chubukov, and J. Schmalian, *Adv. Phys.*, **52**, 119, (2003).

[98] C. M. Varma. *Phys. Rev. Lett.*, **83**, 3538, (1999).

[99] C. M. Varma, *Phys. Rev. B*, **55**, 14554, (1997).

[100] W. Metzner, D. Rohe, and S. Andergassen, *Phys. Rev. Lett.*, **91**, 066402, (2003).

[101] Massimo Capone, Michele Fabrizio, Claudio Castellani, and Erio Tosatti, *Phys. Rev. Lett.*, **93**, 047001, (2004).

[102] J. L. Tallon and J. W. Loram, *Physica C: Superconductivity*, **349**, 53, (2001).

[103] A. J. Millis, Hartmut Monien, and David Pines, *Phys. Rev. B*, **42**, 167, (1990).

[104] S. Sachdev and J. Ye, *Phys. Rev. Lett.*, **69**, 2411, (1992).

[105] G. D. Mahan, *Many particle physics*, (1993).

[106] F. A. Blum, *Phys. Rev. B*, **1**, 1125, (1970).

[107] D. Pines and P. Nozières, *The theory of quantum liquids: Normal Fermi Liquids*. (1966).

[108] T. P. Devereaux and D. Einzel. *Phys. Rev. B*, **51**, 16336, (1995).

[109] M. V. Klein and S. B. Dierker, *Phys. Rev. B*, **29**, 4976, (1984).

[110] H. Monien and A. Zawadowski, *Phys. Rev. B*, **41**, 8798, (1990).

[111] B. Sriram Shastry and Boris I. Shraiman, *Int. J. Mod. Phys. B*, **5** 365, (1991).

[112] P. B. Littlewood and C. M. Varma, *Phys. Rev. Lett.*, **47**, 811–814, (1981).

[113] X. L. Lei, C. S. Ting, and Joseph L. Birman, *Phys. Rev. B*, **32**, 1464, (1985).

[114] I. Tüttő and A. Zawadowski, *Phys. Rev. B*, **45**, 4842, (1992).

[115] L. G. Aslamazov and A. I. Larkin, *Sov. Phys. Solid State*, **10** 875, (1968).

[116] S. Caprara, C. Di Castro, M. Grilli, and D. Suppa, *Phys. Rev. Lett.*, **95**, 117004, (2005).

[117] W. Brenig and H. Monien, *Sol. Stat. Comm.*, **83**, 1009, (1992).

[118] J. K. Freericks and T. P. Devereaux, *Phys. Rev. B*, **64**, 125110, (2001).

[119] T. P. Devereaux and A. P. Kampf, *Phys. Rev. B*, **59**, 6411, (1999).

[120] W. Götze and P. Wölfle, *Phys. Rev. B*, **6**, 1226, (1972).

[121] D. B. Tanner and T. Timusk, *Physical Properties of High Temperature Superconductors III*, page 363. World Scientific, Singapore, (1992).

[122] M. Opel, R. Nemetschek, C. Hoffmann, R. Philipp, P. F. Müller, R. Hackl, I. Tüttő, A. Erb, B. Revaz, E. Walker, H. Berger, and L. Forró, *Phys. Rev. B*, **61**, 9752, (2000).

[123] Andras Janossy, Titusz Feher, and Andreas Erb, *Phys. Rev. Lett.*, **91**, 177001, (2003).

[124] B. Keimer, N. Belk, R. J. Birgeneau, A. Cassanho, C. Y. Chen, M. Greven, M. A. Kastner, A. Aharony, Y. Endoh, R. W. Erwin, and G. Shirane, *Phys. Rev. B*, **46**, 14034, (1992).

[125] H. Takagi, T. Ido, S. Ishibashi, M. Uota, S. Uchida, and Y. TokuraD.B. *Phys. Rev. B*, **40**, 2254, (1989).

[126] J. D. Axe, A. H. Moudden, D. Hohlwein, D. E. Cox, K. M. Mohanty, A. R. Moodenbaugh, and Youwen Xu, *Phys. Rev. Lett.*, **62**, 2751, (1989).

[127] A. R. Moodenbaugh, Youwen Xu, M. Suenaga, T. J. Folkerts, and R. N. Shelton, *Phys. Rev. B*, **38**, 4596, (1988).

[128] Warren E. Pickett, *Rev. Mod. Phys.*, **61**, 433, (1989).

[129] Ch. Niedermayer, C. Bernhard, T. Blasius, A. Golnik, A. Moodenbaugh, and J. I. Budnick, *Phys. Rev. Lett.*, **80**, 3843, (1998).

[130] A. Erb, *The impact of crystal frowth, oxygenation and microstructure on the physics of the rare earth (123) superconductors.* PhD thesis, University of Geneva, (1999).

[131] J. M. Tranquada, A. H. Moudden, A. I. Goldman, P. Zolliker, D. E. Cox, G. Shirane, S. K. Sinha, D. Vaknin, D. C. Johnston, M. S. Alvarez, A. J. Jacobson, J. T. Lewandowski, and J. M. Newsam, *Phys. Rev. B*, **38**, 2477, (1988).

[132] A. Erb, E. Walker, and R. Flukiger, *Physica C: Superconductivity*, **258**, 9, (1996).

[133] T. B. Lindemer, J. F. Hunley, J. E. Gates, Jr. A. L. Sutton, J. Brynestad, C. R. Hubbard, and P. K. Gallagher, *J. Am. Ceram. Soc.*, **72** 1775, (1989).

[134] J. H. Claassen, M. E. Reeves, and Jr. R. J. Soulen. *Review of Scientific Instruments*, **62**, 996, (1991).

[135] F. Venturini, *Raman Scattering Study of Electronic Correlations in Cuprates: Observation of an Unconventional Metal-Insulator Transition.* PhD thesis, Technische Universität München, (2003).

[136] M. Opel, *Eigenschaften des Elektronensystems und seiner Wechselwirkungen in antiferromagnetischen und supraleitenden Kupraten: Eine Raman-Studie.* PhD thesis, Technische Universität München, (2000).

[137] W. Hayes and R. Loudon, *Scattering of Light by Crystals.* John Wiley & Sons, New York, (1978).

[138] C. Kendziora, Michael C. Martin, J. Hartge, L. Mihaly, and L. Forro, *Phys. Rev. B*, **48**, 35313, (1993).

[139] A. Zibold, L. Widder, H. P. Geserich, G. Brauchle, H. Claus, H. v. Lohneysen, N. Nucker, A. Erb, and G. Muller-Vogt, *Physica C: Superconductivity*, **212**, 365, (1993).

[140] F. Venturini, M. Opel, T. P. Devereaux, J. K. Freericks, I. Tüttő, B. Revaz, E. Walker, H. Berger, L. Forró, and R. Hackl, *Phys. Rev. Lett.*, **89**, 107003, (2002).

[141] R. Nemetschek, *Energielücke und Pseudogap in supraleitfähigem* $YBa_2Cu_3O_{6+x}$ *Ergebnisse der elektronischen Raman-Streuung.* PhD thesis, Technische Universität München, (1998).

[142] M. Fujita, K. Yamada, H. Hiraka, P. M. Gehring, S. H. Lee, S. Wakimoto, and G. Shirane, *Phys. Rev. B*, **65**, 064505, (2002).

[143] K. Yamada, C. H. Lee, K. Kurahashi, J. Wada, S. Wakimoto, S. Ueki, H. Kimura, Y. Endoh, S. Hosoya, G. Shirane, R. J. Birgeneau, M. Greven, M. A. Kastner, and Y. J. Kim, *Phys. Rev. B*, **57**, 6165, (1998).

[144] J. M. Tranquada, *to appear as a chapter in "Treatise of High Temperature Superconductivity" edited by J. Robert Schrieffer; e-print: cond-mat/0512115*, (2005).

[145] D. Reznik, L. Pintschovius, M. Ito, S. Iikubo, M. Sato, H. Goka, M. Fujita, K. Yamada, G. D. Gu, and J. M. Tranquada, *Nature*, **440**, 1170, (2006).

[146] L. Tassini, F. Venturini, Q.-M. Zhang, R. Hackl, N. Kikugawa, and T. Fujita. *Phys. Rev. Lett.*, **95**, 117002, (2005).

[147] B. R. Patton and L. J. Sham, *Phys. Rev. Lett.*, **31**, 631, (1973).

[148] S. Takada and E. Sakai, *Prog. Theor. Phys.*, **59** 1802, (1978).

[149] S. Sachdev, In Hao Bailin, editor, *Proceedings of the 19th IUPAP International Conference on Statistical Physics*, World Scientific, Singapore, pag. 289, Xiamen, China, (1996).

[150] S. J. L. Billinge, M. Gutmann, and E. S. Božin, *Int. J. Mod. Phys. B*, **17** 3640, (2003).

[151] S. Doniach and M. Inui, *Phys. Rev. B*, **41**, 6668, (1990).

[152] Y. J. Uemura, L. P. Le, G. M. Luke, B. J. Sternlieb, W. D. Wu, J. H. Brewer, T. M. Riseman, C. L. Seaman, M. B. Maple, M. Ishikawa, D. G. Hinks, J. D. Jorgensen, G. Saito, and H. Yamochi, *Phys. Rev. Lett.*, **66**, 2665, (1991).

[153] V. J. Emery and S. A. Kivelson, *Nature*, **374**, 434, (1995).

[154] V. J. Emery and S. A. Kivelson. *Phys. Rev. Lett.*, **74**, 3253, (1995).

[155] S. A. Kivelson, E. Fradkin, and V. J. Emery, *Nature*, **393**, 550, (1998).

[156] S. Chakravarty, R. B. Laughlin, D. K. Morr, and C. Nayak, *Phys. Rev. B*, **63**, 094503, (2001).

[157] A. Kampf and J. R. Schrieffer, *Phys. Rev. B*, **41**, 6399, (1990).

[158] A. P. Kampf and J. R. Schrieffer, *Phys. Rev. B*, **42**, 7967–7974, (1990).

[159] C. Kusko, R. S. Markiewicz, M. Lindroos, and A. Bansil, *Phys. Rev. B*, **66**, 140513, (2002).

[160] G. Kotliar and J. Liu, *Phys. Rev. Lett.*, **61**, 1784, (1988).

[161] X. G. Wen and P. A. Lee, *Phys. Rev. Lett.*, **76**, 503, (1996).

[162] J. G. Naeini, J. C. Irwin, T. Sasagawa, Y. Togawa, and K. Kishio, *Cond-mat9909342*, (2000).

[163] R. Hackl, L. Tassini, F. Venturini, C. Hartinger, A, Erb, N, Kikugawa, and T, Fujita, *Advances in Solid State Physics*. Springer, (2005).

[164] B. Muschler, Unpublished results.

[165] J. K. Freericks and T. P. Devereaux. *Phys. Rev. B*, **64**, 125110, (2001).

[166] S. Sugai and T. Hosokawa, *Phys. Rev. Lett.*, **85**, 1112, (2000).

[167] H. L. Liu, G. Blumberg, M. V. Klein, P. Guptasarma, and D. G. Hinks, *Phys. Rev. Lett.*, **82**, 3524, (1999).

[168] K. C. Hewitt and J. C. Irwin, *Phys. Rev. B*, **66**, 054516, (2002).

[169] T. Masui, M. Limonov, H. Uchiyama, S. Lee, S. Tajima, and A. Yamanaka. *Phys. Rev. B*, **68**, 060506, (2003).

[170] L. V. Gasparov, P. Lemmens, M. Brinkmann, N. N. Kolesnikov, and G. Güntherodt, *Phys. Rev. B*, **55**, 1223, (1997).

[171] L. V. Gasparov, P. Lemmens, N. N. Kolesnikov, and G. Güntherodt. *Phys. Rev. B*, **58**, 117530, (1998).

[172] A. Hoffmann, P. Lemmens, G. Guntherodt, V. Thomas, and K. Winzer, *Physica C: Superconductivity*, **235-240**, 1897, (1994).

[173] Y. Gallais, A. Sacuto, T. P. Devereaux, and D. Colson, *Physical Review B (Condensed Matter and Materials Physics)*, **71**, 012506, (2005).

[174] V. Hinkov, S. Pailhes, P. Bourges, Y. Sidis, A. Ivanov, A. Kulakov, C. T. Lin, D. P. Chen, C. Bernhard, and B. Keimer, *Nature*, **430**, 650, (2004).

[175] C. Stock, W. J. L. Buyers, R. A. Cowley, P. S. Clegg, R. Coldea, C. D. Frost, R. Liang, D. Peets, D. Bonn, W. N. Hardy, and R. J. Birgeneau, *Phys. Rev. B*, **71**, 024522, (2005).

[176] C. Stock, W. J. L. Buyers, Z. Yamani, C. L. Broholm, J.-H. Chung, Z. Tun, R. Liang, D. Bonn, W. N. Hardy, and R. J. Birgeneau, *Phys. Rev. B*, **73**, 100504, (2006).

[177] J. E. Hoffman, E. W. Hudson, K. M. Lang, V. Madhavan, H. Eisaki, S. Uchida, and J. C. Davis, *Science*, **295**, 466, (2002).

[178] V. V. Struzhkin, M. I. Eremets, Wei Gan, H. K. Mao, and J. Russell, Hemley. *Science*, **298**, 1213, (2002).

[179] M. C. Aronson, S. B. Dierker, B. S. Dennis, S-W. Cheong, and Z. Fisk, *Phys. Rev. B*, **44**, 4657, (1991).

[180] T. Zhou, K. Syassen, M. Cardona, J. Karpinski, and E. Kaldis, *Solid State Communications*, **99**, 669, (1996).

[181] A. F. Goncharov and V. V. Struzhkin, *J. Raman Spectrosc.*, **34** 532, (2003).

[182] C. E. Weir, E. R. Lippincott, A. Van Valkenburg, and E. N. Bunting. *J. Res. Natl. Bur. Stand.*, **63A** 55, (1959).

[183] J. A. Xu and H. K. Mao, *Science*, **290**, 783, (2000).

[184] G. J. Piermarini and S. Block. *Review of Scientific Instruments*, **46**, 973, (1975).

[185] H. K. MAO, *Science*, **200**, 1145, (1978).

[186] J. Yen and M. Nicol, *Journal of Applied Physics*, **72**, 5535, (1992).

[187] D. D. Ragan, R. Gustavsen, and D. Schiferl, *Journal of Applied Physics*, **72**, 5539–5544, 1992.

[188] F. Datchi, R. LeToullec, and P. Loubeyre, *Journal of Applied Physics*, **81**, 3333, (1997).

[189] F. Datchi, Unpublished results.

Acknowledgments

I am deeply grateful to Prof. Dr. R. Gross for giving me possibility to make my PhD. at the Walther Meissner Institut, for his constant willingness to discuss physics, and his continuous support.

I would like to express profound gratitude to Dr. Rudi Hackl, my academic advisor. This work would not have been possible without his continuous support and encouragement. I am deeply grateful to Rudi for teaching me all the experimental and physical know-how. I greatly profited from his vast experimental experience, continuous support, advise, and spontaneous help in any direction.

I am particularly thankful to Francesca Venturini. Without our meeting in Florence of few years ago, where I was introduced to the research done at WMI, this work would not have been possible. I really appreciated the many stimulating discussions we had.

I would like to express ma gratitude to Dr. A. Erb, M. Lambacher, Dr. N. Kikugawa, and Prof. T. Fujita for providing excellent samplels. I would like also to thank Dr. A. Erb and M. Lambacher for many useful discussions.

I am truly thankful to Prof. C. Di Castro, Prof. M. Grilli, Dr. D. Suppa, Dr. M. Ortolani, and Dr. L Benfatto for the many clarifying and stimulating discussions.

I would like to thank Prof. T. P. Deveraux for the many discussions I had the opportunity to have with him, for his continuous willingness to discuss and to enlighten me on the electronic Raman theory. I very much enjoyed the exciting discussions and the social events we had. I am also thankful for

the hospitality during my visit of the Waterloo University and for reading the manuscript.

I am very grateful to Dr. D. Einzel for theoretical support, for the many discussions we had, and for reading the manuscript.

I would like to thank B.S. Chandrasekhar for the many stimulating discussions we had about physics and various other subjects, and for reading the manuscript.

I am indebted to Dipl.-Ing. Thomas Brenninger for the helpful support on the high pressure cell design.

I am truly thankful to Dr. T. Roscilde for his spontaneous theoretical support, for many useful and stimulating discussions, and for the organization of various pleasant social evenings.

I am grateful to D. Galea for reading the manuscript.

A special thank is for W. Prestel to whom I shared the office. Discussions about physics as well about various other subjects were always enjoyable.

I would also like to express my gratitude to all the diploma and doctoral students, to the scientific and technical staff of the WMI for the spontaneous support and friendly atmosphere.

Desidero ringraziare la mia famiglia per il supporto l'affetto e la fiducia mostratomi in questi anni.

Infine un grazie speciale e' per Annalisa, per tutto l'affetto dimostratomi e per avermi sopportato durante la scrittura di questa Tesi.